

Testing of a Magnetically Levitated Rocket Thrust Measurement System Demonstrator for NASA

Eric J. Blumber

Thesis submitted to the Faculty of the
Virginia Polytechnic Institute and State University
in partial fulfillment of the requirements for the degree of

Master of Science
in
Mechanical Engineering

Dr. Mary Kasarda, Chairman

Dr. Gordon Kirk

Dr. Al Wicks

June 13, 2002
Blacksburg, VA

Keywords: Force Measurement, Active Magnetic Bearings, Thrust Measurement System
Copyright 2002, Eric Joseph Blumber

Testing of a Magnetically Levitated Rocket Thrust Measurement System
Demonstrator for NASA

Eric J. Blumber

(ABSTRACT)

Existing thrust measurement systems (TMSs) at NASA Stennis Space Center use strain gauges and flux plates to measure forces produced by a test article. Alignment and calibration can take two weeks or more every time a piece of hardware or test article is changed. Cross axis loading is also problematic because it is impossible to perfectly align the flex plates and strain gauges in the thrust direction. In response to these problems, a magnetically levitated thrust measurement system has been proposed and a 300lb capacity demonstrator has been designed and built. In this design, the magnetic bearings work concurrently as support bearings and force measurement devices. The demonstrator consists of a floating frame that is completely levitated within a fixed frame by four support bearings carrying loads in the x- and y-direction and seven thrust bearings carrying loads in the z- or thrust direction. Joe Imlach of Imlach Consulting Engineering designed the demonstrator and magnetic bearing components, while Virginia Tech's role has been the application of the multipoint calibration technique including code development, the implementation of a 128-channel data acquisition system, and the overall test verification of the TMS demonstrator.

A turnbuckle assembly and magnetostrictive actuator are used in series with a conventional load cell for static and dynamic testing, respectively. Both current based and flux based force equations were used to measure the reaction forces at the bearings. The static results using the current based equations including the current based fringing equations resulted in accuracies of 93% of full load, while the static results using the flux based equations including the flux based fringing equations resulted in accuracies of 99.5% of full load. These accuracies can be compared to accuracies of 83-90% seen in previous work using magnetic bearings to measure forces by monitoring currents and to accuracies of about 99% in previous work using magnetic bearings to measure forces by monitoring fluxes. All of the improved accuracies were made possible through the

implementation of a calibration technique known as the multipoint method and the implementation of a gap dependent fringing correction factor developed by Joe Imlach. The demonstrator was not outfitted with accelerometers so the inertia of the floating frame could not be accounted for, limiting the scope of dynamic testing. However, the tests confirmed the ability of the demonstrator to measure dynamic loads in general.

ACKNOWLEDGEMENTS

First, I would like to thank my advisor, Mary Kasarda, for choosing me to work with her on this project. I greatly value the freedom she gave me to work at my own pace and the trust that she had in me to get the work done. Just in case I did get stuck, she always made sure I had a way to contact her. I feel as though I am much more prepared for the working world because of my opportunity to work with her.

The next person I would like to recognize is Joe Imlach. Without his planning, hard work, and patience with me, this project would not have been possible. He did an outstanding job designing the test rig and working out the snags along the way. I would like to thank him for his insights and help in the near daily phone calls to Alaska that allowed me to finish on time.

I would also like to thank my committee members for their help along the way. I had the privilege of taking courses from both Dr. Wicks and Dr. Kirk. Dr. Kirk always used real world anecdotes to help emphasize points he wanted to make. Dr. Wicks made the class entertaining as well as humorous while still managing to teach the information. Both of them really helped to make my educational experience at Virginia Tech the best it could be.

I also need to thank all the guys from the lab. I always looked forward to our hang out times both during lunch and outside the office. Travis Bash was always willing to help out in any way possible. It always amazed me how busy he was yet could still carve out time for me. I could always count on Eric Stasiunas for off-the-wall humor and the latest movie critique. Rob Prins helped me both with the test rig and in preparing me for the real world. I greatly valued his advice to me about jobs, presentations, and working with others. He became not only an officemate, but also a good friend. I will miss the racquetball and tennis games we used to play.

I cannot leave out my parents, Joe and Diane Blumber, who have been so supportive of everything I have done. I am very lucky to have such loving and caring parents. I am most grateful to them for raising me in a Christian home and showing me what it means to be a follower of God.

I would like to acknowledge the National Aeronautics and Space Administration (NASA) for supporting the work presented in this paper under Contract No. NAS13-00029. I would also like to acknowledge NASA Stennis Space Center for their support on this project.

Last but certainly not least I would like to thank Chelsea McRaven. She is truly my other half because we help to balance one another's extremes. Her heart for others impresses me as well as her desire to serve God. I am so grateful for her love and support over the years, and I look forward to many more years together.

Eric J. Blumber

Blacksburg, VA

June, 2002

TABLE OF CONTENTS

| | |
|---|-----------|
| Abstract | ii |
| Acknowledgements | iv |
| List of Figures | ix |
| List of Tables..... | xii |
| Nomenclature | xiii |
| | |
| 1 Introduction and Literature Review | 1 |
| 1.1 General Overview | 1 |
| 1.2 Motivation for Magnetically Levitated Rocket TMS..... | 3 |
| 1.3 Literature Review..... | 5 |
| | |
| 2 Development of Force Equations..... | 14 |
| 2.1 Introduction | 14 |
| 2.2 Flux Based Force Equations..... | 14 |
| 2.3 Current Based Force Equations..... | 19 |
| | |
| 3 Experimental Description..... | 25 |
| 3.1 Overview of TMS Demonstrator..... | 25 |
| 3.2 Data Acquisition System..... | 30 |
| 3.2.1 Data Acquisition Hardware | 30 |
| 3.2.2 Data Acquisition Software | 32 |
| 3.3 Static Force Acquisition | 35 |
| 3.3.1 Setup Procedure..... | 36 |
| 3.3.2 Static Force Acquisition Procedure..... | 38 |
| 3.4 Dynamic Force Acquisition | 40 |
| 3.4.1 Setup Procedure..... | 41 |
| 3.4.2 Dynamic Force Acquisition Procedure | 43 |

| | |
|---|------------|
| 4 Calibration Procedure | 45 |
| 4.1 Introduction | 45 |
| 4.2 The Multipoint Method | 45 |
| 4.3 Using the Multipoint Algorithm as a Calibration Procedure | 49 |
| 4.4 Calibration Procedure for the TMS Demonstrator | 51 |
| 4.4.1 Setup Procedure..... | 52 |
| 4.4.2 Calibration Procedure..... | 53 |
| 5 Thermal Testing | 56 |
| 5.1 Introduction | 56 |
| 5.2 Procedure..... | 57 |
| 5.3 Thermal Testing Results and Conclusions | 58 |
| 6 Static Force Testing..... | 66 |
| 6.1 Introduction | 66 |
| 6.2 Vertical Weight Results and Conclusions | 66 |
| 6.3 Axial Loading Results and Conclusions | 68 |
| 7 Dynamic Force Testing | 79 |
| 7.1 Introduction | 79 |
| 7.2 Dynamic Results and Conclusions for Original System | 80 |
| 7.3 Dynamic Results and Conclusions for Stiffer System | 87 |
| 8 Summary of Results and Recommendations | 95 |
| 8.1 Overview of Work Completed | 95 |
| 8.2 Summary of Results | 96 |
| 8.3 Recommendations for Future Work..... | 98 |
| References | 100 |

| | |
|---|------------|
| Appendix A – Scale Drawings for TMS Demonstrator | 102 |
| A.1Front View..... | 103 |
| A.2Rear View..... | 104 |
| A.3Top View of Top Bearings..... | 105 |
| A.4Top View of Bottom Bearings | 106 |
| Appendix B – Uncertainty Analysis..... | 107 |
| B.1 Introduction | 107 |
| B.2Uncertainty Analysis for Current Based Force Equations | 109 |
| B.3Uncertainty Analysis for Flux Based Force Equations | 111 |
| Appendix C – FFT Analysis of Dynamic Data | 124 |
| C.1FFT Analysis for Data from Original System..... | 124 |
| C.2FFT Analysis for Data from Stiffer System..... | 126 |

LIST OF FIGURES

| <u>Number</u> | <u>Title</u> | <u>Page</u> |
|---------------|--|-------------|
| 1.1 | Required components for magnetic levitation | 2 |
| 1.2 | Schematic of double-acting AMB configuration | 2 |
| 2.1 | Schematic of horseshoe electromagnet and target | 15 |
| 2.2 | Schematic of a double-acting magnetic bearing | 17 |
| 2.3 | Diagram of leakage losses in a magnetic bearing | 18 |
| 2.4 | Diagram of fringing losses in a magnetic bearing | 18 |
| 2.5 | Schematic of ferromagnetic toroid with a concentrated winding | 20 |
| 3.1 | Schematic of TMS Demonstrator | 26 |
| 3.2 | Picture of TMS Demonstrator | 27 |
| 3.3 | Schematic of Support Bearing (schematic provided by Joe Imlach) | 28 |
| 3.4 | Schematic of Thrust Bearing (schematic provided by Joe Imlach) | 28 |
| 3.5 | Support Bearing and Thrust Bearing | 29 |
| 3.6 | Sample LabVIEW 6.1 Front Panel | 33 |
| 3.7 | Sample LabVIEW 6.1 Block Diagram | 33 |
| 3.8 | Flowchart of three main groups of programs | 34 |
| 3.9 | Turnbuckle Assembly for Static Testing | 36 |
| 3.10 | Front Panel of “FORCE MEASURE” VI | 39 |
| 3.11 | Magnetostrictive Actuator Assembly for Dynamic Testing | 41 |
| 4.1 | Schematic of double-acting single axis magnetic bearing | 46 |
| 4.2 | Typical B-H curve for magnetic material (Plonus, 1978) | 47 |
| 5.1 | Flux Versus Temperature for Both Actuators of Bearing 32_ | 59 |
| 5.2 | Current Versus Temperature Plots for Both Actuators of Bearing 32_ | 59 |
| 5.3 | Position Versus Temperature Plots for Both Actuators of Bearing 32_ | 60 |

LIST OF FIGURES

| <u>Number</u> | <u>Title</u> | <u>Page</u> |
|---------------|--|-------------|
| 5.4 | Flux Versus Temperature for Both Actuators of Bearing 37_ | 61 |
| 5.5 | Current Versus Temperature Plots for Both Actuators of Bearing 37_ | 62 |
| 5.6 | Position Versus Temperature Plots for Both Actuators of Bearing 37_ | 63 |
| 5.7 | Least Squares Curve Fits for Both Axes of Bearing 32_ | 64 |
| | | |
| 6.1 | Flux Based Static Results for Positive Pull with Turnbuckle and Six Thrust Bearings Energized | 69 |
| 6.2 | Current Based Static Results for Positive Pull with Turnbuckle and Six Thrust Bearings Energized | 70 |
| 6.3 | Flux Based Static Results for Positive Pull with Turnbuckle and Four Thrust Bearings Energized | 71 |
| 6.4 | Current Based Static Results for Positive Pull with Turnbuckle and Four Thrust Bearings Energized | 72 |
| 6.5 | Flux Based Static Results for Negative Pull with Turnbuckle and Six Thrust Bearings Energized | 73 |
| 6.6 | Current Based Static Results for Negative Pull with Turnbuckle and Six Thrust Bearings Energized | 74 |
| 6.7 | Flux Based Static Results for Negative Pull with Turnbuckle and Four Thrust Bearings Energized | 75 |
| 6.8 | Current Based Static Results for Negative Pull with Turnbuckle and Four Thrust Bearings Energized | 76 |
| 6.9 | Typical Plot of Calculated Axial Load Versus Load Cell Measurement | 77 |
| | | |
| 7.1 | Dynamic Results for Input Frequency of 5Hz for Original System | 80 |
| 7.2 | Dynamic Results for Input Frequency of 10Hz for Original System | 81 |
| 7.3 | Dynamic Results for Input Frequency of 20Hz for Original System | 82 |
| 7.4 | Dynamic Results for Input Frequency of 30Hz for Original System | 83 |
| 7.5 | Dynamic Results for Input Frequency of 50Hz for Original System | 84 |
| 7.6 | Time Response with Swept Sine Input for Original System | 85 |

LIST OF FIGURES

| <u>Number</u> | <u>Title</u> | <u>Page</u> |
|---------------|---|-------------|
| 7.7 | Time Response for Load Cell with Swept Sine Input for Original System | 86 |
| 7.8 | Dynamic Results for Input Frequency of 5Hz for Stiffer System | 88 |
| 7.9 | Dynamic Results for Input Frequency of 10Hz for Stiffer System | 89 |
| 7.10 | Dynamic Results for Input Frequency of 20Hz for Stiffer System | 90 |
| 7.11 | Dynamic Results for Input Frequency of 30Hz for Stiffer System | 91 |
| 7.12 | Dynamic Results for Input Frequency of 50Hz for Stiffer System | 92 |
| 7.13 | Time Response with Swept Sine Input for Stiffer System | 93 |
| 7.14 | Time Response for Load Cell with Swept Sine Input for Stiffer System | 94 |

LIST OF TABLES

| <u>Number</u> | <u>Title</u> | <u>Page</u> |
|---------------|--|-------------|
| 3.1 | Summary of National Instruments Components | 30 |
| 4.1 | Summary of PVF Controller Files Used in the “AUTOCAL” VI | 54 |
| 5.1 | Percent Error Full Load Results from Individual Thrust Bearings | 63 |
| 5.2 | Summary of Quadratic Least Squares Fit on Flux and Temperature Data | 64 |
| 6.1 | Estimation of the Weight of the Floating Frame | 67 |
| 6.2 | Comparison of Axially Unloaded Summed Flux and Current Based Y-Direction Forces with Estimated Floating Frame Weight | 68 |
| 7.1 | Summary of Proportional Gains Used for Original and Stiffer Systems | 88 |

NOMENCLATURE

| <u>Symbol</u> | <u>Metric Units</u> | <u>Description</u> |
|---------------------------|---------------------|---|
| A | m^2 | Cross Sectional Area |
| A_t | m^2 | Cross Sectional Area of Toroid |
| A_i | - | Current Based MFEA Constant |
| A_b | - | Flux Based MFEA Constant |
| A_g | m^2 | Air Gap Area |
| B | T | Magnetic Flux Density |
| B_1 | T | Top Magnetic Flux Density |
| B_{\max} | T | Maximum Flux Density |
| B_{\min} | T | Minimum Flux Density |
| B_2 | T | Bottom Magnetic Flux Density |
| F | N | Force |
| F_1 | N | Force Due to Top Actuator |
| F_2 | N | Force Due to Bottom Actuator |
| F_b | N | Flux Based Force |
| F_{est} | N | Estimated Weight of the Floating Frame |
| $F_{\text{flux/current}}$ | N | Sum of the Y-direction forces for Flux or Current Based Methods |
| F_i | N | Current Based Force |
| F_{LC} | N | Force Measured from Load Cell |
| F_{net} | N | Net Force |
| F_{result} | N | Resultant Force |
| F_{DCx} | N | Unloaded Force in the X-direction |
| F_{DCy} | N | Unloaded Force in the Y-direction |
| F_{DCz} | N | Unloaded Force in the Z-direction |
| F_x | N | Force in the X-direction |
| F_y | N | Force in the Y-direction |
| F_z | N | Force in the Z-direction |
| ff_1 | - | Top Fringing Factor |

NOMENCLATURE

| <u>Symbol</u> | <u>Metric Units</u> | <u>Description</u> |
|------------------|---------------------|---|
| ff_2 | - | Bottom Fringing Factor |
| g | m | Air Gap Length |
| g_1 | m | Top Air Gap |
| g_2 | m | Bottom Air Gap |
| g_0 | m | Nominal Air Gap |
| g_{01} | m | Nominal Air Gap of Outer Legs |
| g_{02} | m | Nominal Air Gap of Center Leg |
| H | A/m | Magnetic Field Strength |
| I | A | Current |
| I_1 | A | Top Current |
| I_2 | A | Bottom Current |
| K_b | - | Flux Based MFEA Constant |
| K_i | - | Current Based MFEA Constant |
| L_i | m | Mean Iron Path Length |
| l | m | Length |
| m | - | Counting Variable |
| N | - | Number of Coils, also Number of Energized Thrust Bearings |
| \mathfrak{R} | A/Wb | Magnetic Reluctance |
| \mathfrak{R}_g | A/Wb | Magnetic Reluctance Through Air Gap |
| \mathfrak{R}_i | A/Wb | Magnetic Reluctance Through Iron |
| V | m^3 | Volume |
| V_{DCLC} | V | Unloaded Voltage Measured from Load Cell |
| V_{LC} | V | Voltage Measured from Load Cell |
| W | - | Flux Based MFEA Constant |
| W_{mag} | J | Magnetic Energy |
| W_{mech} | J | Mechanical Energy |
| W_1 | - | Current Based MFEA Constant |

NOMENCLATURE

| <u>Symbol</u> | <u>Metric Units</u> | <u>Description</u> |
|---------------|---------------------|---|
| W_2 | - | Current Based MFEA Constant |
| W_3 | - | Current Based MFEA Constant |
| W_4 | - | Current Based MFEA Constant |
| x | m | Target Position |
| x_{ptp} | m | Absolute Target Position Predicted by Calibration |
| α_b | - | Flux Based MFEA Constant |
| α_i | - | Current Based MFEA Constant |
| ϕ | Wb | Magnetic Flux |
| ϕ_g | Wb | Magnetic Flux Through Air Gap |
| ϕ_i | Wb | Magnetic Flux Through Iron |
| Σ | - | Standard Deviation Matrix |
| σ | - | Standard Deviation |
| μ_0 | Wb/A-m (N/A^2) | Magnetic Permeability of Free Space |
| μ_i | Wb/A-m (N/A^2) | Magnetic Permeability of Iron |
| μ_r | - | Relative Magnetic Permeability |

Chapter 1

Introduction and Literature Review

1.1 General Overview

Active magnetic bearings (AMBs) are electromechanical devices that use a feedback control system to keep a rotor, or target, levitated at a fixed position in a magnetic field. Because there is no contact between the electromagnetic actuator and the target and because of the feedback nature of AMBs, many new uses and applications that are impossible with conventional bearings are being developed. This thesis discusses the use of magnetic bearings in a magnetically levitated rocket Thrust Measurement System (TMS) for NASA. The magnetic bearings are used as both support bearings to levitate the test article as well as sensors to measure the forces produced by the test article. The goal of this project is to demonstrate the use of magnetic bearings in a TMS prototype by calculating accurate forces generated by a simulated test article in the TMS. A calibration process known as the multipoint method as well as equations to account for fringing losses are introduced to measure applied forces within 0.5% error full load.

There are four main components required by AMBs as shown in Figure 1.1. The four main components are the actuator, the rotor, the position sensor, and the controller and power amplifier. If the AMB is not used in a rotating application, as is the case for the rocket TMS, the rotor is called a target instead because there are no rotating parts. The AMB works by measuring the position of the target using the position sensor and comparing it to a predetermined desired location set by the controller. The controller then adjusts the current through the coil of the actuator to keep the target levitated. The

coil currents are adjusted thousands of times per second by the controller to keep the target accurately located in the desired position.

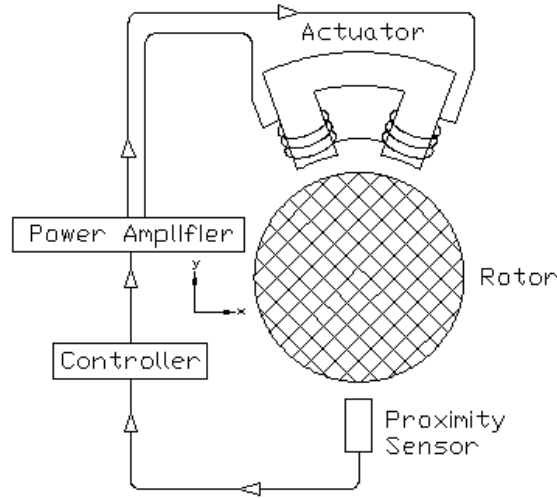


Figure 1.1: Required components for magnetic levitation

The most common arrangement for AMBs is the double-acting configuration in which there are two electromagnetic actuators arranged in opposing directions with a target located between them. A schematic is shown in Figure 1.2. For this configuration,

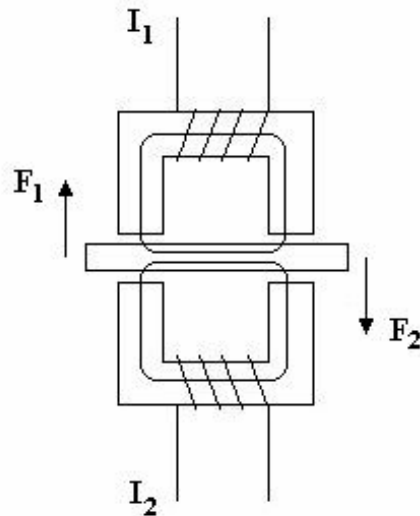


Figure 1.2: Schematic of double-acting AMB configuration

the position of the target is measured by the position sensor. The controller then adjusts both the top and bottom coil currents to maintain a predetermined fixed target position accurately. For instance, if the position sensor measures that the target is too close to the top actuator, the controller will increase the current in the bottom coil and decrease the current in the top coil to move the target downward.

The force produced by each magnetic actuator on the target is proportional to the magnetic flux through the air gap between that actuator and the target. Because flux sensors are needed to measure the flux in the air gap, it is often desirable to calculate forces using coil currents and air gaps instead. The general equation relating magnetic flux density, B , to coil current, I , and air gap, g , is shown in Equation 1.1.

$$B = \frac{\mu_o NI}{g} \quad (1.1)$$

In this equation, μ_o is the permeability of free space and N is the number of turns in the coil. Due to the feedback system of the AMB, the coil currents and relative target positions are easily accessible from the controller. The coil currents and air gaps can then be used to infer the magnetic flux through the air gaps. Therefore, given either the magnetic flux through the air gaps or the coil currents and physical target position, the forces exerted by the actuator on the target can be calculated. The equations used for force calculations will be discussed in more detail in Chapter 2.

1.2 Motivation for Magnetically Levitated Rocket TMS

Current rocket TMSs utilize strain gauges to measure thrust and off-axis loads. Existing test stands consist of a floating frame on which the test article is rigidly mounted to a fixed frame via flex plates and data columns. The data columns and flex plates which connect the floating frame to the fixed frame must be aligned and calibrated to accurately measure the forces exerted by the test article, or rocket engine.

There are several weaknesses to this design that can be solved using a TMS with active magnetic bearings. The first is the amount of time needed for calibration and alignment of the flex plates and data columns. The calibration process alone currently takes upwards of two weeks to perform and must be repeated every time a new test article or piece of hardware is implemented. Even after the test stand is calibrated, cross-axis forces can be supported by the flex plates and data columns because it is impossible to achieve a perfect alignment. With a TMS fitted with magnetic bearings, the flex plates and data columns are replaced by magnetic bearings. In this case, the floating frame is completely levitated in a magnetic field so there is no contact between the floating and fixed frames. For a TMS using magnetic bearings, a calibration process known as the multipoint method can be performed on the test stand. The multipoint method calibration technique determines the physical air gaps for all of the magnetic bearings for use in the force equations. This calibration only takes a couple of hours compared to a couple of weeks for conventional TMS setups. The calibration process for the TMS demonstrator is discussed in more detail in Chapter 4. Also, because the floating frame is completely isolated from the fixed frame and the targets have been oversized to minimize cross-axis forces, alignment is no longer problematic. After the calibration process is complete, the static loads can be calculated and subtracted out of subsequent force measurements if desired.

Another issue with current thrust stands is the limited thrust ranges that can be measured by a single stand. Current thrust stands cannot handle a large range of thrust loads while keeping the accuracy needed for a TMS. Therefore, multiple thrust stands are needed to accurately measure forces for rockets with various thrust outputs. The magnetically levitated rocket TMS, however, can measure forces over a range of more than ten times the minimum load without a loss in accuracy. This is due to the fact that the magnetic bearings that support forces in the thrust direction, also known as thrust bearings, are mounted in parallel so different numbers of thrust bearings can be turned on or off to cover a wider range of thrust loads.

One final advantage of a magnetically levitated rocket TMS over conventional TMSs utilizing strain gauges is the ability to modify the frequency response of the TMS using the gain parameters of the magnetic bearings. Because conventional TMSs utilize flex plates and data columns, the dynamics of the system are fixed once the test stand has been assembled. However, with the magnetic bearing design, the dynamics of the TMS can be changed once the test stand is built simply by varying the gain parameters of the magnetic bearings. This is helpful because the dynamics of the TMS system are also a factor of the test article. A heavier test article may reduce the resonant frequency of the TMS enough that it falls within the frequency range of force measurements. In the case of conventional TMSs, the test stand would need to be redesigned; however, in the case of the magnetically levitated TMS, the gain parameters of the magnetic bearings can be changed to move the resonant frequency of the TMS out of the frequency range of interest.

Current TMSs must measure forces with less than a 1% error. To prove the capability of the magnetically levitated rocket TMS, it is desirable to demonstrate accurate force measurements within 0.5% error. This is accomplished using the multipoint calibration procedure as well as the improved flux based force equations that account for fringing losses as a function of air gap.

1.3 Literature Review

The concept of magnetic bearings has been around for decades (Imlach et al., 1990), but has not been economically or technically viable until the advent of high-speed electronics (Kasarda, 2000). Today magnetic bearings are a proven technology in many commercial applications including active vibration control and rotating applications where severe environments or low maintenance are critical. Recently the use of active magnetic bearings concurrently as support bearings and non-invasive force measurement devices has been investigated for various applications, and with varying degrees of success.

AMBs have been used in laboratory settings to measure forces in propulsion devices, seals, and bearings. In these applications, the pump rotor is completely supported by magnetic bearings. Thus, by directly measuring the bearing reaction forces, it is possible to determine the radial and axial hydraulic loads acting on the pump impeller as well as obtain information about the flow characteristics that are otherwise difficult to obtain (Guinzburg and Buse, 1994; Guinzburg and Buse, 1995; Baun and Flack, 1999). Previous methods used either strain measurements or pressure taps in the compressor shroud to measure forces. Baun and Flack (1999) used a current based force equation to calculate forces using the magnetic bearings in their test stand. Their test stand uses magnetic bearings to measure radial and axial hydraulic forces in a centrifugal pump. The force equation used for this work is shown in Equation 1.2.

$$F_{th} = k_{th} \left[\frac{i_1^2}{(2g_1 + b_{th})^2} - \frac{i_2^2}{(2g_2 + b_{th})^2} \right] \quad (1.2)$$

where

$$k_{th} = \mu_o A_g N^2 \quad (1.3)$$

and

$$b_{th} = \frac{L_i}{\mu_r} \quad (1.4)$$

For this equation, F_{th} is the theoretical force applied by the magnetic bearing in a double-acting configuration and k_{th} and b_{th} can be calculated based on actuator geometry and material magnetic properties. The parameters in the k_{th} equation are the permeability of free space, μ_o , the air gap area, A_g , and the number of turns in the coil, N . The b_{th} equation parameters are the mean path length of the iron, L_i , and the relative permeability of the iron, μ_r . The actual force relationship for the thrust actuator used on the pump test rig as well as any nonlinear effects due to material hysteresis, eddy currents, leakage, and fringing were determined by a calibration apparatus and systematic calibration developed by Baun. This calibration apparatus and procedure is discussed in more detail in (Baun et al., 1996). A static calibration procedure was also conducted to find the optimized values

of k_{exp} and b_{exp} that minimized the root-mean-square error between the load cell measurements and the forces calculated by the magnetic bearings.

Fittro et al. (1997) used a similar model to calibrate an 8-pole planar radial magnetic actuator. Three theoretical models of varying degrees of complexity were used to predict forces. The first model, deemed the full model, was developed using magnetic circuit theory and assuming constant magnetic material properties. The flux is found by relating it to the coil currents and air gaps. Two sets of linearly independent equations are generated using nodal equations as well as a complete set of independent loop equations. These equations are compiled in matrix form to determine the forces in the X- and Y-directions. The form of these matrix equations is shown in Equations 1.5 and 1.6.

$$F_x = \varepsilon k_{th} I^T N^T R^{-T} A_x R^{-1} NI \quad (1.5)$$

$$F_y = \varepsilon k_{th} I^T N^T R^{-T} A_y R^{-1} NI \quad (1.6)$$

where

$$k_{th} = \frac{\mu_o A N^2}{2} \quad (1.7)$$

In these equations, A_x and A_y are matrices that account for the sines and cosines of the pole angles. The second model, deemed the reduced model, makes two additional assumptions that reduce the number of flux densities to be solved for from 24 down to 8. These assumptions are that the stator back iron and rotor have infinite permeability while referring their actual reluctances back to the stator legs and that the journal fluxes are treated as if they originate from a single pole at the center of the rotor. The third model, deemed the uncoupled model, makes the assumption that the actuator is fully uncoupled. This reduces the number of fluxes to be solved for to 4.

The system is then calibrated by recording the coil currents and rotor positions as the magnetic actuator is moved relative to the stator and the coil currents are varied. An optimization routine based on Powell's method is then employed to minimize the RMS

error between the experimental actuator force, as measured by a load cell, and the force calculated using Equations 1.2 through 1.4. This results in an experimentally determined k_{exp} and b_{exp} as described previously. The full model resulted in RMS errors of approximately 0.19% while the reduced model resulted in RMS errors of about 0.17%. The error of the uncoupled model was much higher resulting in the conclusion that the assumption that the actuator is fully uncoupled is inaccurate. Due to the accuracy and simplicity of the reduced model, it was chosen as the preferred model and used to generate the remainder of the data.

The optimized values of k_{exp} and b_{exp} are then used to calculate the forces in the actuators. These results are then compared to the measurements from the load cell. The resulting errors were normally distributed with a mean of 1.04% with a standard deviation of 3.69% and a maximum error of about 10%. These are good results from a current based force calculation, however, the calibration routine involved applying known loads, which is not practical in a field situation.

Hysteresis testing was also performed on the test rig to determine the affect of increasing and decreasing currents on the calculated forces. The tests resulted in an average variation between increasing and decreasing currents of about 2.0%. Because the combined errors from the calibration and the static force measurements are significantly higher than the hysteresis errors, the hysteresis errors can be considered insignificant.

Magnetic bearings have also been used to determine the dynamic labyrinth coefficients for turbo compressors (Wagner and Steff, 1998). The operational reliability of turbo compressors with very high power densities depends on an accurate determination of fluid forces originating from the interstage seals and from the balance piston. Analytical calculations such as the computational fluid dynamics (CFD) method and bulk-flow method have been used to aid in the rotor-dynamic design of such turbomachines. The results of these calculations are highly dependent on the selected boundary conditions and parameters. Thus at low speeds and pressures the calculated values show an acceptable coincidence; however, at high speeds and high pressures, they

may deviate sharply from the measured values. As a result, experimental verification of the labyrinth stiffness and damping coefficients remains indispensable. In the test rig used by Wagner and Steff, magnetic bearings are used to levitate the rotor as well as directly measure the forces acting on the rotor.

Wagner and Steff use a current based force equation that is linearized about the equilibrium state to measure the forces in the magnetic bearing. The general force equation used is shown in Equation 1.8.

$$F = F_o + k_s \tilde{x} + k_q \tilde{i} \quad (1.8)$$

The coefficients F_o , k_s , and k_q are functions of the equilibrium state ($x_{\text{brg}}=x_o$ and $i=i_o$), the magnetic biasing current, and bearing geometry. Because the gas forces have a static component due to unavoidable rotor eccentricities, k_s and k_q are also a function of operating point. To reduce these effects, a correction coefficient for each bearing is calculated based on the condition of static equilibrium and no gas forces. The errors in force calculation for these tests are not discussed; however, the results proved successful in making available reliable data for calculating the stability behavior of industrial compressors.

Aenis and Nordmann (1999, 2000) investigate the use of magnetic bearings for fault detection in turbomachines. Today's monitoring systems are not an integral component in turbomachines, but must be purchased separately by the operators. For these failure detection systems, the motions of the rotor are measured as output signals and compared to a faultless initial state. The diagnosis attempts to detect deviations from the initial state and propose a cause. The problem with these systems is that the causes of the changes in the output signal cannot be detected clearly because the deviation from the initial state could be due to a change in the process or a modification of the system itself. Active magnetic bearings can be introduced to the system to improve the diagnostic technique.

The magnetic bearings can be used to excite the rotating shaft without contact and measure simultaneously the required forces and displacements precisely. Frequency response function can then be generated between the measured input and output signals. These frequency response functions can be compared to an initial state to determine certain faults in turbomachines. In order to generate accurate frequency response functions, it is necessary to accurately measure the forces at the magnetic bearings. Aenis and Nordmann compare three techniques for force measurement for use in this application. The first equation used to calculate magnetic bearing forces while the bearings are in differential mode is shown in Equation 1.9.

$$F_x = k_i i_x + k_s s_x \quad (1.9)$$

In this equation, F_x is the force in the x-direction, i_x is the control current in the x-direction, s_x is the rotor displacement in the x-direction, and k_i and k_s are linearization constants that depend on the chosen design point of the magnetic bearing. This method, called the i-s method, resulted in errors of about 17% in an operating range of $\pm 700\text{N}$. A calibration was used that performs a least-squares curve fit on the k_i - k_s -plane to the measured data. Including the calibration, errors were reduced to less than 9%.

The second force measurement method used was based on a reluctance network. For this method, the entire bearing is modeled as a multi-node network of variable reluctances. The magnetic network can be computed in a similar way to electrical networks. Given coil current data and position data, the model calculates the magnetic flux and from this, the force generated by the bearing. Because of the mathematical complexity of this method, it could not be used to calculate real time applied forces. For this method, errors are about 11% because the non-linearities of the magnetic material are not modeled. More recent work by Aenis and Nordmann has proven errors of about 8% using this same method, however details were not given as to the calibration procedures used to improve the results.

The third and final force measurement method used by Aenis and Nordmann involves the use of Hall effect flux sensors in the air gap between the actuator and rotor. Reported errors for this method are about 5% for the entire working range with most of the error resulting from an offset depending on the rotor position. If a rotor position dependent factor is introduced to account for the offset, errors are reduced to 2.8%. If the rotor is only operated in the nominal center of the bearing, expected errors are less than 1% for this method.

Flux sensors are also used to calculate bearing forces in the test rig designed by Knopf and Nordmann (1998) for the identification of the dynamic behavior of turbulent journal bearings. The magnetic bearings are used to levitate the rotor and to generate a relative motion between the rotating and the stationary part of the journal bearing. The magnetic bearings are used both as actuators and force measurement devices. The force measurements were used in this case to align the rotor in the journal bearing and determine bearing clearances. To calculate accurate forces for this application, known loads were applied to the rotor and forces were calculated using the flux density measurements from the Hall effect probes. Calibration factors were then chosen to minimize the error at maximum magnetic forces. This method results in errors of less than 1% over the entire operating range of the bearings. Higher errors result if eccentric rotor positions are considered due to the change in flux distribution on the pole surface with the rotor position that cannot be measured by the Hall sensors.

In order to increase the accuracy of force measurement for both current based and flux based equations, work has been done to characterize effects such as fringing. Imlach et al. (2000) found that fringing was a strong function of both air gap and magnetic bearing geometry. The work presents a fringing model for a planar E-core actuator geometry that relates a fringing correction factor to the ratio of air gaps and actuator pole widths. As the target is moved relative to the actuator, the amount of fringing changes, resulting in varying correction factors. Smaller air gaps between the target and actuator result in larger amounts of fringing. Fringing effects are discussed in more detail in Section 2.2. The function used to describe the position dependency of the fringing factor

is a compound exponential, with three parameters used to tune the model (Kasarda et al., 2000). Equation 1.10 shows the general form of the fringing equation that fits the data for air gap to pole width ratios of between 0.01 and 0.10. This range covers the design envelope for most practical systems.

$$Y(G/W) = \alpha + \beta \left(1 + e^{-\gamma \frac{G}{W}} \right) \quad (1.10)$$

In Equation 1.10, G is the air gap length, W is the width of the actuator pole, and α , β , and γ are the three parameters used to tune the model.

The accuracy of current based force calculations for magnetic bearings was improved by a technique called the multipoint method (Marshall, 2000). In this technique, several perturbations are made to the magnetic bearing system using bias currents. These perturbations are then processed mathematically to determine both the force and effective gap at each bearing. The multipoint method is discussed in more detail in Section 4.2. Marshall uses a constant derating factor, as does Baun et al. (1996), to account for magnetic losses. Errors in force calculations using the multipoint method were less than 3% whereas errors using single point techniques with no system perturbations led to errors of more than 6%. The multipoint method provides more accurate force calculations; however, at this time known forces must still be applied to the bearings to calculate the constant derating factor. Using Magnetic Finite Element Analysis (MFEA) to calculate the derating factor caused by effects such as fringing would add to the versatility of the multipoint method by allowing accurate forces to be calculated without applying known loads.

The multipoint method has also been verified using MFEA (Kasarda et al., 2000). The validation was performed by two groups of researchers. One group performed the MFEA analysis using various loads and air gaps. The coil currents generated in the MFEA analysis were then given to the second group of researchers who used them with an AMB model that included the fringing model to predict the forces and displacements

used originally. The results showed errors of less than 0.1% for both the predicted forces and displacements. This work did not include experimental results to further validate the technique.

Imlach et al. (2000) present a calibration technique for current based force equations utilizing the multipoint method. Unlike the work done by Marshall (2000), the multipoint method is presented as an in-situ calibration method rather than a static force measurement technique. Perturbations are performed to infer additional information about the system. The result of the calibration is the absolute actuator/target gap for each magnetic bearing on which the multipoint method is performed. This calibration technique solves the difficult problem of measuring physical air gaps, a necessary parameter for accurate force measurement. The multipoint method calibration is discussed in more detail in Section 4.3.

The use of magnetic bearings for industrial applications such as manufacturing scenarios has also been examined. Kasarda (1999) addresses the benefit of using magnetic bearings for improved process control. In these applications, magnetic bearings can be used to monitor industrial processes such as fiber extrusion in which the quality of the product is directly related to the ability to hold a constant tension between rollers. In a similar application, magnetic bearings can be used to observe operating forces within machinery allowing improved diagnostic information for health monitoring purposes. This would allow maintenance to be performed when needed, instead of according to a schedule, resulting in longer and safer production runs.

Chapter 2

Development of Force Equations

2.1 Introduction

In this chapter, both flux based and current based force equations are developed for the magnetic bearings. The flux based equations lead to more accurate force calculations (Aenis and Nordmann, 2000); however, the need for additional hardware and larger air gaps for the flux sensors make current based force equation more attractive in some applications. The currents and relative target positions needed for the current based force equations are readily available from the magnetic bearing controller because of the feedback nature of the bearings.

A fringing factor is also applied to both the flux and current based force equations to account for fringing effects. Joe Imlach, who participated in the research for this project, developed the fringing factor equations using Magnetic Finite Element Analysis (MFEA). Fringing was found to be a strong function of air gap length as well as bearing geometry. Fringing factor equations were developed for both the flux and current based force equations, and MFEA was used to verify the validity of these equations for the E-core actuators used in the TMS demonstrator. More details on the methods used to determine these equations can be found in [10].

2.2 Flux Based Force Equations

The flux based force equation for magnetic bearings is derived from simple magnetic circuit theory. A magnetic bearing can be modeled as a basic horseshoe electromagnet and target. Figure 2.1 shows a schematic of this basic setup. In this

schematic, N is the number of coils around the horseshoe, I is the current in the coils, A_g is the area of the air gap, and g is the air gap between the horseshoe and the target.

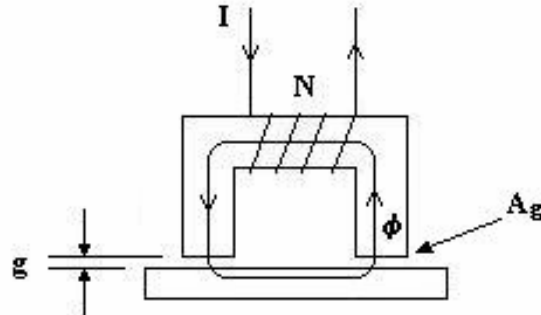


FIGURE 2.1: Schematic of horseshoe electromagnet and target

The current in the coils around the horseshoe induces a magnetic flux, ϕ , in the direction shown. All of the flux is assumed to be confined to the ferromagnetic core and the air gap volume defined by the projection of the pole face on the target. Neglecting edge effects such as fringing and leakage in this discussion allows scalar rather than vector equations to be used in the derivations. This results in unidirectional forces perpendicular to the pole face and target. Edge effects will be discussed in more detail in later discussion.

If we assume that the current is allowed to change so as to keep the magnetic flux constant, then a change in magnetic energy can only occur as a change in the energy stored in the air gap. The energy stored in each air gap is given by:

$$W_{mag} = \frac{1}{2} \mu_o H^2 V \quad (2.1)$$

where μ_o is the permeability of free space, H is the magnetic field strength, and V is the volume of the air gap. The volume of the air gap is simply the area of the gap times the length of the gap, or $A_g * g$. If the target is displaced an additional Δg , then the change in energy for both air gaps is:

$$\Delta W_{mag} = 2 \left[\frac{1}{2} \mu_o H^2 A_g (g + \Delta g) - \frac{1}{2} \mu_o H^2 A_g g \right] \quad (2.2)$$

or

$$\Delta W_{mag} = \mu_o H^2 A_g \Delta g \quad (2.3)$$

Due to conservation of energy, the change in magnetic energy is equal to the change in mechanical energy, so

$$\Delta W_{mech} = \Delta W_{mag} \quad (2.4)$$

where the change in mechanical energy for both gaps is $2*F*\Delta g$ and the change in magnetic energy is given by Equation 2.3. So, substituting into EQ. 4 gives

$$2F\Delta g = \mu_o H^2 A_g \Delta g \quad (2.5)$$

Solving for force in the equation above yields

$$F = \frac{\mu_o H^2 A_g}{2} \quad (2.6)$$

Using the definition of the permeability, B/μ_o can be substituted for H , resulting in the following force equation:

$$F = \frac{B^2 A_g}{2\mu_o} \quad (2.7)$$

where B is the magnetic flux density, A_g is the pole face area, and μ_o is the permeability of free space.

Because of the feedback nature of magnetic bearings, they are almost always arranged in an opposing pair configuration, also called a double-acting magnetic bearing configuration. In this configuration, the electromagnets pull against one another creating a net force. A schematic of a double-acting configuration is shown in Figure 2.2.

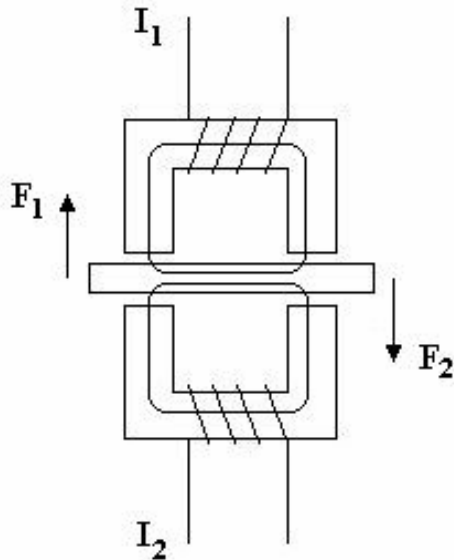


FIGURE 2.2: Schematic of a double-acting magnetic bearing

The net force on the target is the difference between F_1 and F_2 . So, the net force is given by:

$$F_{net} = F_1 - F_2 = \frac{A_g}{2\mu_o} (B_1^2 - B_2^2) \quad (2.8)$$

where B_1 is the magnetic flux density generated by I_1 and B_2 is the magnetic flux density generated by I_2 .

The force equation given in Equation 2.8 is based on simple magnetic circuit theory and does not include losses. Common losses in magnetic bearings include leakage and fringing. Leakage occurs when magnetic flux travels from one pole face to the other pole face without traveling through the target. Figure 2.3 demonstrates leakage losses.

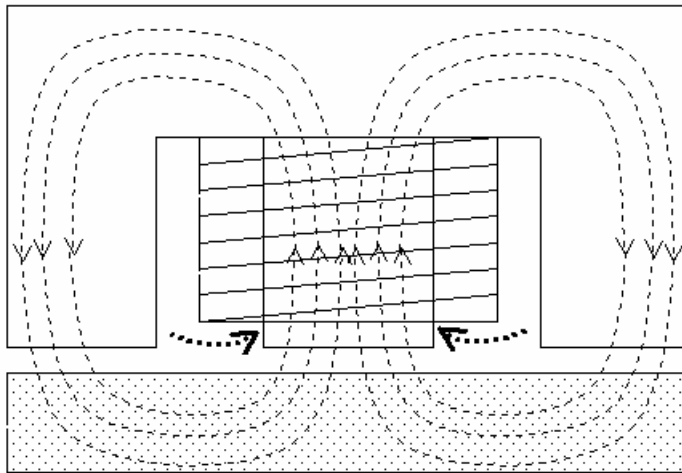


FIGURE 2.3: Diagram of leakage losses in a magnetic bearing

Because the magnetic flux density is measured directly using a Hall effect probe and not calculated using the relationship between current and flux density, leakage losses can be ignored. Fringing losses occur when magnetic flux does not travel directly from the pole face to the target, but “fringes” around the edges. This results in a larger effective air gap area because the flux is distributed throughout a larger area. A diagram illustrating fringing losses is shown in Figure 2.4.

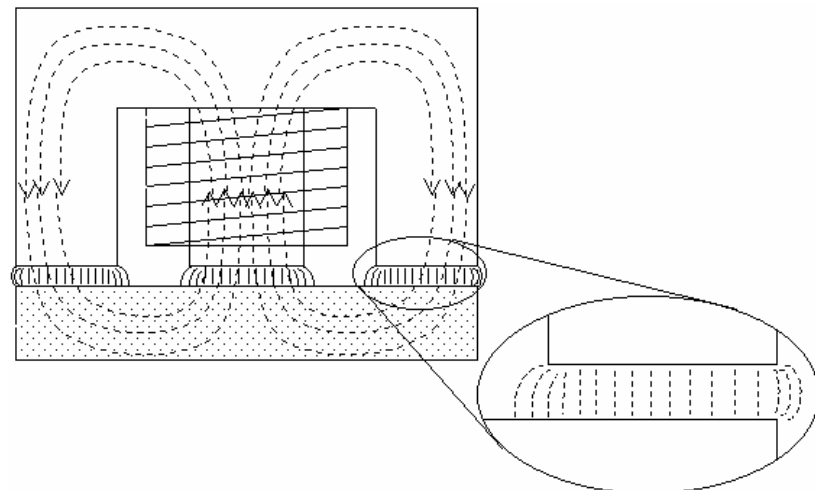


FIGURE 2.4: Diagram of fringing losses in a magnetic bearing

Fringing losses cannot be neglected because they are a strong function of air gap and bearing geometry as shown in the previous section on the development of the fringing factor. Assuming the flux probe is located in the center of the pole, the fringing factor corrects for losses due to fringing. So, including the flux based fringing factor (developed by Joe Imlach) in Equation 2.8 to account for fringing losses yields the final flux based force equation for a magnetic bearing:

$$F = \frac{A_g}{2\mu_0} (ff_1 B_1^2 - ff_2 B_2^2) \quad (2.9)$$

where ff_1 and ff_2 are the flux based fringing factors defined by the following equations:

$$ff_1 = A_b e^{-\alpha_b \left(\frac{g_o - x}{W} \right)} + K_b \quad (2.10)$$

$$ff_2 = A_b e^{-\alpha_b \left(\frac{g_o + x}{W} \right)} + K_b \quad (2.11)$$

and where g_o is the nominal gap between the actuator and target, x is the target position, and A_b , α_b , K_b , and W are constants from MFEA for the particular bearing geometry. Accurate forces are calculated using Equation 2.9 in conjunction with the flux based fringing factor equations.

2.3 Current Based Force Equations

The current based force equation for magnetic bearings can be derived using Kirchhoff's law for magnetic circuits and the flux based force equation derived in the previous section. Kirchhoff's law states that for any closed loop electrical circuit, the summation of voltage rises equals the summation of voltage drops; similarly, for a magnetic circuit, the summation of the magnetomotive force rises equals the summation of magnetomotive force drops. This can be written as

$$\sum NI - \sum \Re \phi = 0 \quad (2.12)$$

where N is the number of turns in the coil, I is the current in the coil, \mathfrak{R} is the reluctance of the magnetic path, and ϕ is the magnetic flux. Figure 2.5 shows a schematic of a simple magnetic circuit consisting of a ferromagnetic toroid with a concentrated winding.

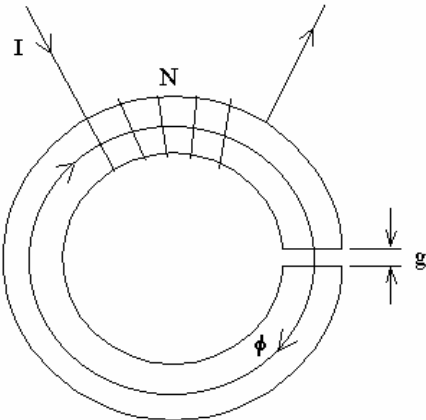


FIGURE 2.5: Schematic of ferromagnetic toroid with a concentrated winding

The reluctance is defined as the ratio of the magnetomotive force to flux. This relationship is represented by the following equation:

$$\mathfrak{R} = \frac{mmf}{flux} = \frac{\oint H \cdot dl}{\iint B \cdot dA} \quad (2.13)$$

where H is the magnetic field strength, l is the path taken along the toroid, B is the magnetic flux density, and A is the cross sectional area of the toroid. The total reluctance for this magnetic circuit is the summation of the reluctance of the iron and the reluctance of the air gap.

Assuming the magnetic field and cross-sectional area are uniform, the path length is the mean length along the middle of the iron, and the electromagnet is operating in the linear portion of the BH curve, the reluctance through the iron is given by:

$$\mathfrak{R}_i = \frac{L_i}{\mu_i A_t} \quad (2.14)$$

where L_i is the mean iron path length, μ_i is the permeability of the iron, and A_t is the cross-sectional area of the toroid. Assuming the magnetic field and cross-sectional area are uniform and the path length is the length of the air gap, the reluctance through the air gap is given by:

$$\mathfrak{R}_g = \frac{g}{\mu_o A_g} \quad (2.15)$$

where g is the gap length, μ_o is the permeability of free space, and A_g is the area of the gap.

The result after substituting the reluctance equations into Equation 2.12 is

$$NI = \phi_i \left(\frac{L_i}{\mu_i A_t} \right) + \phi_g \left(\frac{g}{\mu_o A_g} \right) \quad (2.16)$$

where N is the number of turns on the coil, I is the current through the coil, ϕ_i is the magnetic flux through the iron, and ϕ_g is the magnetic flux through the gap. If there is no leakage, the magnetic flux through the iron is equal to the magnetic flux through the gap; and if there is no fringing, the cross-sectional area of the toroid is equal to the area of the gap. After taking these assumptions into account and defining the relative permeability, μ_r , as μ_i/μ_o , Equation 2.16 simplifies to

$$NI = \frac{\phi}{A\mu_o} \left(\frac{L_i}{\mu_r} + g \right) \quad (2.17)$$

Magnetic flux density, B , is defined as the magnetic flux divided by the area it is distributed over. Making this substitution and solving for magnetic flux density yields

$$B = \frac{\mu_o NI}{\left(\frac{L_i}{\mu_r} + g \right)} \quad (2.18)$$

For two air gaps as in the case with a magnetic bearing, Equation 2.18 becomes

$$B = \frac{\mu_o NI}{\left(\frac{L_i}{\mu_r} + 2g \right)} \quad (2.19)$$

Now that the relationship between magnetic flux density and current has been determined, it can be substituted in the flux based force equation, Equation 2.9, derived in the previous section. So the net force in an opposing electromagnet configuration is given by

$$F_{net} = \frac{\mu_o N^2 A_g}{2} \left(\frac{I_1^2}{\left(\frac{L_i}{\mu_r} + 2g_1 \right)^2} - \frac{I_2^2}{\left(\frac{L_i}{\mu_r} + 2g_2 \right)^2} \right) \quad (2.20)$$

This equation, like the flux based force equation, is derived using simple magnetic circuit theory and does not include any losses. The assumptions inherent in Equation 2.20 are that the electromagnet is operating in the linear portion of the BH curve and that there is no leakage or fringing. In magnetic bearings, a bias current or permanent magnet is used to ensure that the electromagnet operates in the linear portion of the BH curve. Several design consideration such as over sizing the target can be made to minimize the effects of leakage; however, because fringing is a strong function of air gap and bearing geometry, it is not negligible. So, including the current based fringing factor (developed

by Joe Imlach) in Equation 2.20 to account for fringing losses yields the final current based force equation for a magnetic bearing yields Equation 2.21. The fringing factor equations for Equation 2.21 are given in Equations 2.22 and 2.23.

$$F_{net} = \frac{\mu_o N^2 A_g}{2} \left(\frac{ff_1 I_1^2}{\left(\frac{L_i}{\mu_r} + 2g_1 \right)^2} - \frac{ff_2 I_2^2}{\left(\frac{L_i}{\mu_r} + 2g_2 \right)^2} \right) \quad (2.21)$$

$$ff_1 = \frac{1}{2} \left[A_i e^{-\alpha_i \left(\frac{g_{o1}-x}{W_1} \right)} + K_i \left[A_i e^{-\alpha_i \left(\frac{g_{o1}-x}{W_2} \right)} + K_i \right] \right. \\ \left. + \frac{1}{2} \left[A_i e^{-\alpha_i \left(\frac{g_{o2}-x}{W_3} \right)} + K_i \left[A_i e^{-\alpha_i \left(\frac{g_{o2}-x}{W_4} \right)} + K_i \right] \right] \right] \quad (2.22)$$

$$ff_2 = \frac{1}{2} \left[A_i e^{-\alpha_i \left(\frac{g_{o1}+x}{W_1} \right)} + K_i \left[A_i e^{-\alpha_i \left(\frac{g_{o1}+x}{W_2} \right)} + K_i \right] \right. \\ \left. + \frac{1}{2} \left[A_i e^{-\alpha_i \left(\frac{g_{o2}+x}{W_3} \right)} + K_i \left[A_i e^{-\alpha_i \left(\frac{g_{o2}+x}{W_4} \right)} + K_i \right] \right] \right] \quad (2.23)$$

In Equations 2.22 and 2.23, g_{o1} is the nominal gap for the outer legs of the actuator; g_{o2} is the nominal gap for the center leg of the actuator; x is the target position; and A_i , α_i , K_i , W_1 , W_2 , W_3 , and W_4 are constants from MFEA for the particular bearing geometry. The gaps g_1 and g_2 in Equation 2.21 are often replaced by the nominal gap, g_o , plus and minus the target position, x . So Equation 2.21 can be rewritten as follows:

$$F = \frac{\mu_o N^2 A_g}{2} \left(\frac{ff_1 I_1^2}{\left(\frac{L_i}{\mu_r} + 2(g_o - x) \right)^2} - \frac{ff_2 I_2^2}{\left(\frac{L_i}{\mu_r} + 2(g_o + x) \right)^2} \right) \quad (2.24)$$

In Equation 2.24, g_o is the average of g_{o1} and g_{o2} . Accurate forces can be calculated using Equation 2.24 in conjunction with the current based fringing factor equations given in Equations 2.22 and 2.23.

Chapter 3

Experimental Description

3.1 Overview of TMS Demonstrator

A TMS demonstrator was designed in order to prove the capability of using magnetic bearings in a magnetically levitated thrust measurement system. Joe Imlach designed the test rig and magnetic bearing components, while Virginia Tech's role has been the application of the multipoint calibration technique including code development, the implementation of a 128-channel data acquisition system, and the overall test verification of the TMS demonstrator. There are six main components to the TMS demonstrator: the fixed frame, the floating frame, four support bearings, seven thrust bearings, three controllers, and the data acquisition (DAQ) system. The frame for the demonstrator is assembled from commercially available precision aluminum extruded structural elements (Mini-Tec Framing Systems, LLC; Canandaigua, NY). This simplified the design and construction of the test rig and allows for maximum flexibility of future uses of the demonstrator for actual testing. The fixed frame is essentially a rectangular box (0.70 m x 0.70 m x 0.92 m) [27.5 in x 27.5 in x 36.4 in], with three additional axial members in both the top and bottom plane. The floating frame is located inside the fixed frame and rests on bolts that act as backup bearings to support the weight of the floating frame while the frame is not levitated. A schematic of the test rig is shown in Figure 3.1.

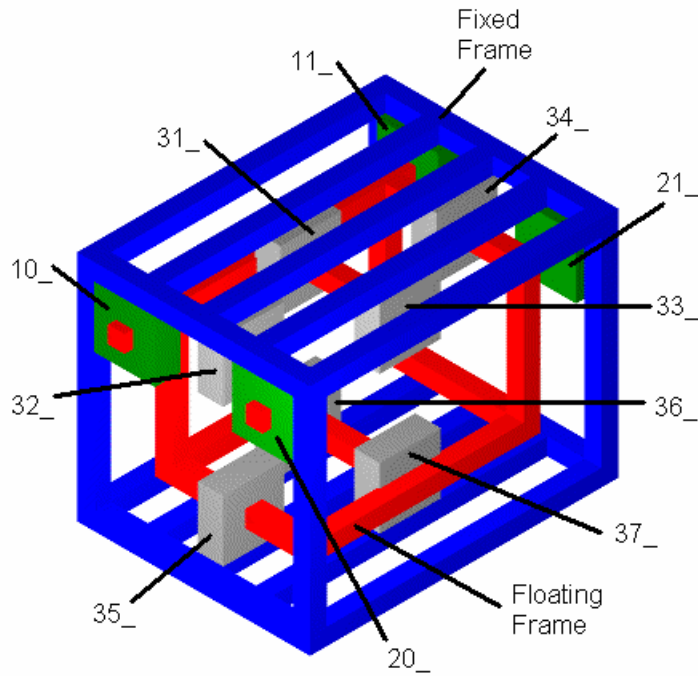


Figure 3.1: Schematic of TMS Demonstrator

The fixed frame, floating frame, support bearings, and thrust bearings can be seen in Figure 3.1. The fixed frame is shown in blue, the floating frame is shown in red, the support bearings are shown in green, and the thrust bearings are shown in grey. The numbering scheme for the magnetic bearings is also shown in Figure 3.1. The front support bearings are numbered 10_{_} and 20_{_} and the back support bearings are numbered 11_{_} and 21_{_}. The top thrust bearings are numbered counterclockwise starting with 31_{_} on the left and going around to 34_{_} in the back. The original number scheme for the bottom thrust bearings was 35_{_}, 36_{_}, 37_{_} (going counterclockwise from the left); however, thrust bearing 35_{_} was unusable due to instability issues. Thus, bearings 35_{_} and 36_{_} were switched to maintain symmetric reaction forces on the floating frame. The resulting number scheme for the bottom thrust bearings was 36_{_}, 35_{_}, 37_{_} (going counterclockwise from the left) after the swap was made.

A picture of the TMS demonstrator is shown in Figure 3.2. The demonstrator is shown in the foreground while the controllers and data acquisition system are shown in

the background. The individual components of the TMS demonstrator will now be discussed in more detail.

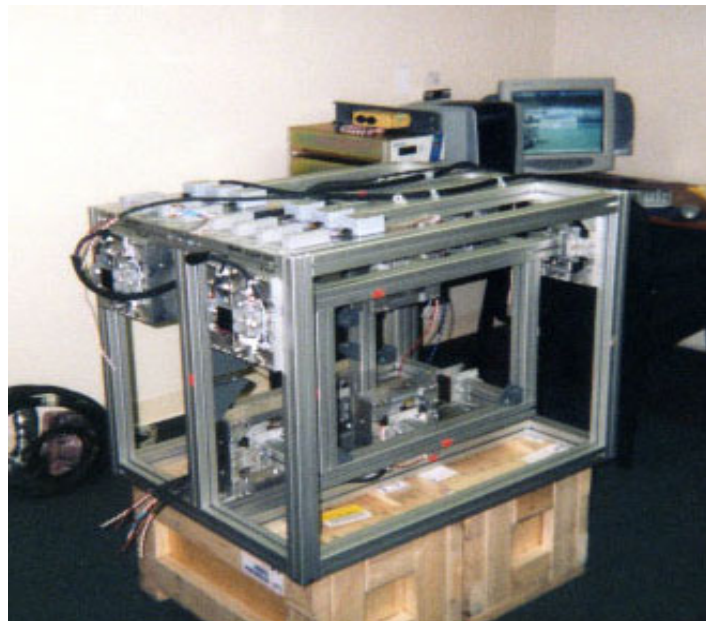


Figure 3.2: Picture of TMS Demonstrator

Four support bearings in the top four corners of the test rig levitate and measure forces applied in the x- and y-directions. The weight of the rig as well as side loading is measured by the support bearings. Each support bearing has two axes, a horizontal and a vertical, as seen in the schematic in Figure 3.3.

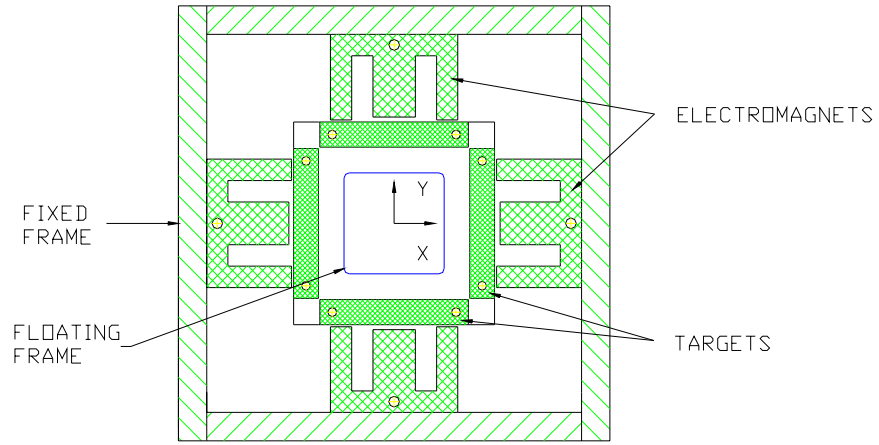


Figure 3.3: Schematic of Support Bearing (schematic provided by Joe Imlach)

There are also seven thrust bearings located in the center of the test rig that levitate and measure forces applied in the z- or thrust direction. Each thrust bearing has only one axis of support. Figure 3.4 shows a schematic of one of the thrust bearings from the TMS demonstrator.

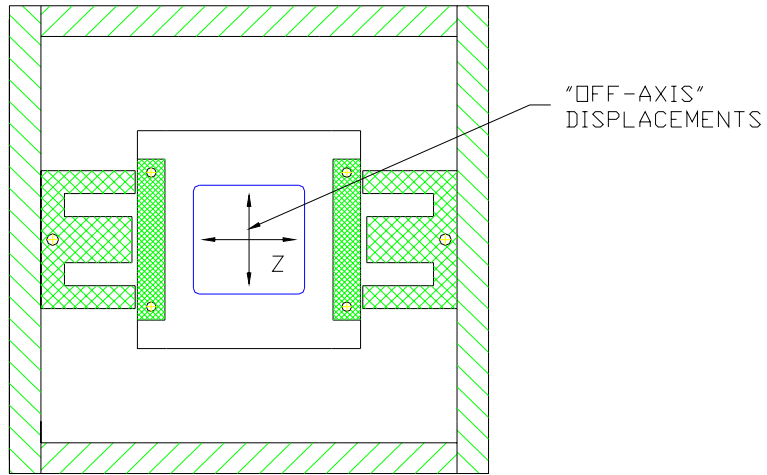


Figure 3.4: Schematic of Thrust Bearing (schematic provided by Joe Imlach)

The targets are attached to the floating frame and the actuators are attached to the fixed frame so that the floating frame is completely levitated within the fixed frame by the

magnetic bearings. Thus the floating frame is completely supported by 15 axes: four in the x-direction and four in the y-direction by the support bearings, and seven in the z-direction by the thrust bearings.

A magnetic bearing axis, or axis of support, consists of two actuators, a target, and a differential proximity sensor to measure the relative position of the target. The proximity sensors provide the high accuracy position measurements needed by the controllers to keep each target levitated within the actuators. Each actuator is also equipped with a thermistor to measure the coil temperature and a Hall effect flux sensor to measure the flux density in the air gap between the actuator and target.

Pictures of the support and thrust bearings are shown in Figure 3.5. The target and actuators can be seen clearly in the picture of the thrust bearing shown on the right while the circuit boards that house the electronics for the flux probe and thermistors as well as the eddy current position sensors (with yellow tips) can be seen in the picture of the support bearing shown on the left. These components are discussed in more detail in the hardware section of the DAQ system.

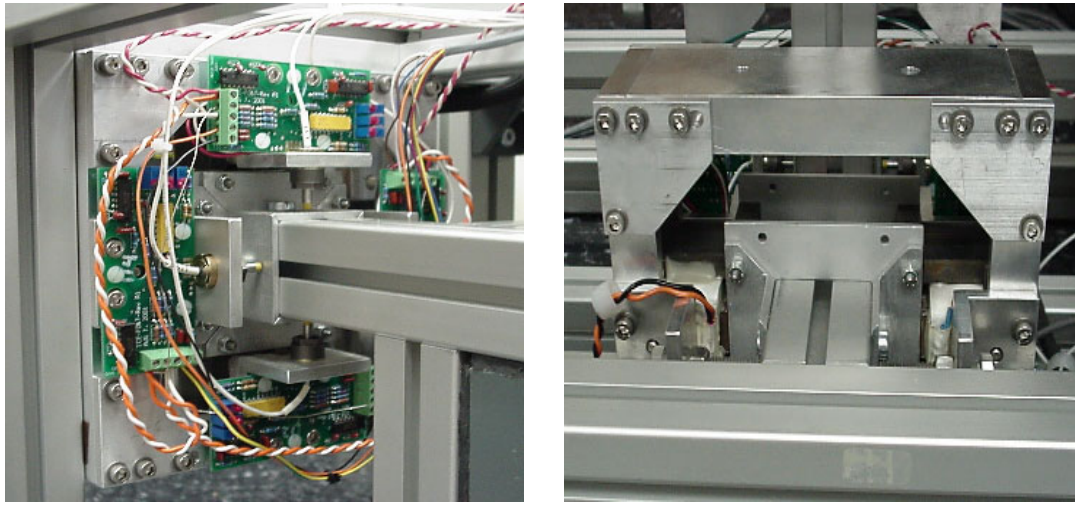


Figure 3.5: Support Bearing (left) and Thrust Bearing (right)

The wires providing current to the actuators as well as the proximity sensor outputs are connected to three Revolve controllers. Each controller has the capability of

supporting five axes. Controller 1(A) controls the two left support bearings as well as the left center thrust bearing (bearings 10_{_}, 11_{_}, and 31_{_} as seen in Figure 3.1); Controller 2(B) controls the right two support bearings as well as the right center thrust bearing (bearings 20_{_}, 21_{_}, and 33_{_} as seen in Figure 3.1); and Controller 3(C) controls the remaining thrust bearings (bearings 32_{_}, 34_{_}, 35_{_}, 36_{_}, and 37_{_} as seen in Figure 3.1).

The coil currents and target positions as well as the coil temperatures and flux probe readings are all inputs to the DAQ system. The DAQ system acquires and processes these signals to calculate accurate forces being applied to the TMS demonstrator.

3.2 Data Acquisition (DAQ) System

The main hardware components of the DAQ system are discussed first followed by an overview of the DAQ software used to measure forces. Most of the DAQ components including the software package, LabVIEW 6.1, were purchased from National Instruments. The DAQ system has the capability of sampling 128 channels, however only 106 of those channels are used for the TMS demonstrator.

3.2.1 Data Acquisition Hardware

J. Imlach and R. Kipp, in conjunction with National Instruments personnel, designed the DAQ system used for the thrust measurement system. Table 3.1 summarizes the National Instruments components that were purchased for the DAQ system.

Table 3.1: Summary of National Instruments Components

| Item | Number of Items Used in DAQ System |
|--|---------------------------------------|
| PCI-6032E data acquisition card for PC | 1 |
| SCXI-1000 chassis | 1 |
| SCXI-1102C module | 4 |
| SCXI-1300 connector | 2 |
| SH 96-96 cables | 2 |
| BNC-2095 BNC connector boxes | 2 |

There are 15 axes of control, each consisting of two opposing electromagnetic actuators, monitored by the DAC system. Each axis consists of two flux measurements, one for each actuator; two temperature measurements; two current measurements; and one position measurement. The DAC system uses 106 of the 128 channels available: 30 for flux densities, 30 for temperatures, 30 for currents, 15 for positions, and one channel for load cell measurements.

FH-560 Hall effect flux probes manufactured by F. W. Bell are used to measure flux density in each actuator. These sensors are high gain (high sensitivity) devices, and were each individually calibrated using a magnetic calibration chamber. The Hall effect sensors have an operating range from -55 to $+100$ C. The thermistors are YSI model #44201 devices. Each thermistor package includes two thermistors (NTC and PTC) along with two precision resistors that mount on a custom printed circuit board (PCB). The combination results in a linear output over the range of 0 to 100 °C. The thermistors are mounted between the coil and the center leg of the E-core and are used to measure the temperature of the coil for each actuator. A custom PCB containing the driver and conditioning circuits for the thermistors and the Hall sensors is mounted by each electromagnet.

The current data is obtained through outputs from the Revolve MBResearch hardware supplied with the controllers. Differential eddy current proximity sensors manufactured by Kaman Instrumentation are used to measure the relative target position. This position data is also obtained through the outputs from the MBResearch hardware.

The flux and temperature outputs are wired from the circuit boards located at each actuator to the black terminal block box located on top of the thrust measurement system. These wires are bundled and hardwired into the SCXI-1300 connector from National Instruments. The SCXI-1300 connector plugs into the SCXI-1102C module mounted to the SCXI-1000 chassis from National Instruments. The PC addresses the flux and temperature channels using the PCI-6032E data acquisition card.

The current and position outputs from the MBResearch hardware are connected to the BNC-2095 using BNC cables. The SH 96-96 cables connect the BNC-2095s to the SCXI-1102C modules mounted to the SCXI-1000 chassis. The PC addresses the current and position channels using the PCI-6032E data acquisition card.

LabVIEW 6.1 was used as a software interface. In particular, the Measurement and Automation Explorer supplied with the LabVIEW 6.1 software provides for simple channel configuration. The channels have been set up to include all of the flux density, temperature, current, and position measurements for the 15 axes currently on the rig and extra channels for measurements on another axis if added in the future. The channels are named C1-C113: C1-C16 are position channels with an output range of $\pm 2.5V$, C17-C48 are current channels with an output range of 0-10V, C49-C80 are flux density channels with an output range of $\pm 10V$, C81-C112 are temperature channels with an output range of 0-10V, and C113 is the load cell channel with an output range of $\pm 10V$. The LabVIEW software is used to control the data acquisition of all the channels.

3.2.2 Data Acquisition Software

LabVIEW 6.1 is the software platform used for control of the data acquisition for the thrust measurement system (TMS). LabVIEW is a graphically based, user-friendly programming language. Each program, called a Virtual Instrument (VI) is composed to two main interfaces: the front panel and the block diagram. Program names in future sections may have a “VI” following the program name noting it as a virtual instrument program. The front panel is the user interface of the VI. This panel is designed first in the programming process and includes any inputs needed by the user and outputs such as graphs, indicators, or filenames for saving data. A sample front panel is shown in Figure 3.6.

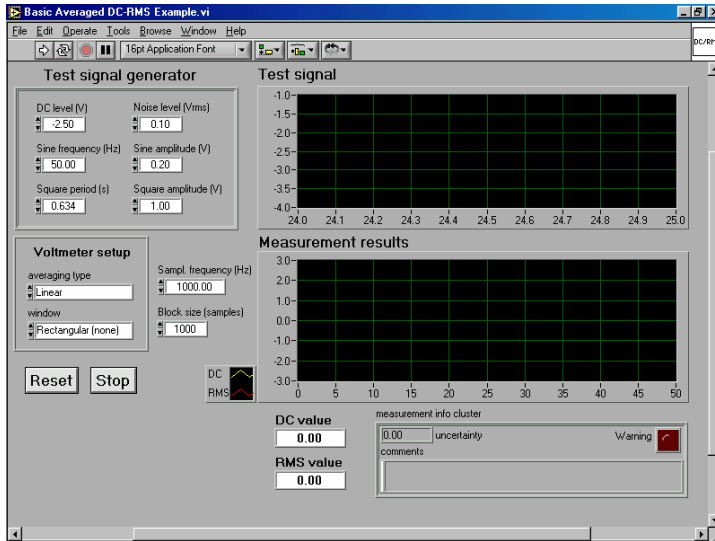


Figure 3.6: Sample LabVIEW 6.1 Front Panel

This then generates blocks in the block diagram that can be connected using wires to control data flow. The block diagram shows the flow of data and all the data processing that is done in the VI. VIs can be called as subroutines in other VIs to simplify block diagrams and wiring. A sample block diagram is shown in Figure 3.7.

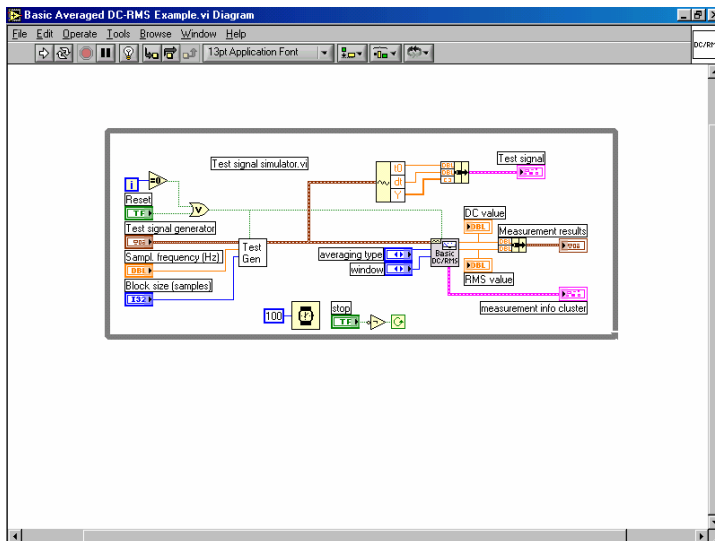


Figure 3.7: Sample LabVIEW 6.1 Block Diagram

The VIs written for the TMS are broken down into three main groups: calibration programs, static force acquisition programs, and dynamic force acquisition programs.

The three main groups are further broken down into two procedures: the setup procedure and the main program. The flowchart in Figure 3.8 shows the step-by-step procedure that the user performs for either static or dynamic force acquisition.

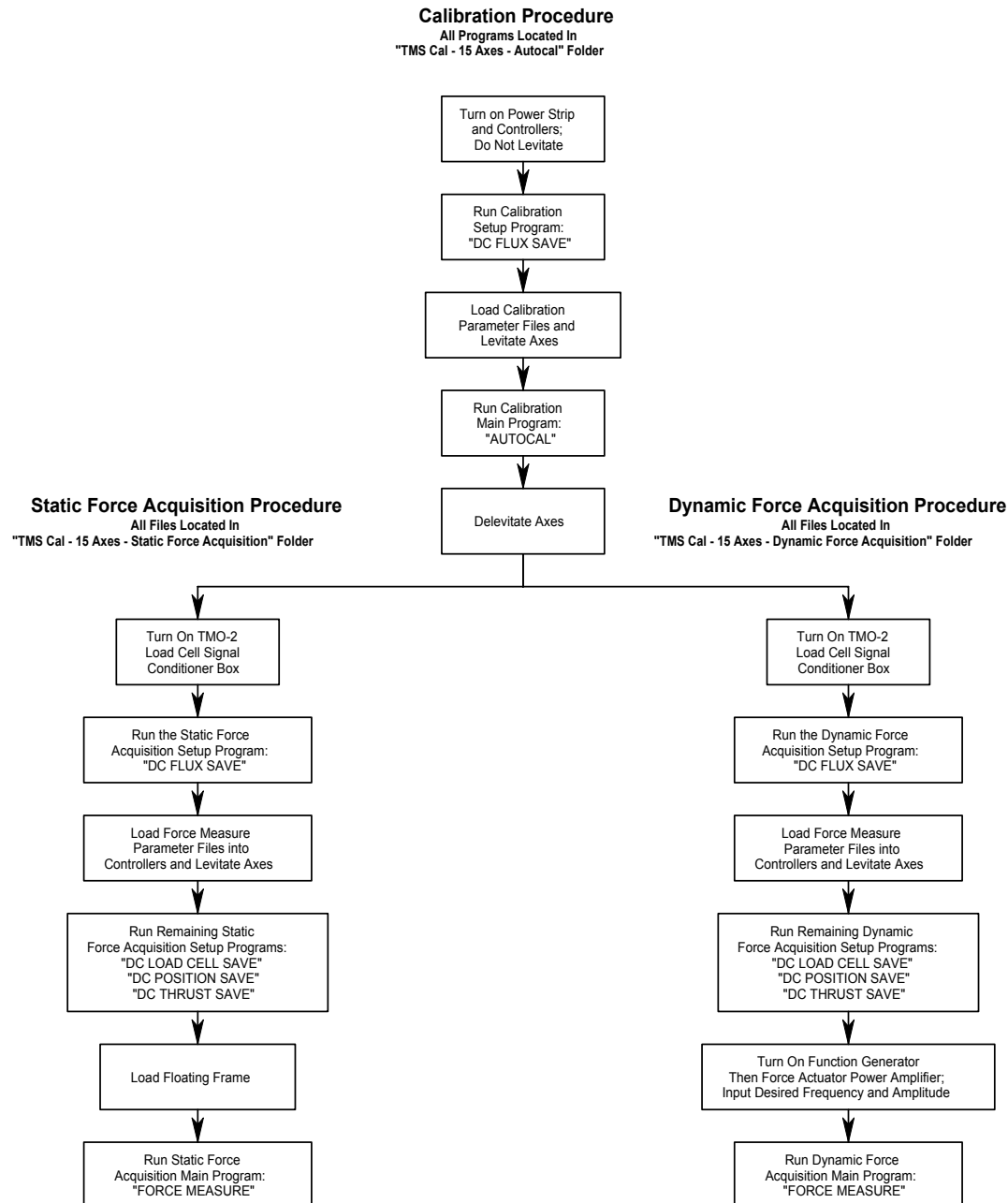


Figure 3.8: Flowchart of three main groups of programs

The calibration programs perform the multipoint method on all 15 axes of the TMS and record the predicted target positions of each axis for use in subsequent static and dynamic force calculations. The static force acquisition programs calculate, display, and record static forces applied to the floating frame of the TMS. The dynamic force acquisition programs calculate, display, and record dynamic forces in real time applied to the floating frame. These three main groups of VIs are discussed in more detail in the next three chapters.

3.3 Static Force Acquisition

The calibration procedure, described in the next chapter, must be completed prior to static force acquisition because the predicted target positions are needed for force calculations. The static force acquisition programs calculate, display, and record static forces applied to the floating frame of the TMS. There are four programs used in the setup procedure for static force acquisition: “DC FLUX SAVE,” “DC LOAD CELL SAVE,” “DC POSITION SAVE,” and “DC THRUST SAVE.” All of the files for these programs are found in the “TMS Cal – 15 Axes – Static Force Acquisition” folder. After the setup procedure, the “FORCE MEASURE” VI is used to calculate the static forces applied to the floating frame. “FORCE MEASURE” uses the files created by the programs from the setup procedure along with the predicted target position results from the calibration procedure to calculate accurate static forces.

Axial forces are applied to the test rig using a turnbuckle assembly that connects the fixed frame to the floating frame. Figure 3.9 shows the turnbuckle assembly connecting the fixed and floating frames. An MLP-300 load cell manufactured by Transducer Techniques is connected in series with the turnbuckle to measure the actual force applied. The output from the load cell, the actual force applied, is then compared to the results from the “FORCE MEASURE” VI, the measured force applied.

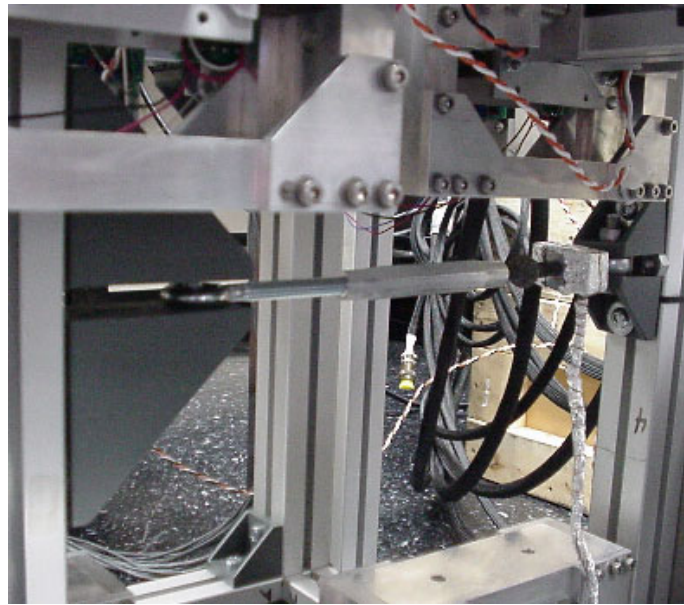


Figure 3.9: Turnbuckle Assembly for Static Testing

Static forces measurements must have errors less than 0.5% as determined by NASA STTR Phase II objectives. The full load is the maximum load of each bearing multiplied by the total number of thrust bearings used. Different numbers of thrust bearings can be turned on or off to calculate accurate forces for various axial loads.

3.3.1 Setup Procedure

Several steps must be completed prior to running the “FORCE MEASURE” VI for determination of static forces. For the laboratory setup, the load cell conditioner electronics require a 15-minute warm-up time before load measurements can be taken, so the TMO-2 load cell signal conditioner should be turned on first. The load cell must be loaded in tension for static measurements because the turnbuckle assembly cannot guarantee proper loading of the load cell in compression. Errors may arise from side loading of the load cell if it is used in compression. For that reason, the load cell assembly should be mounted in the direction the user desires to pull the floating frame.

With the circuit boards powered and the floating frame delevitated, the user must click the “Run” arrow of the “DC FLUX SAVE” VI. This program records the flux density voltage outputs from the circuit boards when the flux in the actuators is zero.

These voltages are subtracted from subsequent flux density measurements to find the actual flux density through each actuator. If the calibration procedure was just completed and the “dcflux.dat” file is still in the “15 Axes” folder on the computer desktop, then it is not necessary to run the “DC FLUX SAVE” VI.

The correct parameter files must then be loaded into the Revolve controllers before the floating frame is levitated. Even if the calibration procedure was just completed, new parameter files using a bias current of 1.1 amps must be loaded into the controllers. “Controller 1(A) V20 Bias 1-1,” “Controller 2(B) V20 Bias 1-1,” and “Controller 3(C) V20 Bias 1-1 35 Off” from the “Forcemeasure PVF Files” folder should be loaded into controllers 1(A), 2(B), and 3(C), respectively, using the “Parameter Loader” program. The floating frame is then levitated by pressing the green “Start” buttons located on the front panels of the Revolved controllers.

The system must now be allowed to reach a steady state in which all the axes are levitated and centered. The MBScope “Snapshots” software supplied by Revolve allows the user to view the positions of each axis for the controller selected by the data switch. The positions of the axes are plotted in real time by clicking on the “Channels” drop down menu and selecting “Positions.” To view the numerical values instead of the plots of the positions, the user can click on the “View” drop down menu and select “Statistics.” When all of the positions of all three controllers are fluctuating within the hundredths of a micron (μm) range, the system has reached steady state. It takes about two minutes for the system to reach steady state.

With the floating frame levitated but still unloaded, the user must run the “DC LOAD CELL SAVE,” “DC POSITION SAVE,” and “DC THRUST SAVE” VIs. “DC LOAD CELL SAVE” saves the output voltage of the load cell when the cell is unloaded. This is typically a small voltage; however, because of the accuracy needed in the force measurements, it is not negligible. This voltage will be subtracted from future load cell measurements converted to pounds to find the actual force being applied to the load cell. “DC POSITION SAVE” saves the DC position output voltages for all the actuators.

These values will be subtracted from future position measurements and the result will be converted to inches, yielding the position of the target. These target positions are added to the predicted target position and used in the force calculations of “DC THRUST SAVE” and “FORCE MEASURE.” “DC THRUST SAVE” saves the forces that all the actuators experience when the floating frame is unloaded (i.e. the turnbuckle is not tightened). This allows the “FORCE MEASURE” VI to calculate the resultant force applied to the floating frame because the load applied by the turnbuckle assembly is not purely axial. The resultant is calculated using Equation 3.1 shown below.

$$F_{result} = \sqrt{(\sum F_x - \sum F_{DCx})^2 + (\sum F_y - \sum F_{DCy})^2 + (\sum F_z - \sum F_{DCz})^2} \quad (3.1)$$

In this equation ΣF_x , ΣF_y , ΣF_z are the sums of the forces in the x, y, and z directions from the “FORCE MEASURE” VI and ΣF_{DCx} , ΣF_{DCy} , ΣF_{DCz} are the sums of the forces in the x, y, and z directions from the “DC THRUST SAVE” VI. The setup procedure is now finished and the TMS is ready for static force acquisition.

3.3.2 Static Force Acquisition Procedure

When the “Run” arrow on the “FORCE MEASURE” VI is pressed, flux densities, currents, and positions are sampled at 1024Hz and averaged over 2048 samples. Therefore data is being taken for a total of two seconds. This means that the static load must remain constant for the two seconds during data acquisition for accurate force measurements using the “FORCE MEASURE” VI. The force applied to the floating frame by the turnbuckle assembly can be calculated using Equation 3.2.

$$F_{LC} = (V_{LC} - V_{DCLC}) * 30 \frac{lb}{V} \quad (3.2)$$

In Equation 3.2, V_{LC} is the output voltage from the TMO-2 load cell signal conditioning box, V_{DCLC} is the DC load cell value from the “DC LOAD CELL SAVE” VI, and 30 lb/V is the conversion factor for the TMO-2 box. The turnbuckle is tightened to the desired axial load according to EQ. 2 using an 11/16” box-end wrench on the shaft coming from

the load cell to keep the load cell from turning and a 5/8" box-end wrench on the turnbuckle. While the desired load is applied, the user must remove the wrenches and press the "Run" arrow on the "FORCE MEASURE" VI to begin the static force acquisition. The "FORCE MEASURE" VI displays the total forces and moments experienced by the floating frame. Figure 3.10 shows the section of the "FORCE MEASURE" VI front end that displays the forces calculated by the program.

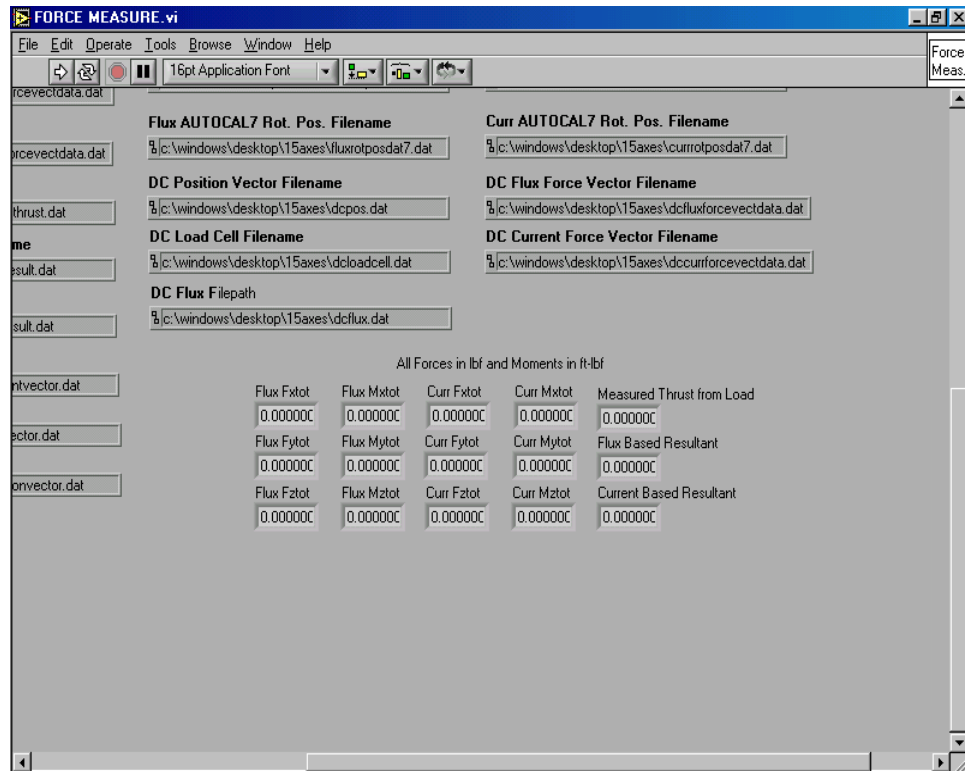


Figure 3.10: Front Panel of "FORCE MEASURE" VI

Total moments for the floating frame are summed about the center of bearing 32_ as shown in the schematic in Figure 3.1. The fluxes, currents, and positions used to calculate the forces along with the forces in each axis and resultant forces are saved to the "15axes" folder on the computer desktop. The error is calculated using Equation 3.3.

$$\% \text{ Error Full Load} = \frac{(F_{\text{result}} - F_{LC})}{N * 37.77 \text{lb}} \quad (3.3)$$

F_{result} is either the flux or current based resultant force in pounds, F_{LC} is the corrected force from the load cell, N is the number of energized thrust bearings, and $37.77lb$ is the load capacity of each thrust bearing. After the setup procedure is complete, “FORCE MEASURE” can be run any number of times with different loads while levitated and the new data will be appended to the output files.

3.4 Dynamic Force Acquisition

The calibration procedure, described in the next chapter, must be completed prior to dynamic force acquisition because the predicted target positions are needed for force calculations. The dynamic force acquisition programs calculate, display, and record dynamic forces applied to the floating frame in real time. There are four programs used in the setup procedure for dynamic force acquisition: “DC FLUX SAVE,” “DC LOAD CELL SAVE,” “DC POSITION SAVE,” and “DC THRUST SAVE.” All of the files for these programs are found in the “TMS Cal – 15 Axes – Dynamic Force Acquisition” folder. After the setup procedure, the “FORCE MEASURE” VI is used to calculate the dynamic forces applied to the floating frame. This program uses the files created by the programs from the setup procedure along with the predicted target position results from the calibration procedure to calculate accurate forces. A magnetostrictive force actuator (Terfenol-D actuator model #AA140J013-ES1; Etrema Products, Inc.) using a function generator to provide the input signal is used to apply dynamic loads. An MLP-300 load cell manufactured by Transducer Techniques is connected in series with the force actuator to measure the actual force applied. The output from the load cell, the actual force applied, is then compared to the results from the “FORCE MEASURE” VI, the measured force applied, to calculate the error. Dynamic forces measurements must have full load errors less than 0.5% as determined by NASA STTR Phase II objectives. The full load is the maximum load of each bearing multiplied by the total number of thrust bearings used. Different numbers of thrust bearings can be turned on or off to calculate accurate forces for various axial loads.

3.4.1 Setup Procedure

The setup procedure for dynamic force acquisition is similar to that of the static force acquisition. The load cell conditioner electronics require a 15-minute warm-up time before load measurements can be taken, so the TMO-2 load cell signal conditioner should be turned on first. For the dynamic loading case, the magnetostrictive force actuator replaces the turnbuckle of the static loading case. Figure 3.11 shows the dynamic testing setup using the magnetostrictive force actuator. The load cell must be preloaded in tension while the floating frame is levitated to ensure proper loading. As with the static loading case, errors may arise from side loading of the load cell if it is used in compression.

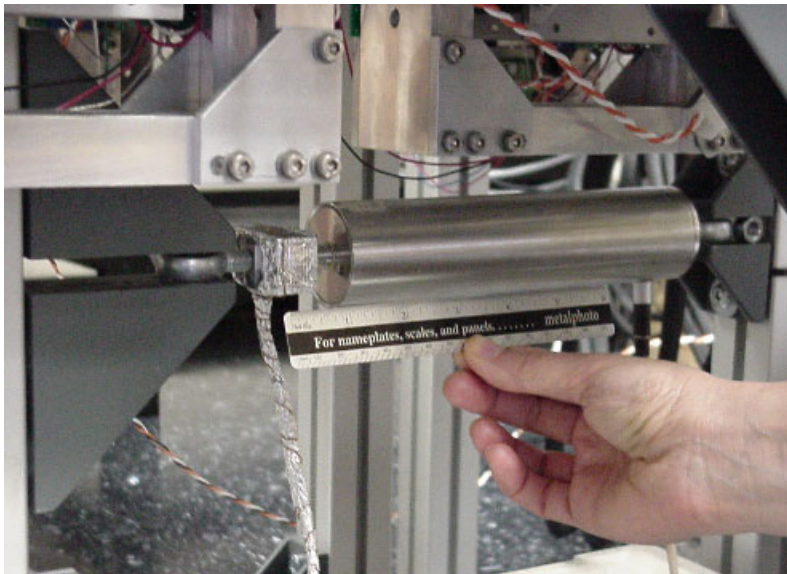


Figure 3.11: Magnetostrictive Actuator Assembly for Dynamic Testing

With the circuit boards powered and the floating frame delevitated, the user must click the “Run” arrow of the “DC FLUX SAVE” VI. This program saves the DC flux density values for all of the actuators. These values will be subtracted from future flux density measurements to determine the actual flux density. If the calibration procedure was just completed and the “dcflux.dat” file is still in the “15 Axes” folder on the computer desktop, then it is not necessary to run the “DC FLUX SAVE” VI.

The correct parameter files must then be loaded into the Revolve controllers before the floating frame is levitated. Even if the calibration procedure was just completed, new parameter files using a bias current of 1.1 amps must be loaded into the controllers. “Controller 1(A) V20 Bias 1-1 Thrust Off,” “Controller 2(B) V20 Bias 1-1 Thrust Off,” and “Controller 3(C) V20 Bias 1-1 35 Off” from the “Forcemeasure PVF Files” folder should be loaded into controllers 1(A), 2(B), and 3(C), respectively, using the “Parameter Loader” program. Then, only Controllers 1(A) and 2(B) should be levitated by pressing the green “Start” button on the front panels of the controllers.

The system must now be allowed to reach a steady state in which all the axes are levitated and centered. The MBScope “Snapshots” software supplied by Revolve allows the user to view the positions of each axis for the controller selected by the data switch. The positions of the axes are plotted in real time by clicking on the “Channels” drop down menu and selecting “Positions.” To view the numerical values instead of the plots of the positions, the user can click on the “View” drop down menu and select “Statistics.” When all of the positions of all three controllers are fluctuating within the hundredths of a micron (μm) range, the system has reached steady state. It takes about two minutes for the system to reach steady state.

With the floating frame levitated but still unloaded, the user must run the “DC LOAD CELL SAVE,” “DC POSITION FOR DC THRUST SAVE,” and “DC THRUST SAVE” VIs. These programs save data files needed by the “FORCE MEASURE” VI to calculate the forces in each axis.

The thrust bearings must be energized before running the next setup LabVIEW VI. First, the user must turn on Controller 3(C) by pressing the green “Start” button on the front panel of the controller. Then, new parameter files must be loaded into Controllers 1(A) and 2(B). “Controller 1(A) V20 Bias 1-1” and “Controller 2(B) V20 Bias 1-1” from the “Forcemeasure PVF Files” folder should be loaded into Controllers 1(A) and 2(B), respectively. All of the thrust bearings are now energized.

The system must again be allowed to reach a steady state in which all the axes are levitated and centered. The MBScope “Snapshots” software, can be used as described above to determine when the system has reached steady state. When all of the positions of all three controllers are fluctuating within the hundredths of a micron (μm) range, steady state has been achieved. This takes approximately two minutes. The setup procedure is now finished and the TMS is ready for dynamic force acquisition.

3.4.2 Dynamic Force Acquisition Procedure

A couple of general principles for signal processing can be used to determine the sampling parameters that should be used for dynamic force acquisition. The highest frequency component expected in a typical rocket TMS is 30 Hz, but to be conservative, 50 Hz was used. Sampling at 10 to 20 times the frequency of the waveform results in a good reproduction of the shape of the waveform. Thus, sampling a 50 Hz waveform at a rate of 1000 samples per second is sufficient. At least three cycles of waveform should be sampled, so at least 60 samples ($3*20$) should be taken of a waveform sampled at 20 times its frequency. To ensure enough cycles of the waveform are sampled, 300 samples were acquired in the “FORCE MEASURE” VI. This means that with an input waveform of 30 Hz taking 300 samples and sampling at a rate of 1000 Hz, nine complete cycles of the waveform will be captured $\left(\frac{30*300}{1000}\right)$.

For the laboratory set up a magnetostrictive force actuator is used to load the system for testing. The function generator connected to the force actuator controls the magnitude and frequency of the input force. The function generator should be turned on first with amplitude set to zero to prevent damage to the force actuator and magnetic bearings. It is then safe to turn on the power amplifier of the force actuator. The amplitude and frequency of the input signal can be adjusted to the desired values using the function generator. Data acquisition begins when the “Run” button on the “FORCE MEASURE” VI is pressed. Three-tenths of a second of data is acquired $\left(\frac{300\text{samples}}{1000\text{samples/sec}}\right)$ and total forces and moments applied to the rig in that time are

plotted and saved. Total moments for the floating frame are summed about the center of bearing 32_ as shown in Figure 3.1. The fluxes, currents, and positions used to calculate the forces along with the forces in each axis and resultant forces are saved to the “15axes” folder on the computer desktop.

The purpose of these tests is to prove that the TMS demonstrator is capable of dynamic force acquisition. Because of the inertia of the floating frame, there is a time lag as well as a magnitude shift between the resultant force from the magnetic bearings and the measured force from the load cell. This time lag is dependent on the mass of the floating frame as well as the acceleration of the floating frame. The TMS demonstrator is not equipped with accelerometers, so the time lag and magnitude shift cannot be corrected in the force data for the TMS demonstrator. Hence, the conclusions about the dynamic results will be more qualitative than quantitative.

Chapter 4

Calibration of TMS Demonstrator

4.1 Introduction

Both the current and flux based force equations for magnetic bearings include a physical air gap term. In the flux based method, this term is found only in the fringing factor equations (see Equations 2.9 through 2.11). In the current based method, the target position term is found in both the force equation and the fringing factor equations (see Equations 2.22 through 2.24). Therefore, it is necessary to determine air gaps for accurate force measurements with either method. Position sensors exist but they are only able to determine a target position relative to the position sensor and do not indicate a bearing/actuator gap that may be a function of temperature, alignment, and machining tolerances. Previous methods of identifying physical air gaps involve using feeler gauges to physically measure the gap between the actuator and the target. Other calibration methods involve applying known loads to the bearings to calculate a correction factor. One goal of this work is to develop a robust calibration that can be completely automated allowing it to be used in a field situation. In order to meet this goal, a system identification method, called the multipoint method, has been developed.

4.2 The Multipoint Algorithm

The multipoint method was originally developed as a new current based force measurement methodology that inherently accounts for system uncertainties by utilizing multiple sets of current pairs in opposing actuators, in conjunction with a calculation algorithm, to accurately determine the force applied by the AMB. In the TMS scenario, the multipoint method is used as a calibration to determine air gaps for use in fringing

models and force equations. The multi-point force measurement technique takes advantage of the fact that an AMB feedback system will keep the supported target at a predetermined fixed location between two opposing actuators with great accuracy. The multiple points required by the technique are obtained by increasing the current into one side of the double-acting actuator in small increments and recording the currents for both sides of the actuator for each of these increments after initial transients are dissipated and the target is re-centered within the actuator. This is simply performed by adding a perturbation current to the control effort already levitating the load as shown in Figure 4.1. Alternatively, the bias current in both actuators can be modified so that the same perturbation is achieved. Because of the controller and software used in the TMS test rig, the bias current perturbation method is used to perturb the thrust measurement system.

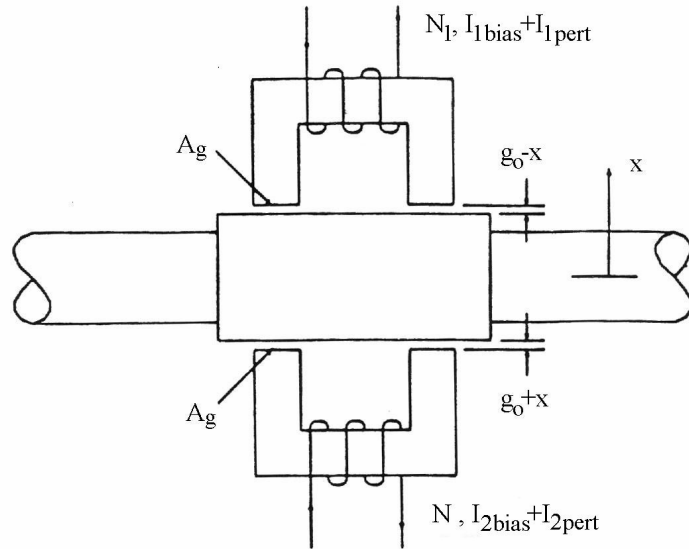


Figure 4.1: Schematic of double-acting single axis magnetic bearing

The total current in each coil is the summation of the bias current and perturbation current. The bias current is used to ensure that the actuator is operating in the linear portion of the B-H curve. The B-H curve for a typical magnetic material is shown in Figure 4.2 where the extended line indicates the linear portion. The perturbation current is injected by the controller to maintain the centered target position.

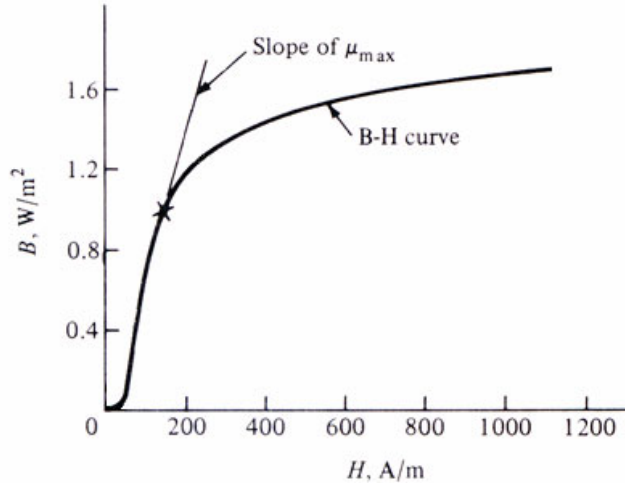


Figure 4.2: Typical B-H curve for magnetic material (Plonus, 1978)

The perturbation procedure for the TMS system consists of changing the input bias current to both actuators of an axis pair. For each bias current, the total currents from each of the opposing actuators are recorded comprising a current pair. Since the controller maintains the same target position, the force supported by the axis and the position of the target are the same for all of the recorded current pairs. These current pairs are then used to generate a vector of possible forces.

First of all, a vector of possible target positions is generated from $-g_o$ to $+g_o$, the physical bounds of the target within the actuators. The vector is broken down into discrete steps by a user chosen step size, Δx . Therefore, the target position vector is of the form shown in Equation 4.1.

$$x = \begin{bmatrix} -g_o \\ -g_o + \Delta x \\ -g_o + 2\Delta x \\ \vdots \\ -g_o + (m-1)\Delta x \\ -g_o + m\Delta x \end{bmatrix} = \begin{bmatrix} -g_o \\ -g_o + \Delta x \\ -g_o + 2\Delta x \\ \vdots \\ g_o - \Delta x \\ g_o \end{bmatrix} \quad (4.1)$$

where m is defined as

$$m = \frac{2g_o}{\Delta x} \quad (4.2)$$

For the flux based force equation used in the TMS scenario, the target position vector is substituted into the fringing factor equations (see Equations 2.10 and 2.11). along with the flux density measurements to produce a flux based force vector for each position listed in the vector in Equation 4.1. Once this substitution is complete for all of the flux density pairs (i.e. one perturbation condition), a matrix of possible forces is produced where each column represents a flux density pair from an associated perturbation. The flux based force matrix is of the form

$$F_b = \begin{bmatrix} F(-g_o; B_{10}, B_{20}) & \dots & F(-g_o; B_{1n}, B_{2n}) \\ F(-g_o + \Delta x; B_{10}, B_{20}) & \dots & F(-g_o + \Delta x; B_{1n}, B_{2n}) \\ \vdots & \ddots & \vdots \\ F(-g_o + m\Delta x; B_{10}, B_{20}) & \dots & F(-g_o + m\Delta x; B_{1n}, B_{2n}) \end{bmatrix} \quad (4.3)$$

Note that for the current based force equation, this target position vector is substituted into the fringing factor and force equations (see Equations 2.22 through 2.24) along with each current pair to produce a current based force vector. The current based force matrix is of the form

$$F_i = \begin{bmatrix} F(-g_o; I_{10}, I_{20}) & \dots & F(-g_o; I_{1n}, I_{2n}) \\ F(-g_o + \Delta x; I_{10}, I_{20}) & \dots & F(-g_o + \Delta x; I_{1n}, I_{2n}) \\ \vdots & \ddots & \vdots \\ F(-g_o + m\Delta x; I_{10}, I_{20}) & \dots & F(-g_o + m\Delta x; I_{1n}, I_{2n}) \end{bmatrix} \quad (4.4)$$

The force matrices have the same number of columns as perturbations and the same number of rows as the target position vector, x . Theoretically, the row in which the forces match exactly across all of the current or flux density pairs represents the actual

physically realizable target position and axis force. Because the target position vector is not a continuous function, but made up of discrete target positions, the actual force and target position are determined by finding the row with the lowest standard deviation. Thus, a standard deviation vector is produced from each force matrix as shown in Equation 4.5.

$$\Sigma = \begin{bmatrix} \sigma[F(-g_o; I_{10}, I_{20}), \dots, F(-g_o; I_{1n}, I_{2n})] \\ \sigma[F(-g_o + \Delta x; I_{10}, I_{20}), \dots, F(-g_o + \Delta x; I_{1n}, I_{2n})] \\ \vdots \\ \sigma[F(-g_o + m\Delta x; I_{10}, I_{20}), \dots, F(-g_o + m\Delta x; I_{1n}, I_{2n})] \end{bmatrix} \quad (4.5)$$

The row of the target position vector that corresponds to the row with the minimum standard deviation is the most likely actual target position. This target position found using the multipoint method is called the predicted target position. Air gaps needed for the fringing factor expressions are determined using the predicted target position as well as the proximity sensor output. If used alone, the multipoint method would use the average value of the forces on this row as the predicted force. However, for the TMS scenario, the multipoint method is utilized only as a calibration technique as described in the following section. Increasing the number of perturbations and increasing the number of steps used in the target position vector improves the accuracy of the results from the multipoint method. For the TMS calibration procedure, seven perturbations and five thousand steps between $\pm g_o$ have been determined as sufficient for accurate force and target position results.

4.3 Using The Multipoint Algorithm as a Calibration Procedure

The multipoint method is used as an online calibration for the TMS prototype. The position sensors output a relative position of the target, and the multipoint method outputs the absolute physical position of the target. Both of these target positions are used in subsequent force calculations. The predicted target position from the multipoint method is added to the position sensor measurements to give the absolute target position at any time. So, the flux based force equation including the predicted target position term

is shown in Equation 4.6 where the fringing factor equation are given in Equations 4.7 and 4.8.

$$F = \frac{A_g}{2\mu_o} (ff_1 B_1^2 - ff_2 B_2^2) \quad (4.6)$$

$$ff_1 = A_b e^{-\alpha_b \left(\frac{g_o - (x + x_{ptp})}{W} \right)} + K_b \quad (4.7)$$

$$ff_2 = A_b e^{-\alpha_b \left(\frac{g_o + (x + x_{ptp})}{W} \right)} + K_b \quad (4.8)$$

where g_o is the nominal gap between the actuator and target; x is the relative target position from the position sensors; x_{ptp} is the absolute target position from the multipoint method; and A_b , α_b , K_b , and W are constants from MFEA for the particular bearing geometry.

Including the predicted target position from the multipoint method in the current based force equation yields Equation 4.9 where the fringing factor equation are given in Equations 4.10 and 4.11.

$$F = \frac{\mu_o N^2 A_g}{2} \left(\frac{ff_1 I_1^2}{\left(\frac{L_i}{\mu_r} - 2(g_o - (x + x_{ptp})) \right)^2} - \frac{ff_2 I_2^2}{\left(\frac{L_i}{\mu_r} - 2(g_o + (x + x_{ptp})) \right)^2} \right) \quad (4.9)$$

$$ff_1 = \frac{1}{2} \left[A_i e^{-\alpha_i \left(\frac{g_{o1} - (x + x_{ptp})}{W_1} \right)} + K_i \right] \left[A_i e^{-\alpha_i \left(\frac{g_{o1} - (x + x_{ptp})}{W_2} \right)} + K_i \right] \quad (4.10)$$

$$+ \frac{1}{2} \left[A_i e^{-\alpha_i \left(\frac{g_{o2} - (x + x_{ptp})}{W_3} \right)} + K_i \right] \left[A_i e^{-\alpha_i \left(\frac{g_{o2} - (x + x_{ptp})}{W_4} \right)} + K_i \right]$$

$$ff_2 = \frac{1}{2} \left[A_i e^{-\alpha_i \left(\frac{g_{o1} + (x + x_{ptp})}{W_1} \right)} + K_i \right] \left[A_i e^{-\alpha_i \left(\frac{g_{o1} + (x + x_{ptp})}{W_2} \right)} + K_i \right] \quad (4.11)$$

$$+ \frac{1}{2} \left[A_i e^{-\alpha_i \left(\frac{g_{o2} + (x + x_{ptp})}{W_3} \right)} + K_i \right] \left[A_i e^{-\alpha_i \left(\frac{g_{o2} + (x + x_{ptp})}{W_4} \right)} + K_i \right]$$

where g_{o1} is the nominal gap for the outer legs of the actuator; g_{o2} is the nominal gap for the center leg of the actuator; x is the relative target position from the position probes; x_{ptp} is the absolute target position from the multipoint method; and A_i , α_i , K_i , W_1 , W_2 , W_3 , and W_4 are constants from MFEA for the particular bearing geometry. By determining physical target positions and associated air gaps, the multipoint method allows for accurate determination of forces.

4.4 Calibration Procedure for the TMS Demonstrator

The system calibration programs use the multipoint method to determine the predicted rotor positions for all the axes to be used in subsequent static and dynamic force calculations. Two LabVIEW Virtual Instrument (VI) programs are used to calibrate the system: “DC FLUX SAVE,” used in the setup procedure, and “AUTOCAL,” the main calibration program. Both system calibration programs are located in the “TMS Cal – 15 Axes – Autocal” folder. Bias currents of 0.9 amps to 1.3 amps in 0.1 amp increments, first increasing, then decreasing, are used in the “AUTOCAL” VI for a total of nine perturbations.

The “AUTOCAL” VI must be run seven times with a break between each test to allow the bearings to cool, resulting in seven predicted rotor positions for each axis. Seven predicted rotor positions are found for each axis because of the spread in results from test to test. For each axis, the value that deviates most from the average of these seven predicted rotor positions is discarded. The remaining six predicted rotor position are then averaged and used in subsequent static and dynamic force calculations. This has been determined to be the best procedure for finding the predicted rotor position because of the low standard deviation for each average predicted rotor position. The TMS calibration procedure takes a little over an hour, not including bearing cool down time between tests. Including a ten minute cool down time between tests increases the calibration time to about two and a half hours.

4.4.1 Setup Procedure

Several steps must be completed prior to running the “AUTOCAL” VI. With the circuit boards powered and the floating frame delevitated, the user must first press the “Run” arrow of the “DC FLUX SAVE.” This program records the flux density voltage outputs from the circuit boards when the flux in the actuators is zero. These voltages are subtracted from subsequent flux density measurements to find the actual flux density through each actuator.

Next, the correct parameter files must be loaded into the Revolve controllers before the floating frame is levitated. The parameter values files (PVFs) with a bias current of 0.9 amps must be loaded first. This is done using the MBScope “Parameter Loader” software supplied by Revolve. The user must click “Browse” in the “Parameter Loader” window to select the “Autocal PVF Files” folder. The computer can send and receive information from only one controller at a time, so the data switch is used to select the desired controller. There are four positions on the data switch: A corresponds to Controller 1(A), B corresponds to Controller 2(B), C corresponds to Controller 3(C), and D is unused. The user must then toggle the data switch selector to the “A” position selecting Controller 1(A), and open the “Controller 1(A) V20 Bias 0-9” file. The parameter files are sent to the controller by pressing the “Send File to Controller” button. This procedure is repeated for Controllers 2(B) and 3(C), using the “Controller 2(B) V20 Bias 0-9” and “Controller 3(C) V20 Bias 0-9 35 Off” parameter files, respectively. Note that the 35_ bearing, controller by Controller 3(C) is turned off due to axis instability. The data switch selector must be toggled to send the files to the correct controller. Turning on all three controllers levitates the floating frame of the TMS.

The system must now be allowed to reach a steady state in which all the axes are levitated and centered. The MBScope “Snapshots” software supplied by Revolve allows the user to view the positions of each axis for the controller selected by the data switch. The positions of the axes are plotted in real time by clicking on the “Channels” drop down menu and selecting “Positions.” To view the numerical values instead of the plots

of the positions, the user can click on the “View” drop down menu and select “Statistics.” When all of the positions of all three controllers are fluctuating within the hundredths of a micron (μm) range, the system has reached steady state. It takes about two minutes for the system to reach steady state. The calibration process may now begin.

4.4.2 Calibration Procedure

The system is calibrated by determining the rotor positions using the “AUTOCAL” VI. The user can enter the amount of time desired between tests by entering the desired value in the “Seconds Between Tests” control on the front panel. This is the amount of time the user is given to change the parameter files of all three controllers. The default value is 60 seconds. The “Calculating Test Number” indicator shows the user which perturbation is being processed by the program. Fluxes, currents, and positions are sampled at 1024 Hz and averaged over 1024 samples. Consequently, data is collected for one second immediately before the number in the “Calculating Test Number” indicator changes. Because the transient response takes a few seconds to decay when the bias current is changed, all of the parameter files should be loaded at least five seconds before the “Calculating Test Number” changes. Thus, a value of 60 in the “Seconds Between Tests” really gives the user 55, not 60, seconds to change the parameter files of all three controllers. A summary of the parameter files that must be loaded in the controllers for each test is shown in Table 4.1.

Table 4.1 shows the parameter files that must be loaded into the controllers for a given number appearing in the “Calculating Test Number” indicator. For example, immediately after the “Calculating Test Number” indicator changes from “1” to “2,” the user must begin loading “Controller 1(A) V20 1-1,” “Controller 2(B) V20 1-1,” and “Controller 3(C) V20 Bias 1-1 35 Off” into Controllers 1(A), 2(B), and 3(C), respectively. These files should be loaded at least five seconds before the “Calculating Test Number” indicator changes to “3.”

Table 4.1: Summary of PVF Controller Files Used in the “AUTOCAL” VI

| Number Value showing in “Calculating Test Number” indicator | Bias Current (A) | Controller 1(A) PVF | Controller 2(B) PVF | Controller 3(C) PVF |
|---|---|---------------------------------|---------------------------------|--|
| 0 | 0.9 | Controller 1(A) V20 Bias 0-9 | Controller 2(B) V20 Bias 0-9 | Controller 3(C) V20 Bias 0-9 35 Off |
| Press the “Run” arrow on the “AUTOCAL” VI | | | | |
| 1 | 1.0 | Controller 1(A) V20 Bias 1-0 | Controller 2(B) V20 Bias 1-0 | Controller 3(C) V20 Bias 1-0 35 Off |
| 2 | 1.1 | Controller 1(A) V20 Bias 1-1 | Controller 2(B) V20 Bias 1-1 | Controller 3(C) V20 Bias 1-1 35 Off |
| 3 | 1.2 | Controller 1(A) V20 Bias 1-2 | Controller 2(B) V20 Bias 1-2 | Controller 3(C) V20 Bias 1-2 35 Off |
| 4 | 1.3 | Controller 1(A) V20 Bias 1-3 | Controller 2(B) V20 Bias 1-3 | Controller 3(C) V20 Bias 1-3 35 Off |
| 5 | 1.2 | Controller 1(A) V20 Bias 1-2 | Controller 2(B) V20 Bias 1-2 | Controller 3(C) V20 Bias 1-2 35 Off |
| 6 | 1.1 | Controller 1(A) V20 Bias 1-1 | Controller 2(B) V20 Bias 1-1 | Controller 3(C) V20 Bias 1-1 35 Off |
| 7 | 1.0 | Controller 1(A) V20 Bias 1-0 | Controller 2(B) V20 Bias 1-0 | Controller 3(C) V20 Bias 1-0 35 Off |
| 8 | 0.9 | Controller 1(A) V20 Bias 0-9 | Controller 2(B) V20 Bias 0-9 | Controller 3(C) V20 Bias 0-9 35 Off |
| 9 | Wait for the “AUTOCAL” VI to finish running | | | |

After the last parameter file is loaded and the “Calculating Test Number” indicator reads “9”, the “AUTOCAL” VI calculates the predicted rotor positions and predicted forces for each of the axes using the multipoint method and saves these values to a file. The “AUTOCAL” VI has completed the calibration when the “Running” arrows return to a solid “Run” arrow.

The calibration procedure described above must be repeated six times for a total of seven calibrations. The same file of DC flux densities should be used for all the calibrations, so the “DC FLUX SAVE” VI should not be run again. The output filenames in the “AUTOCAL” VI must be incremented every time the calibration procedure is run.

For example, after the first run, “fluxdat1.dat” becomes “fluxdat2.dat,” “fluxrotposdat1.dat” becomes “fluxrotposdat2.dat,” etc. The default value is “...1.dat.”

Running the “AUTOCAL” VI seven times results in fourteen predicted rotor position vectors: seven for the current based method and seven for the flux based method. These vectors are used in both the static and dynamic force acquisition programs to calculate accurate forces.

Chapter 5

Thermal Testing

5.1 Introduction

Because the flux sensors used in the unit are temperature sensitive, and located in a position that is subject to heating from the AMB coils, thermal testing was performed on the units. This testing was initially conceived to provide a thermal correction factor to subsequent static and dynamic load testing. Because the thermal effects of bearing 37_ could not be isolated, it was impossible to apply thermal correction factors to all the bearings. Correction factors must be known for all the bearings because the total forces are a function of the forces supported by the individual bearings. For that reason, subsequent testing is not corrected for thermal effects. Even without this correction, however, the target accuracy of 99.5% was obtained. A more sophisticated thermal testing program could be developed to correct for thermal variation in the flux sensors, resulting in improved accuracy. Such a program would be recommended for a full-scale system.

Each actuator is equipped with thermistors for tracking electromagnet coil temperatures. The coil and the Hall effect probes for this demonstrator unit are not designed to withstand more than 180°C and 100°C, respectively. Because of these thermal limitations, tracking the temperature to which these components are exposed is essential in order to prevent damage to the hardware. Additionally, the Hall effect probes that are used to measure the flux in the air gaps are temperature sensitive. Because of this sensitivity, it is desirable to have temperature data to correct the output, if a temperature

correction correlation for the probes can be determined. It is noted that coils and Hall effect probes are available that have a wider range of thermal operations.

The FH-560 flux sensors used in this test rig are manufactured by F. W. Bell and, according to the specifications, have a maximum thermal sensitivity of 0.1% per degree Celsius. A minimum thermal sensitivity is not specified. If the thermal sensitivity is near the maximum value, it may be too high to ignore for the flux accuracy needed in the force calculations. However, to correct for thermal effects the actual, not the maximum, thermal sensitivity must be determined for each probe. If the actual thermal sensitivity is low enough, thermal effects may be ignored. The variation of flux measurements due to thermal effects must remain at less than 0.25% error to ensure less than 0.5% total full load error, because force varies as the square of flux density.

5.2 Procedure

Each electromagnet actuator on the test rig is equipped with both a Hall effect flux sensor for measuring flux density and a thermistor for measuring temperature. Each pair of actuators has a differential eddy current position sensor to measure the relative position of the target. For each test, the support bearings were energized to levitate the floating frame, and one thrust bearing was energized. The testing described below was then performed on the energized thrust bearing. This set-up ensured that changes in flux, current, and position were due solely to temperature changes and not to the bearings pulling against one another.

Current, flux, position, and temperature measurements for individual actuators were recorded as the actuators heated up from ambient (about 25°C) to about 75°C. Under load, the bearings naturally heat up over time due to resistance heating in the coils. Larger loads, and thus larger currents, cause the actuators to heat up more quickly, and also result in higher actuator temperatures. In addition to flux measurements, current and position measurements were taken for each bearing. If the trend in the flux measurements matched the trend in the current and position measurements, then the change in flux was most likely due to an actual change in flux and not a change in

measured flux due to temperature changes. However, if the trend in the flux measurement did not match the trend in the current and position measurements, the trend could be considered due to thermal effects.

The first objective of the thermal testing was to determine if the temperature dependency of the flux measurements could be ignored. The percent error full load for the flux measurements is calculated using Equation 5.1.

$$\% \text{ Error Full Load} = \left(\frac{B_{\max} - B_{\min}}{6 \text{kGauss}} \right) * 100\% \quad (5.1)$$

In Equation 5.1, B_{\max} and B_{\min} are the minimum and maximum magnetic flux density over the temperature range and 6 kGauss is the maximum expected magnetic flux output from the actuators.

As described above, if the flux error is greater than 0.25% error full load, then a relationship between flux and temperature must be determined to correct the temperature dependence of the flux measurements. This is accomplished by performing a quadratic least squares curve fit on the flux versus temperature data. An R-squared value is also calculated to determine how well the curve fit matches the data. Built-in functions on Microsoft Excel are used to perform the quadratic least squares curve fit and calculate the R-squared value. In general, an R-squared value of greater than or equal to 0.995 is considered a good fit of the data.

5.3 Thermal Testing Results and Conclusions

Bearings 32_–, 34_–, and 37_– were tested to determine the temperature dependency of the flux measurements. Flux, current and position are plotted versus temperature for both actuators of each bearing. The flux versus temperature plots for both actuators of bearing 32_– are shown in Figure 5.1. These results are typical of the data for both 32_– and 34_–.

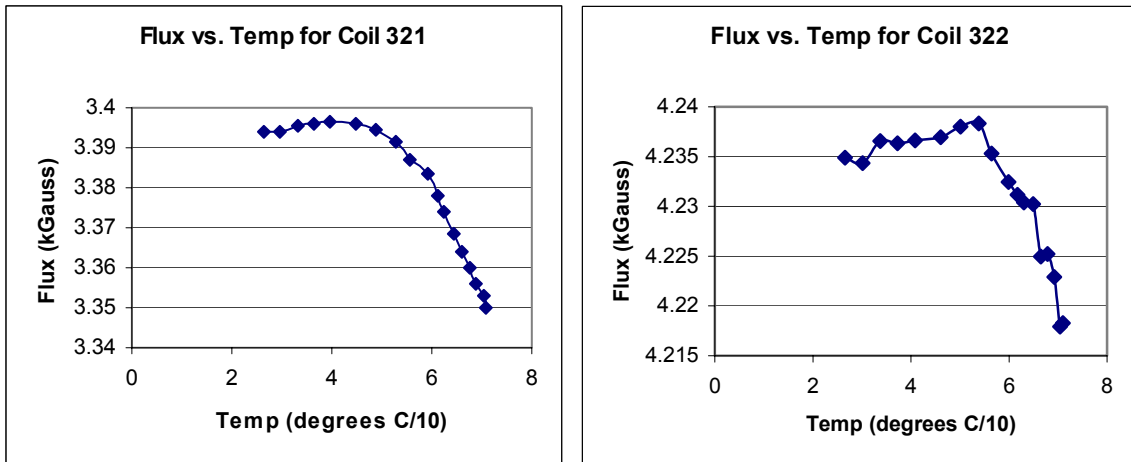


Figure 5.1: Flux Versus Temperature for Both Actuators of Bearing 32_

There is a definite trend in the flux versus temperature data for both actuators of bearing 32_. The flux increases slightly then decreases more dramatically as the temperature increases. This trend could be due to thermal effects because according to the specifications for the FH-560 probes, the probes have a negative thermal sensitivity. This means that the voltage output decreases as the temperature increases. It is still possible that the trend is simply due to actual changes in flux; for this reason it is necessary to compare the current versus temperature plots with Figure 5.1 to determine if the trend is due to the thermal sensitivity of the probes or actual changes in flux. Figure 5.2 shows the current versus temperature plots for both actuators of bearing 32_.

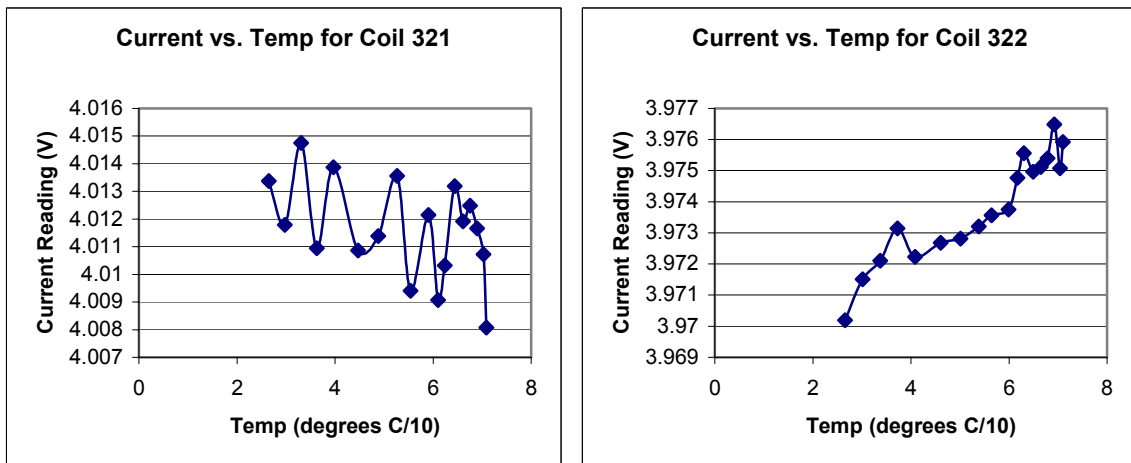


Figure 5.2: Current Versus Temperature Plots for Both Actuators of Bearing 32_

A slight decreasing trend can be seen in the current versus temperature plot for actuator 321; however, the opposite trend can be seen in the results for actuator 322. The slightly increasing trend seen in actuator 322 is probably due to I^2R heating of the coil with higher current. The slight decreasing trend in the current versus temperature plot for actuator 321 may be due to convective cooling due to the fact that this actuator is positioned toward the outside of the test rig where it is more susceptible to air drafts. Despite the fact that there are slight trends in the current data, these trends do not match the trends seen in the flux data shown in Figure 5.1, reiterating the hypothesis made earlier that the trend in the flux data is due to the thermal sensitivity of the probes rather than actual changes in flux. Because the changes in actual flux shown in the current versus temperature plots are too small to account for the changes in flux seen in Figure 5.1, the change in flux is most likely due to the thermal sensitivity of the flux probes rather than the changes in actual flux.

To further check this hypothesis, the position sensor output is also plotted versus temperature for both actuators of bearing 32_{_}. These plots can be seen below in Figure 5.3. Due to the fact that differential position sensors are used on each axis, the position versus temperature plots for actuators 321 and 322 are the same.

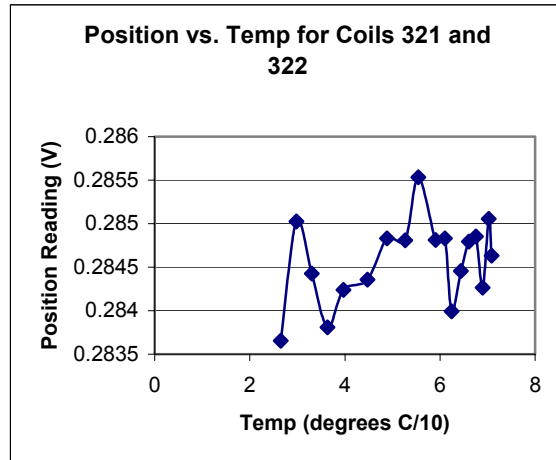


Figure 5.3: Position Versus Temperature Plots for Both Actuators of Bearing 32_{_}

It can be seen in Figure 5.3 that there is no real trend in the position data. The gain for the proximity sensors is 0.008in/V, so the changes in position seen in Figure 5.3 are small with no apparent trend. Because these plots and the current versus temperature plots seen in Figure 5.2 lead to the same conclusion, the trend in flux with increasing temperature for bearing 32_{_} is most likely due to the thermal sensitivity of the flux probes rather than any actual change in flux. Because the results for bearing 32_{_} are typical for bearing 34_{_} as well, this same conclusion can be made about the results from bearing 34_{_}.

The same trends in flux versus temperature are not seen in bearing 37_{_}, however; these results are shown below in Figure 5.4. The trend in flux is not the same for both actuators of bearing 37_{_}.

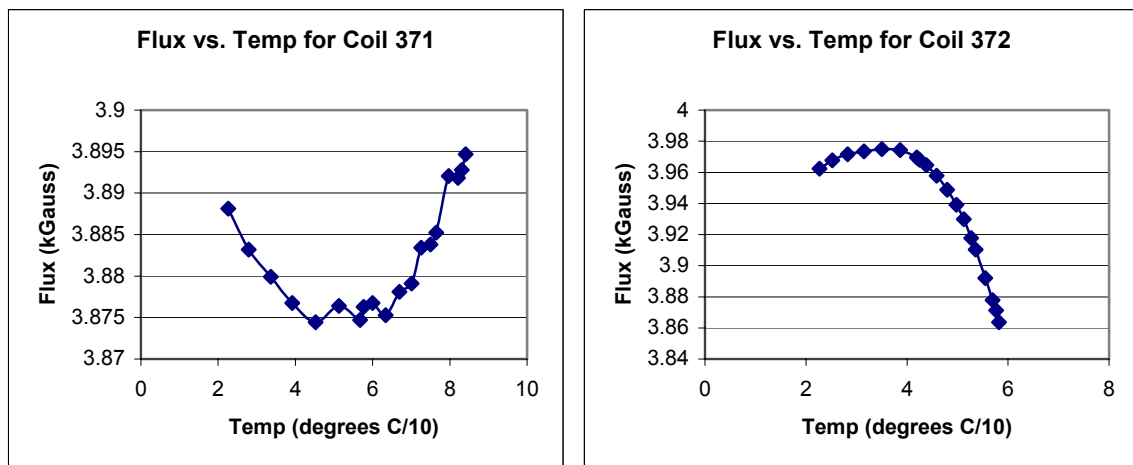


Figure 5.4: Flux Versus Temperature Plots for Both Actuators of Bearing 37_{_}

The flux through actuator 371 decreases then increases with increasing temperature, while the flux through actuator 372 increases slightly then decreases. Because the flux probes have a negative thermal sensitivity, the trend seen in actuator 371 is most likely due to actual changes in flux rather than the thermal sensitivity of the flux probes. The trend in flux seen in actuator 372 is very similar to the trend seen in both actuators of bearing 32_{_} and could be due to thermal effects. Again, it is necessary to investigate the current versus temperature data as well to check these hypotheses.

The current versus temperature plots for both actuators of bearing 37_{_} are shown in Figure 5.5. For actuator 371, the trend in current matches the trend in flux almost exactly. The current first decreases, then after about 55°C starts to increase.

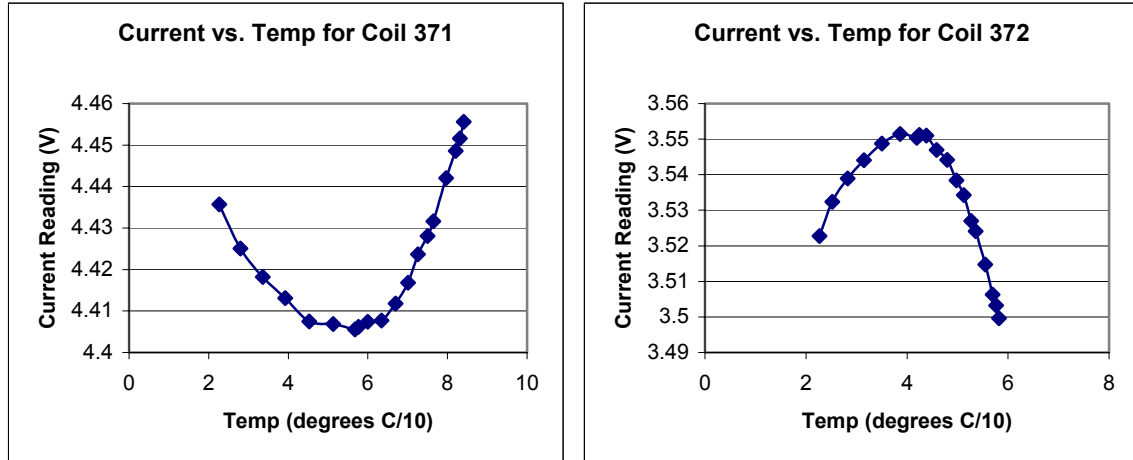


Figure 5.5: Current Versus Temperature Plots for Both Actuators of Bearing 37_{_}

Therefore, the trend in flux for actuator 371 is most likely due to actual changes in flux rather than the thermal sensitivity of the flux probe. The trend in current for actuator 372 is also similar to the trend seen in the flux data; however, the initial increase at lower temperature is more drastic in the current data than the flux data. This makes it difficult to determine the cause of the flux changes for actuator 372. The position data may allow a conclusion to be made.

The position data for both actuators of bearing 37_{_} is plotted in Figure 5.6. Again, due to the fact that differential sensors are used for each axis, the position data is the same for actuators 371 and 372. As temperature increases, the position data first increases, then begins decreasing at about 55°C. This follows the same trend as the flux and current data for actuator 372. This could mean that the trend in flux for actuator 372 is also a result of actual changes in flux rather than the thermal sensitivity of the flux probe.

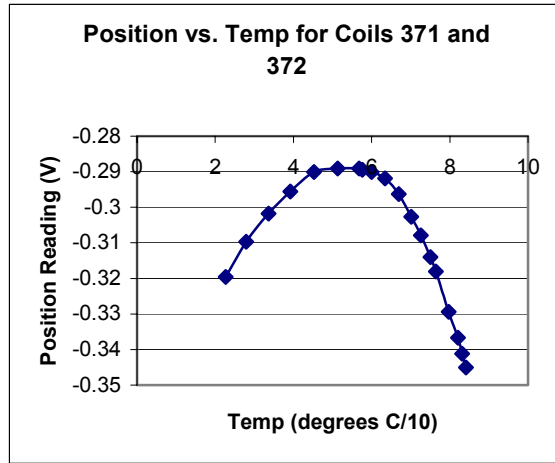


Figure 5.6: Position Versus Temperature for Both Actuators of Bearing 37_

It has been determined that a thermal sensitivity can be seen in the flux data at least for bearings 32_ and 34_. Therefore, the percent errors full load were calculated using Equation 5.1 for bearings 32_, 34_, and 37_ to determine whether the spread seen in the flux data over the temperature range was within an acceptable range. The results for the three bearings tested are summarized in Table 5.1.

Table 5.1: Percent Error Full Load Results from Individual Thrust Bearings

| Actuator | % Error Full Load |
|----------|-------------------|
| 321 | 0.770083333 |
| 322 | 0.34045 |
| 341 | 0.441866667 |
| 342 | 0.711416667 |
| 371 | 0.337733333 |
| 372 | 1.852816667 |

This table shows that none of the results fall within the 0.25% maximum error full load. This means that the temperature sensitivity of the flux probe cannot be ignored and must be corrected for if possible. It can also be seen that the errors for bearing 37_ are much higher than the other two bearings. This is probably due to the fact that the trends in the flux data for bearing 37_ are due to actual changes in flux rather than the thermal sensitivity of the flux probes. Because there are actual changes in flux as evidenced in

the current data, these changes are larger than changes that would result from the thermal sensitivity of the flux probes therefore leading to higher errors. Because the flux variations are too large to ignore, a least squares curve fit was applied to the flux versus temperature plots for both actuators of all three bearings. Figure 5.7 shows the results of the curve fit for both actuators of bearing 32_.

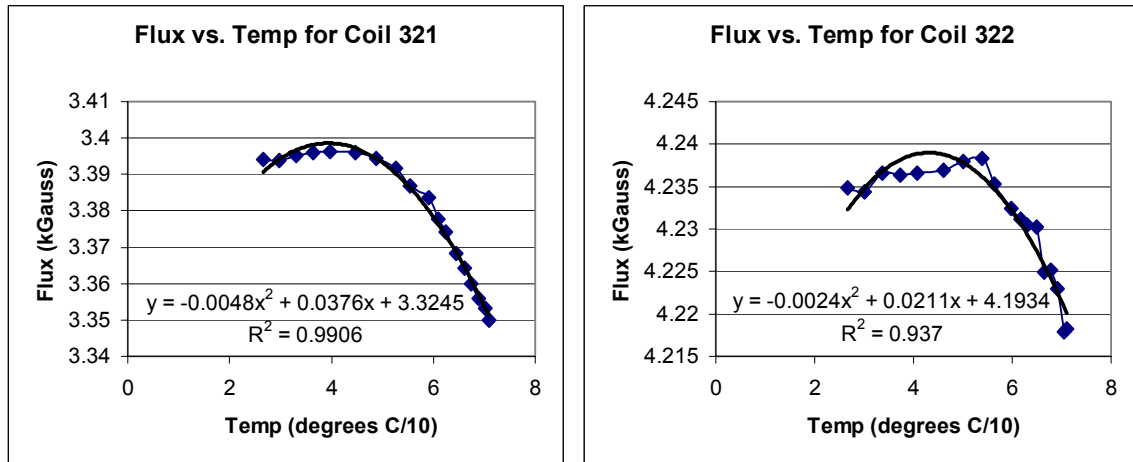


Figure 5.7: Least Squares Curve Fits for Both Actuators of Bearing 32_

The least squares curve fits are shown as a thick black line whereas the flux data itself is shown as a solid blue line with diamonds. The equations describing the curve fits as well as the R-squared values are also shown in each plot of Figure 5.7. Figure 5.7 is meant as an example to show how the least squares curve fit was performed using Excel for each actuator of bearings 32_, 34_, and 37_. Table 5.2 summarizes the curve fit results for both actuators of all three bearings.

Table 5.2: Summary of Quadratic Least Squares Fit on Flux and Temperature Data

| Actuator | $B = aT^2 + bT + C$; Flux in kG, Temp in C/10 | | | R-squared Value |
|----------|--|---------|--------|-----------------|
| | A | b | c | |
| 321 | -0.0048 | 0.0376 | 3.3245 | 0.991 |
| 322 | -0.0024 | 0.0211 | 4.1934 | 0.937 |
| 341 | -0.0038 | 0.0300 | 3.6860 | 0.979 |
| 342 | -0.0029 | 0.0229 | 4.0895 | 0.980 |
| 371 | 0.0018 | -0.0182 | 3.9204 | 0.970 |
| 372 | -0.0195 | 0.1333 | 3.7536 | 0.989 |

It is first noted that the coefficients for bearings 32_{_} and 34_{_}, while of similar sign and magnitude, have significant differences. This indicates that a separate thermal correction factor will need to be applied to each flux sensor. It is also noted that the coefficients for bearing 37_{_} are different in both sign and magnitude, further demonstrating the non-thermal effects present in this bearing. Additionally, all of the R-squared values are below 0.995 with the only R-squared value above 0.990 being that of actuator 321. This indicates that quadratic curve may not be sufficient to fit the data.

Efforts were made to eliminate the discrepancies between bearings 32_{_} and 34_{_} versus 37_{_}. However, the cause of the behavior seen in bearing 37_{_} is still unknown. For this reason a valid thermal correction factor for this bearing could not be derived. This inability to develop a correction factor for 37_{_} in the current testing, however, precludes the possibility of using individual correction factors for each actuator.

The thermal testing results prove that the temperature sensitivity of the flux probes cannot be ignored. The percent errors full load for all of the actuators tested were higher than the 0.25% error full load maximum set by the accuracy needed for the force calculations. The variation in quadratic least squares curve fit results, however, make it impossible to accurately determine a single relationship relating flux and temperature for all flux sensors. A separate thermal calibration curve should be developed for each Hall sensor. While this would be possible if the testing were conducted prior to system assembly, the inability to establish an individual correction factor for bearing 37_{_} in this demonstrator unit makes it impossible to apply individual correction factors for each bearing. The ability to develop this type of testing in a full scale TMS utilizing magnetic bearings will improve the accuracy of that unit over the results for the demonstrator. The TMS demonstrator still has the capacity to make temperature measurements at each actuator. This temperature data is useful in preventing hardware damage to the actuator coils and Hall effect flux probes.

Chapter 6

Static Force Testing

6.1 Introduction

After the calibration procedure was completed, four loading cases were performed to determine the static force measurement capability of the TMS prototype. The four static loading cases used to test the TMS were completed using a positive pull with the turnbuckle and six thrust bearings energized, a positive pull with the turnbuckle and four thrust bearings energized, a negative pull with the turnbuckle and six thrust bearings energized, and a negative pull with the turnbuckle and four thrust bearings energized. As described in the “Static Force Acquisition” section, an axial loading that results in pulling the floating frame in the positive z-direction is called a positive pull, and an axial loading resulting in pulling the floating frame in the negative z-direction is called a negative pull.

Due to time limitations, only three trials were performed for each of these cases; however, an indication of repeatability is achieved. For each trial, the turnbuckle is tightened from no load to full load in ten steps. The capacity of each bearing is 37.77lb, so with six thrust bearings energized, full load is 226.62lb, and with four thrust bearings energized, full load is 151.08lb. Thus, for the loading cases with six thrust bearings, each step from no load to full load is approximately 22.5lb, and for the load cases with four thrust bearings, each step from no load to full load is approximately 15lb.

6.2 Vertical Weight Results and Conclusions

As described in Section 3.3, every time a new trial is run, it is necessary to run the LabVIEW VI “DC THRUST SAVE” to calculate the unloaded forces on the test rig.

When the floating frame is unloaded, the only force applied to the bearings in the y-direction is the weight of the floating frame, so the sum of the forces for each bearing in the y-direction corresponds to the weight of the floating frame. Because the floating frame was not weighed after fabrication, an estimate of the weight of the floating frame was determined in order to compare it to the flux and current based weight calculations from the “DC THRUST SAVE” VI. The estimation of the floating frame weight is based on product specifications for some components and digital scale measurements for other components. The estimated floating frame weight is 63.66lb. The breakdown of the frame weight estimation is shown in Table 6.1.

Table 6.1: Estimation of the Weight of the Floating Frame

| Component | Component Weight (lb) | Number of Each Component | Total Component Weight (lb) |
|---------------------------------|-----------------------|--------------------------|-----------------------------|
| Thrust Bearing Target | 1.6535 | 7 | 11.5745 |
| Radial Bearing Target | 3.0820 | 4 | 12.3280 |
| Aluminum Framing and Connectors | 39.7571 | 1 | 39.7571 |
| TOTAL WEIGHT | | | 63.6596 |

This estimated frame weight was then compared to the sum of the forces in the y-direction for both the flux and current based force calculations from the “DC THRUST SAVE” VI. The percent error full load was determined using Equation 3.3.

$$\% \text{ Error Full Load} = \frac{(F_{\text{flux/current}} - F_{\text{est}})}{N * 37.77 \text{lb}} \quad (3.3)$$

where $F_{\text{flux/current}}$ is the sum of the forces in the y-direction for either the flux or current based force calculations, F_{est} is the estimated weight of the floating frame, N is equal to four because there are four bearings supporting the floating frame in the y-direction, and 37.77lb is the maximum capacity of each bearing. The weight of the floating frame is calculated by “DC THRUST SAVE” before the turnbuckle is tightened for all three trials

of every loading case. A summary table comparing the flux and current based weight calculations with the estimated weight is shown in Table 2.

Table 6.2: Comparison of Axially Unloaded Summed Flux and Current Based Y-Direction Forces with Estimated Floating Frame Weight

| Case | Test Number | Estimated Weight (lb) | Flux Based Result (lb) | Percent Error Full Load Flux | Current Based Result (lb) | Percent Error Full Load Current |
|---------------------------|-------------|-----------------------|------------------------|------------------------------|---------------------------|---------------------------------|
| Positive Pull, 6 Bearings | 1 | 63.66 | 62.89 | 0.51 | 69.78 | -4.05 |
| | 2 | | | | | |
| | 3 | | | | | |
| Positive Pull, 4 Bearings | 1 | 63.66 | 63.18 | 0.32 | 69.50 | -3.86 |
| | 2 | | | | | |
| | 3 | | | | | |
| Negative Pull, 6 Bearings | 1 | 63.66 | 63.45 | 0.14 | 69.60 | -3.93 |
| | 2 | | | | | |
| | 3 | | | | | |
| Negative Pull, 4 Bearings | 1 | 63.66 | 63.24 | 0.28 | 69.77 | -4.05 |
| | 2 | | | | | |
| | 3 | | | | | |

The flux based force calculation provides a more accurate floating frame weight than the current based force calculation. The current based approach resulted in errors below 4.2%, and all but one of the full load errors for the flux based method are below 0.50%, the target maximum error for the TMS.

6.3 Axial Loading Results and Conclusions

For each trial of the four loading cases, ten data points between no load and full load were taken. Because the capacity of each bearing is 37.77lb, full load is 226.62lb for cases in which six thrust bearings are energized and 151.08lb for cases in which four

thrust bearings are energized. The results for all four static loading cases are shown in Figures 6.1 through 6.8. Each plot shows percent error versus percent full load for all three trials of that loading case. Figure 6.1 presents the flux based results for a positive pull with six thrust bearings energized.

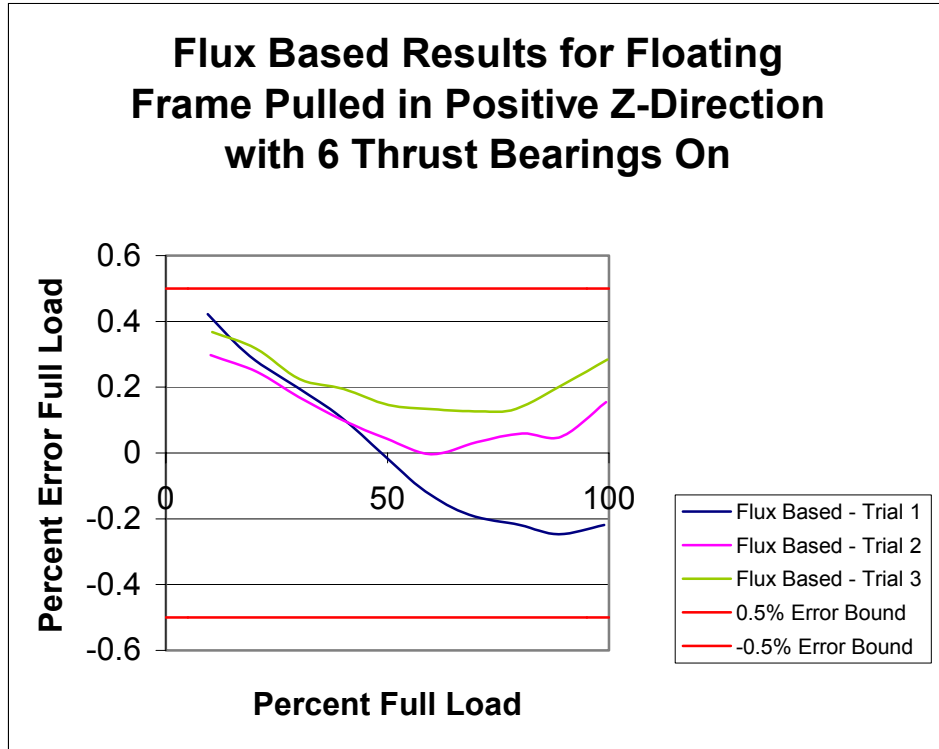


Figure 6.1: Flux Based Results for Positive Pull with Turnbuckle and Six Thrust Bearings Energized

The maximum error seen in the flux based results for this loading case is a little more than 4%. All of the errors for the flux based method are below the maximum target error of 0.50%. At lower loads, the errors are close to one another; however, at higher loads the spread in the error increases. Beyond this, there is really no apparent trend in the flux errors.

Current Based Results for Floating Frame Pulled in Positive Z-Direction with 6 Thrust Bearings On

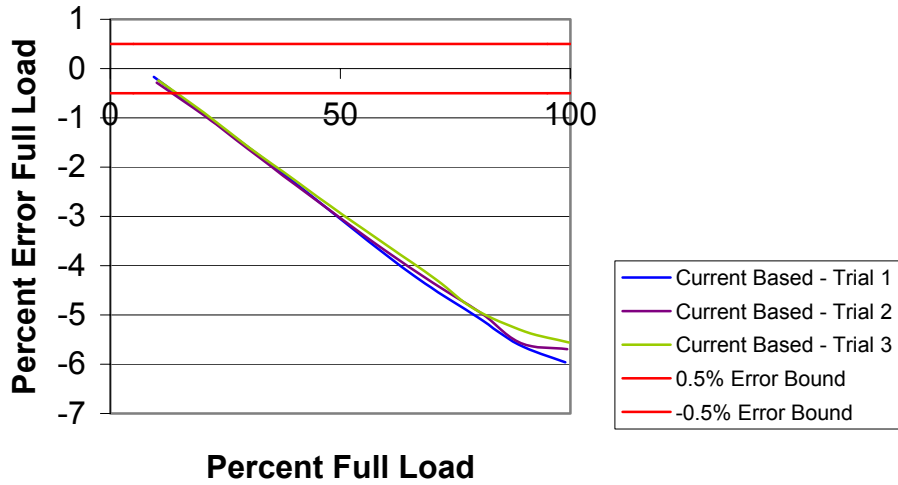


Figure 6.2: Current Based Results for Positive Pull with Turnbuckle and Six Thrust Bearings Energized

For the current based method results shown in Figure 6.2, however, the error appears to vary linearly with load. Because of the deterministic nature of the errors in the current based method, a calibration could be determined that would decrease these errors dramatically. However, one of the goals of this work is to present a calibration procedure that can be performed in a field situation and does not require applying known loads. Correcting for this deterministic error would, therefore, negate the benefits of this calibration procedure. The maximum error for this load case seen in the current based data is about 6%. Even though the errors for the current based method are higher than the flux based method, the multipoint calibration technique used to produce this data has still proved successful at predicting forces more accurately over a large range of loads. Calibration procedures that require applying known loads and, thus, are impractical in a field situation are producing errors of about 10% (Fittro et al., 1997; Aenis, 2000) using a current based force equation. This loading case produces errors of less than 6% over the full range of loading, making this force acquisition technique more accurate as well as more versatile. It should also be noted that all of the current based errors are negative,

which means that the current based force equation is consistently under predicting the force applied.

Figures 6.3 and 6.4 present the results for the second loading case with a positive pull and four thrust bearings energized for the flux and current based methods, respectively. A similar trend is shown in the results for this loading case as the loading case with a positive pull and six thrust bearings energized.

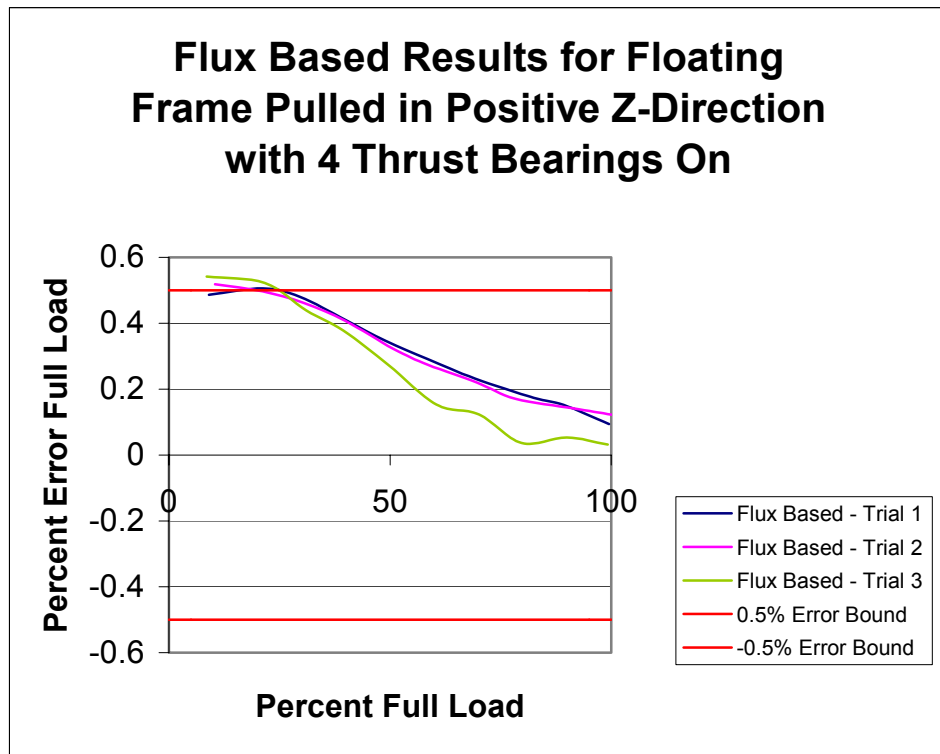


Figure 6.3: Flux Based Results for Positive Pull with Turnbuckle and Four Thrust Bearings Energized

The errors in the flux based results for this loading case are slightly higher with four data points lying above the maximum target error of 0.50%. Even so, the largest error seen for this loading case is 0.54%, which is only slightly above the maximum target error. It is evident that the fewer number of bearings running does affect the accuracy of results, but only slightly. With a positive pull and four thrust bearings energized, all of the flux errors are positive, which means that the flux based force equation is consistently over predicting the force applied. This is just the opposite trend as the current based results.

Current Based Results for Floating Frame Pulled in Positive Z-Direction with 4 Thrust Bearings On

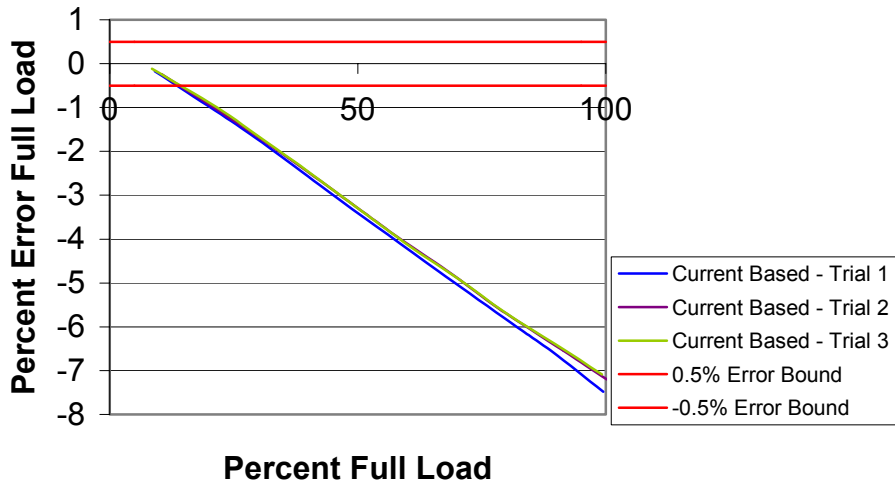


Figure 6.4: Current Based Results for Positive Pull with Turnbuckle and Four Thrust Bearings Energized

The same linear increase with load in the current based errors is seen in this loading case as the previous with a slightly higher maximum error. In this loading case with only four thrust bearings energized, the maximum error is close to 7.5%. Again, the accuracy of the force predictions using the current based force equations is slightly affected by the number of thrust bearings that are energized. All of the current based errors are once again negative, meaning that the current based force equation is consistently under predicting the applied forces.

The flux based results for the third loading case with a negative pull and six thrust bearings energized are shown in Figure 6.5. With six thrust bearings energized, the errors in the flux based method are once again all below the maximum target error of 0.50%.

Flux Based Results for Floating Frame Pulled in Negative Z-Direction with 6 Thrust Bearings On

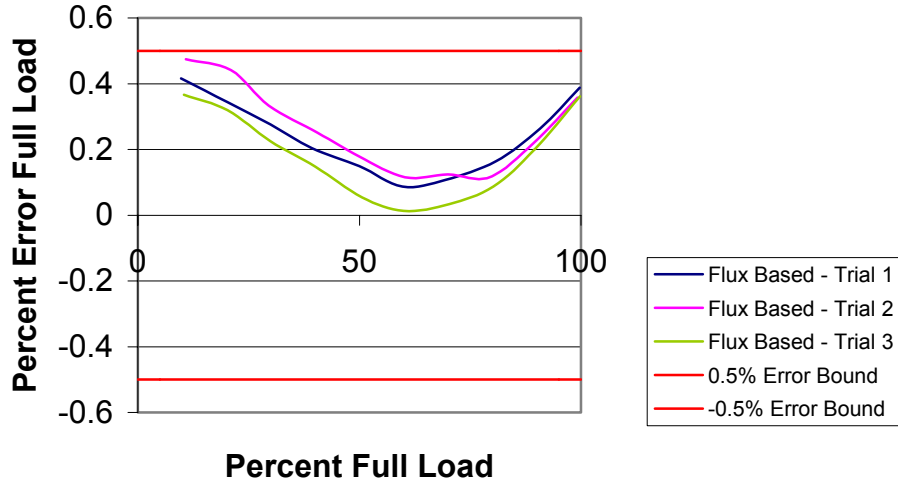


Figure 6.5: Flux Based Static Results for Negative Pull with Turnbuckle and Six Thrust Bearings Energized

For this loading case, however, there appears to be more of a trend in the flux based errors. The errors are higher at lower loads, then decrease to a minimum at about 50% full load, and increase again close to full load. This could be explained in the development of the fringing factor equation which is a curve fit formed from the average of many curve fits over a large range of loads. This would lead to lower errors at medium loadings and higher errors at either extreme.

Current Based Results for Floating Frame Pulled in Negative Z-Direction with 6 Thrust Bearings On

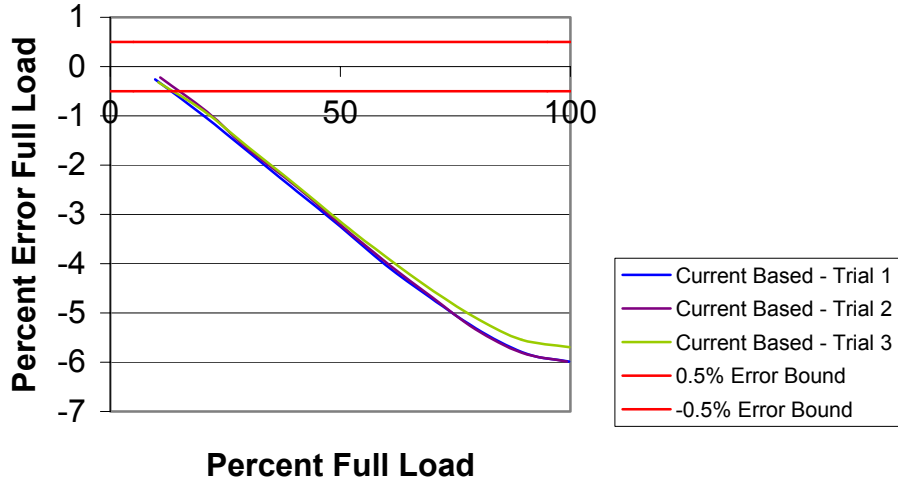


Figure 6.6: Current Based Static Results for Negative Pull with Turnbuckle and Six Thrust Bearings Energized

The current based method results shown in Figure 6.6 show the same linearly increasing trend in error with respect to load. Once again, with six thrust bearings energized, the maximum error is less than 6%. The error tends to start leveling off at loads close to full load. This is most likely due to saturation effects. As the actuators approach saturation, more current is needed to produce only small changes in flux. Because the current based method is consistently under predicting the applied force, these larger currents that result from saturation lead to smaller errors.

Figure 6.7 shows the flux based results for the fourth and final loading case with negative pull and four thrust bearings energized. There is no apparent trend in the flux based data shown in Figure 6.7.

Flux Based Results for Floating Frame Pulled in Negative Z-Direction with 4 Thrust Bearings On

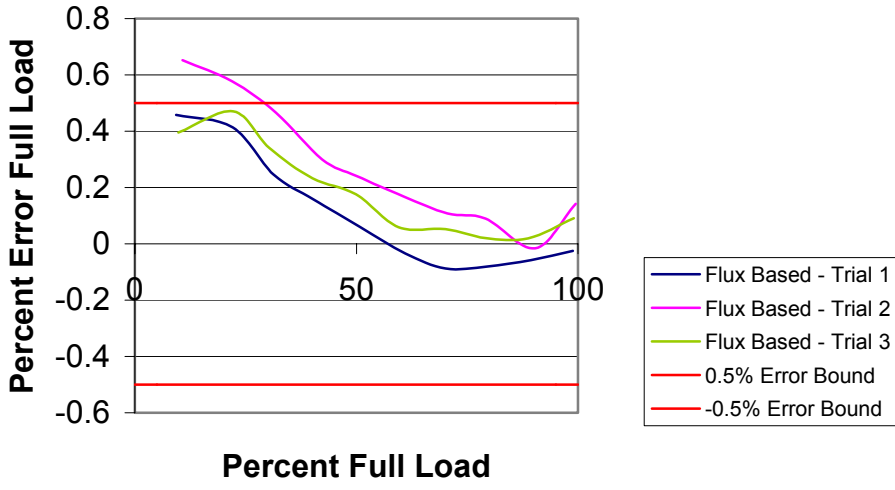


Figure 6.7: Flux Based Static Results for Negative Pull with Turnbuckle and Four Thrust Bearings Energized

For this loading case with a negative pull and four thrust bearings energized, only two data points lie outside the maximum target error, with the largest error being 0.66%. This is a larger maximum error than the loading case with a positive pull and four thrust bearings energized, however, the number of data points that lie outside the maximum target error is fewer. Also, as seen in Figure 6.7, only one of the tests resulted in errors outside the maximum target area. This means that an error could have occurred during testing which led to the higher errors for the one test.

Current Based Results for Floating Frame Pulled in Negative Z-Direction with 4 Thrust Bearings On

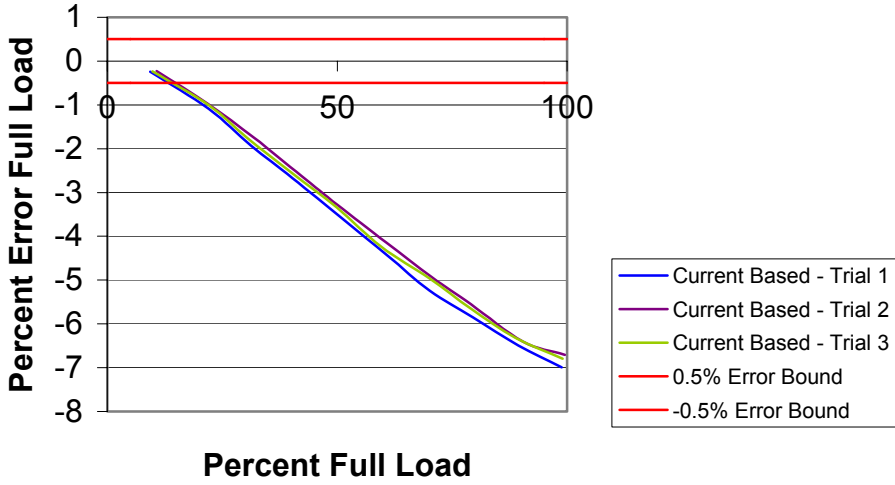


Figure 6.8: Current Based Static Results for Negative Pull with Turnbuckle and Four Thrust Bearings Energized

The results from the current based method shown in Figure 6.8 once again show a linearly increasing trend in error with load for the final loading case. The maximum error for this loading case is about 6%. This shows once more that the number of thrust bearings energized has only a small effect on the resulting errors.

Thus far, the load cell measurements have been assumed to be free of error, which is not true of any measurement. The specifications included with the MLP-300 load cell state that the accuracy of the load cell measurements is better than 99.9% full load. This means that the load cell could have errors as large as 0.3 lb (0.1% of full load) because the full load of the load cell is 300 lb. When this is substituted into Equation 6.1 (a variation of Equation 3.3), this corresponds to about a 0.2% error.

$$\% \text{ Error Full Load} = \frac{\Delta F}{N * 37.77 \text{ lb}} \quad (6.1)$$

Because the largest error seen in the flux based results is 0.66%, it is possible that the flux based method did in fact measure forces within 0.50% error full load. This is due to the fact that if 0.2% error bars are placed on the largest flux based error of 0.66%, the bottom bar falls within the maximum target error of 0.50%.

To show the relationship between the flux based and current based results, a plot of calculated axial load versus load cell measurement was constructed. Figure 6.9 shows the results from the first trial of the positive pull, six thrust bearings energized loading case. This plot is typical of all trials of all loading cases and is designed to show the relative errors between the flux and current based methods.

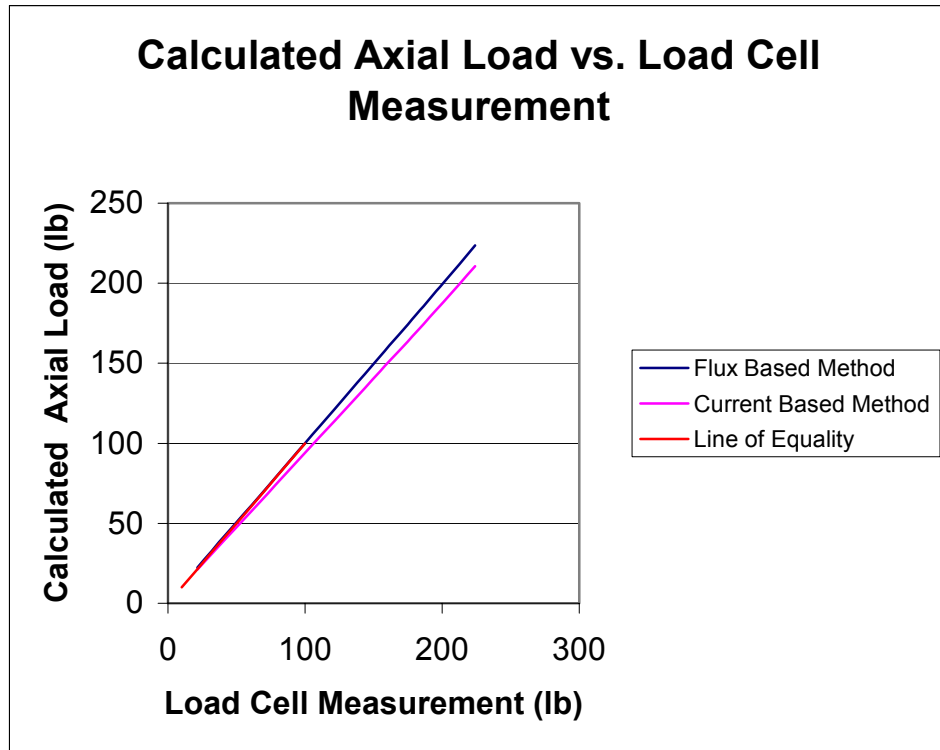


Figure 6.9: Typical Plot of Calculated Axial Load Versus Load Cell Measurement

In Figure 6.9, the “line of equality” represents the points at which the calculated load is equal to the load cell measurements for axial loads. Because the errors in the flux based method are so small, the flux based method results are hardly distinguishable from the line of equality in this chart. This plot, typical for all loading cases, shows that the

flux based method calculates forces more accurately than the current based method over the full range of loads.

The results from static testing show that the flux based method, with maximum errors of about 0.66% full load, calculates more accurate forces than the current based method, with maximum errors of about 7.5% full load. This can be compared to errors of about 1% as seen in previous work involving flux based force equations and to errors of about 10% as seen in previous work involving current based force equations (Aenis, 2000). Furthermore, if the accuracy of the load cell is considered, it is possible that all of the flux based errors fall within the maximum target error of 0.50%. There is no trend in the flux based errors with respect to percent full load that apply to all four load cases. For some cases the error decreases with load; for others, it decreases then increases. The current based errors, however, increase linearly with load.

Thus the techniques developed here have improved the state of the art in both flux and current based force measurement. This force measurement technique also has the added advantage that, when the fringing expressions are known from MFEA, the calibration does not involve applying known loads to calculate accurate forces, allowing this technique to be used in a field situation. The calibration for the TMS demonstrator is a process that can be completely automated and results in smaller errors in the force calculations than other methods.

The static results also prove that the number of thrust bearings energized has only a small effect on the accuracy of the force measurements. This means that a large range of thrusts can be measured on the same test stand simply by energizing different numbers of thrust bearings. This increases the versatility of the TMS beyond existing technologies allowing one test stand utilizing magnetic bearings to replace several test stands utilizing strain gauges with lower ranges of thrust capability.

Chapter 7

Dynamic Force Testing

7.1 Introduction

Dynamic testing was also performed on the rocket TMS. According to results from previous TMS tests at NASA, the maximum frequency component expected for a rocket TMS is about 30Hz. In order demonstrate the capability of dynamic force acquisition beyond this expected maximum frequency, the magnetically levitated rocket TMS prototype was tested up to 50Hz. Recall that the floating frame is not equipped with accelerometers; therefore, it is not possible to correct for the amplitude and phase shifts associated with the inertia of the floating frame.

The magnetostrictive force actuator was used to input various frequencies into the TMS. Force data was recorded for input sine waves of 5, 10, 20, 30, and 50Hz with zero to peak amplitude of half a volt resulting in peak load cell forces from about 42lb at 5Hz to about 55lb at 50Hz. The dynamic acquisition VI “FORCE MEASURE” was used to record the load cell measurement and the flux and current based force resultants. The program was set up with a sampling rate of 1000Hz acquiring 300 samples per channel. Consequently, forces are calculated over a time period of three tenths of a second.

An advantage of a magnetically levitated rocket TMS over current strain gauge designs is that the dynamics, including the location of system resonant frequencies, of the TMS can be controlled by changing the gain parameters of the magnetic bearings. To prove this capability with the TMS demonstrator, a swept sine wave from 5 to 50Hz, in fifteen steps, with a zero to peak magnitude of a half a volt was input into both the

original system and the stiffer system. The stiffer system was achieved by doubling the proportional gain of the magnetic bearings. For the swept sine wave input, the “FORCE MEASURE” VI was set up with a sampling rate of 500Hz acquiring 7500 samples per channel. Thus forces are calculated over a time period of fifteen seconds.

7.2 Dynamic Results and Conclusions for Original System

In Figure 7.1, the forces for the flux and current based methods as well as the load cell measurements are plotted versus time for an input frequency of 5Hz.

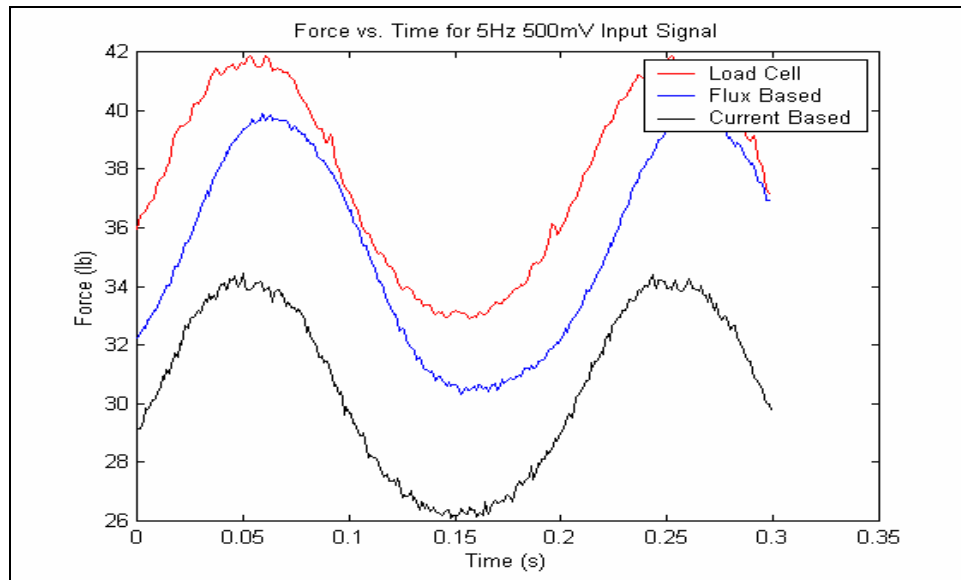


Figure 7.1: Dynamic Results for Input Frequency of 5Hz for Original System

The phase and AC component of the current based resultant are almost exactly the same as the load cell measurement; however, the flux based resultant is more accurate at calculating the DC component of the input force. This is unexpected because the flux based method should predict both the AC and DC components of forces more accurately than the current based method due to the fact that the flux is measured directly rather than inferred from coil currents and target positions. Even though the TMS demonstrator is not equipped with accelerometers to correct for inertial effects of the floating frame, at low frequencies where the system dynamics are minimal, a good correlation between the input force as measured by the load cell and the reaction force as measured by the flux

and current based force calculations is expected. Nevertheless, at an input frequency of 5Hz, all three methods of force measurement are fairly close in both phase and amplitude.

Figure 7.2 shows the dynamic results for an input frequency of 10Hz. At this input frequency, the current based method again predicts both the AC component and phase of the load cell measurement more accurately; however, the flux based method predicts the DC component more accurately.

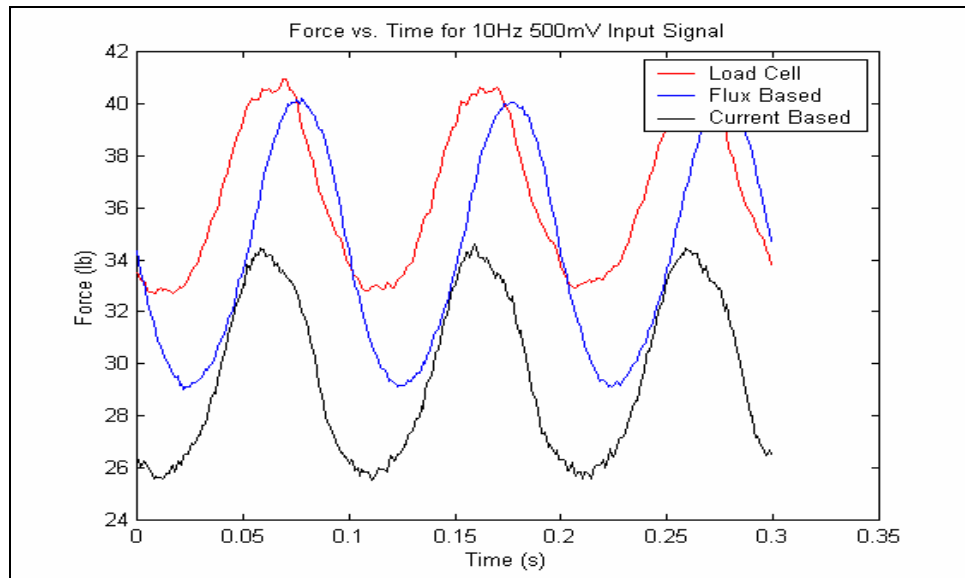


Figure 7.2: Dynamic Results for Input Frequency of 10Hz for Original System

As in the previous case with an input frequency of 5Hz, the peak to peak amplitude of the load cell and current based measurements is about 8lb, whereas the peak to peak amplitude of the flux based measurement is about 10lb. This agreement with the 5Hz input frequency results shows that the effects of system dynamics are still quite minimal at 10Hz. In other words, the flux and current based resultants at input frequencies of 5Hz and 10Hz that have not been corrected for the inertia of the floating frame should be close in both amplitude and phase to the actual reaction forces at the bearings.

The dynamic results for an input frequency of 20Hz are shown in Figure 7.3. At this input frequency, it is the flux based method rather than the current based method that calculates the AC component of the load cell more accurately.

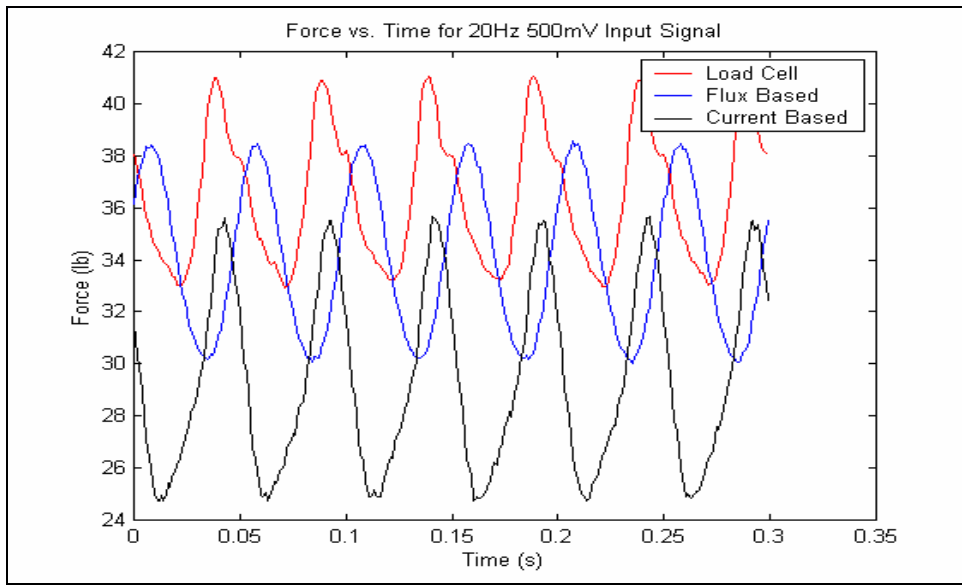


Figure 7.3: Dynamic Results for Input Frequency of 20Hz for Original System

So, for an input frequency of 20Hz, the flux based method predicts both the AC and DC components of the input force more accurately than the current based method. The peak to peak amplitude of the load cell measurement is about 8lb which is close to 7lb, the peak to peak amplitude of the flux based method. It should be noted that the peak to peak amplitude of the current based method is 10lb for an input frequency of 20Hz, which is quite a large increase from the 8lb peak to peak amplitude from the 10Hz case. The main frequency component of all three force measurements is 20Hz; however, there is a 60Hz component superimposed on the load cell measurement. This is probably not due to noise because it does not appear in any of the previous results; however, it should be noted.

Figure 7.4 shows the dynamic results for an input frequency of 30Hz. Once again, the flux based method predicts both the AC and DC components of the load cell measurement more accurately than the current based method. Both the load cell measurement and flux based resultant have a peak to peak amplitude of about 6lb. The current based AC amplitude is very high which is probably due to hysteresis and eddy current effects. At the input frequency increases, the currents in the coils must also

change more quickly to keep the floating frame levitated. These quickly changing currents lead to residual currents that must be overcome by the input current from the controller. This means that a large current is needed for only a small change in flux because some of the current is being used to overcome the residual currents and hysteresis effects. This would lead to over predictions in the forces calculated by the current based method. The flux based method would be unaffected by hysteresis and eddy current effects because the flux is being measured directly, not inferred from current and target position data.

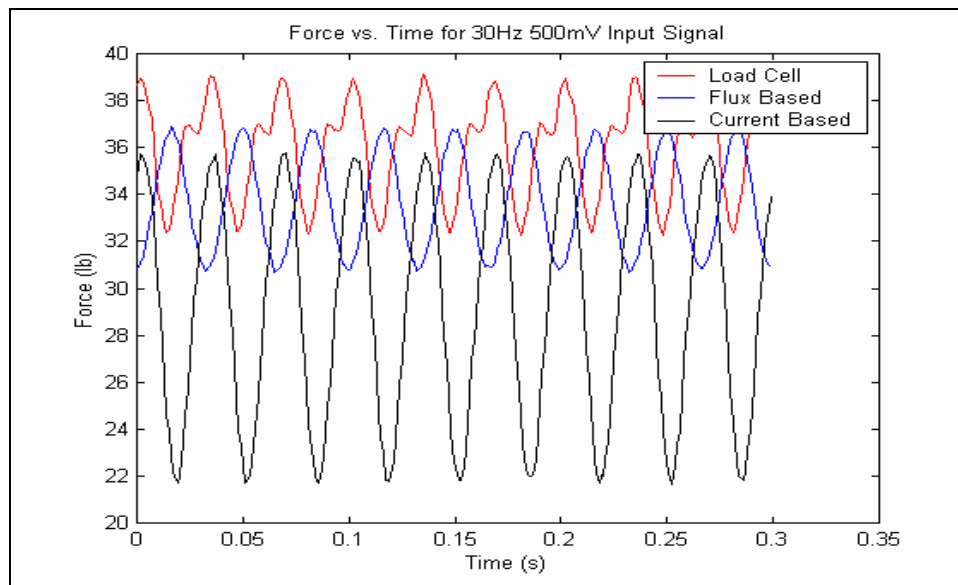


Figure 7.4: Dynamic Results for Input Frequency of 30Hz for Original System

The 60Hz frequency component in the load cell measurement is a bit stronger at an input frequency of 30Hz than an input frequency of 20Hz. This component is probably due to harmonics within the load cell instead of noise because it is only seen when the frame is forced at 20Hz and 30Hz. When the frame is forced at 20Hz, the second harmonic is 60Hz; whereas when the frame is forced at 30Hz, the first harmonic is 60Hz. This explains the fact that the 60Hz component is stronger when the frame is forced at 30Hz than when the frame is forced at 20Hz because harmonics drop off in amplitude with increasing frequencies. There are no 60Hz components in either the flux or current based force resultants.

The final input frequency to the TMS demonstrator was 50Hz. These results are shown in Figure 7.5. At this frequency, the load cell measurement data shows input forces that are beyond the capability of the magnetostrictive force actuator. This probably means that there is a system resonance close to 50Hz. The flux based resultant is only 5lb peak to peak which shows that the dynamics of the system are beginning to become significant. This means that the flux and current based resultants must include the inertial component of the floating frame to give accurate force and phase information. The current based method is also predicting forces that are incapable of being generated by the force actuator. This is probably due to the hysteresis and eddy current effects discussed previously.

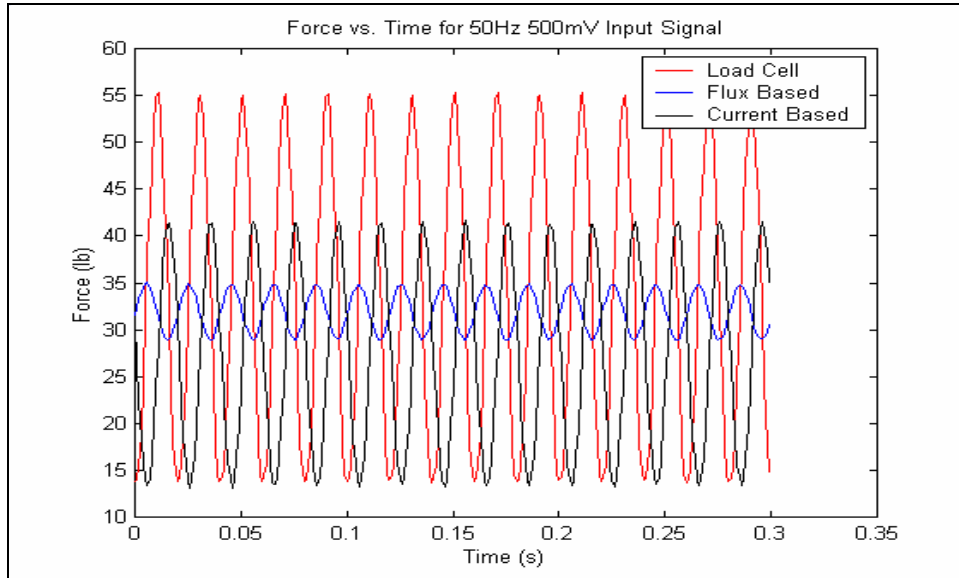


Figure 7.5: Dynamic Results for Input Frequency of 50Hz for Original System

From the dynamic results of the original system as a whole, several observations can be made. As the frequency is increased, both the magnitude and phase of the flux and current based force calculations deviate more. The larger deviations in magnitude of the flux based method at higher frequencies could be due to the fact that the effects of the system dynamics are stronger at higher frequencies. Therefore, the lower the input frequency, the better the results if they are not corrected for system dynamics. At higher input frequencies, the current based resultant increases in magnitude. This is probably

due to hysteresis and eddy current effects and cannot be corrected for. It should also be noted, that the load cell measurements are also much larger than the capability of the force actuator at 50Hz. This could be evidence of a system resonant frequency close to 50Hz. To check this hypothesis and prove that varying the gain parameters of the magnetic bearings can change the dynamics of the system, a swept sine wave input from 5Hz to 50Hz was input into the floating frame. The “FORCE MEASURE” VI was set up with a sampling rate of 500Hz acquiring 7500 samples per channel. Figure 7.6 shows the time response for flux and current based force calculations as well as the load cell measurement for the original system. In this plot, the frequency starts at 5Hz and increases 3Hz every second until it finally reaches 50Hz at 15 seconds. Thus, every second on the x-axis represents a 3Hz increase in frequency.

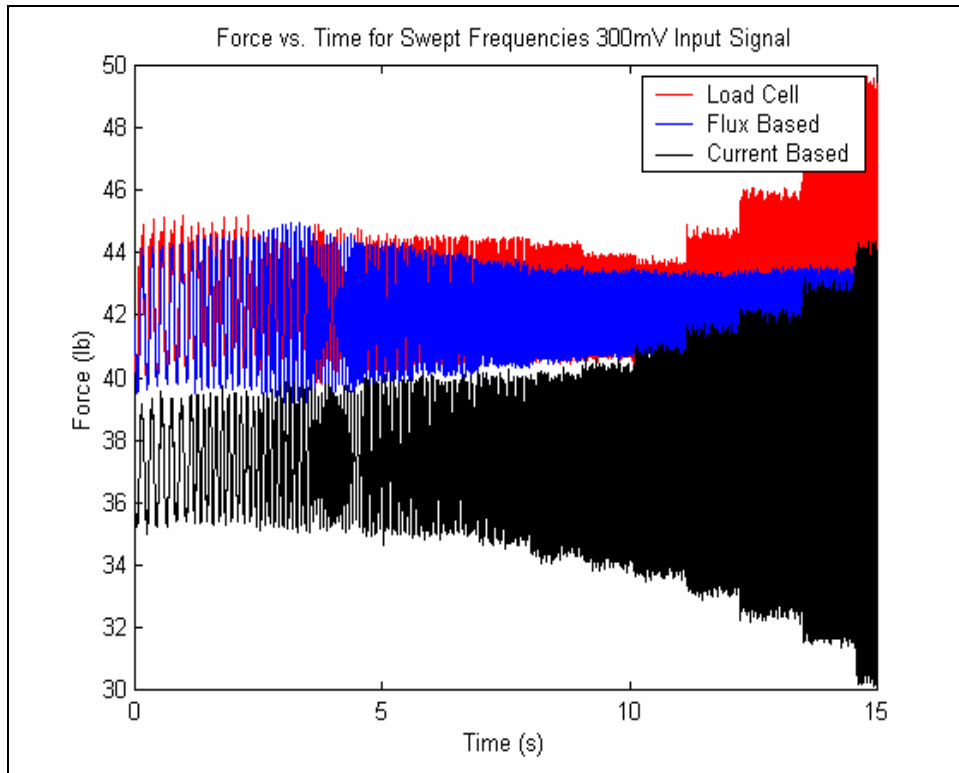


Figure 7.6: Time Response with Swept Sine Input for Original System

The measurement from the load cell shows a decreasing trend until about 11 seconds, or about 35Hz, followed by an increasing trend beyond the minimum at 11 seconds. This is evidence that the system is approaching a resonance at about 35Hz.

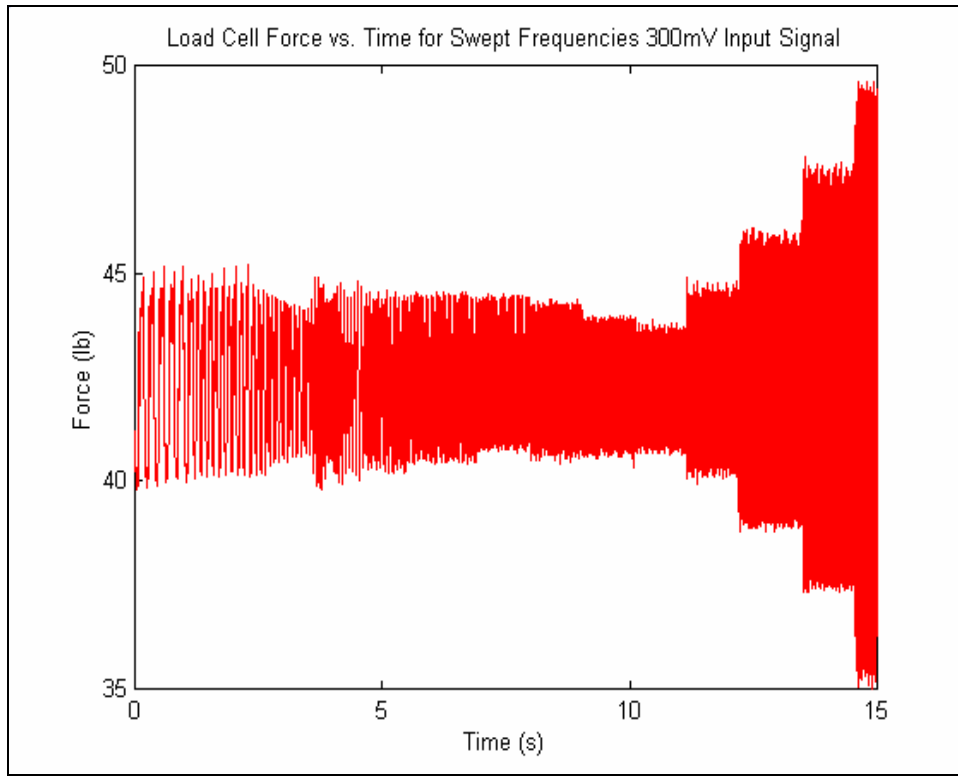


Figure 7.7: Time Response for Load Cell with Swept Sine Input for Original System

The trend can be seen more clearly in Figure 7.7 where the load cell data is plotted by itself. As the system approaches the resonance, the structure becomes very pliable leading to a smaller input force needed to move the frame a given distance. Then, after the system passes through the resonant frequency, it appears as though the floating frame is moving 180° out of phase with the input from the magnetostrictive force actuator causing the response to increase as the frequency increases. In order to completely determine whether or not the system is going through a resonance at about 35Hz, a plot of phase versus frequency is needed. This could be accomplished by determining the transfer function between force and position and plotting the phase for this transfer function versus frequency. A phase shift of 180° would designate a system resonance. Unfortunately, time restrictions did not allow this to be investigated.

The time response for the flux based measurement does not follow the same increasing trend as the load cell measurements. Instead, the time response for the flux based method continues to decrease as the frequency increases. This is due to the fact

that the inertia effects are not accounted for because the TMS demonstrator is not equipped with accelerometers. If the inertia term, being the product of the mass and acceleration of the floating frame, were added to the flux data, the same trend should be seen in both the load cell measurement and the flux based method results.

The time response of the current based measurement seems to follow the same trend as the load cell measurement without the initial decrease in response. This is probably due to hysteresis and eddy current effects rather than a system resonance because the initial decrease in response is not seen as in the current based results. Again, as the input frequency to the floating frame increases, the currents must switch directions more rapidly to keep the frame levitated, causing the build up of eddy currents. Every time the current changes direction, enough current must be injected into the actuator to both overcome the eddy current and hysteresis effects as well as produce enough force to maintain the centered target position. So, a large change in current results in a small change in magnetic flux. As discussed previously, this does not affect the flux based method because the magnetic flux density is being measured directly, not inferred from current and position data. This leads to the conclusion that the accuracy of the current based method in its existing incarnation is limited at higher frequencies.

7.3 Dynamic Results and Conclusions for Stiffer System

In order to further check the hypothesis of a system resonant frequency at 35Hz and to show that the magnetic bearing gain parameters can be used to change the system dynamics, the same tests as above were performed after doubling the proportional gain of the thrust bearings. The proportional gain corresponds to the stiffness of the magnetic bearings, so increasing it should increase the resonant frequency of the system. Table 7.1 summarizes the proportional gains used in the original and stiffer systems for each of the thrust bearings.

Table 7.1: Summary of Proportional Gains Used for Original and Stiffer Systems

| Thrust Bearing Number | Proportional Gain Used in Original System | Proportional Gain Used in Stiffer System |
|-----------------------|---|--|
| 31 | 35 | 70 |
| 32 | 35 | 70 |
| 33 | 35 | 70 |
| 34 | 35 | 70 |
| 35 | 55 | 110 |
| 36 | 55 | 110 |
| 37 | 45 | 90 |

The load cell, flux based, and current base measurements were again sampled at 1000Hz acquiring 300 samples to determine what affect doubling the proportional gain had on the system dynamics. Input frequencies of 5, 10, 20, 30, and 50Hz were input into the stiffer system using the magnetostrictive force actuator. The time responses for the stiffer system at an input frequency of 5Hz are shown in Figure 7.8.

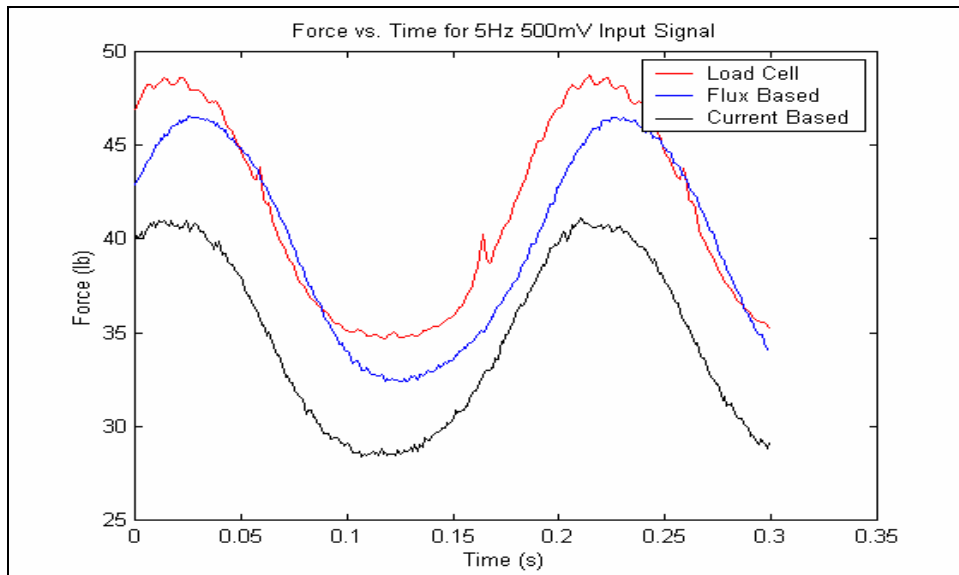


Figure 7.8: Dynamic Results for Input Frequency of 5Hz for Stiffer System

For the stiffer system at an input frequency of 5Hz, the forces being generated are a bit larger, but the results are still similar. Both the flux and current based methods accurately predict the AC component of the load cell measurement; however, the flux based method still predicts the DC component more accurately than the current based

method while the current based method still predicts the phase more accurately than the flux based method. Overall, the amplitudes and phases for all three measurements are close at an input frequency of 5Hz.

The dynamic results for an input frequency of 10Hz to the stiffer system are shown in Figure 7.9. At this input frequency, the current based method is predicting the AC component and phase of the load cell measurement more accurately than the flux based method. This is similar to the results seen in the original system.

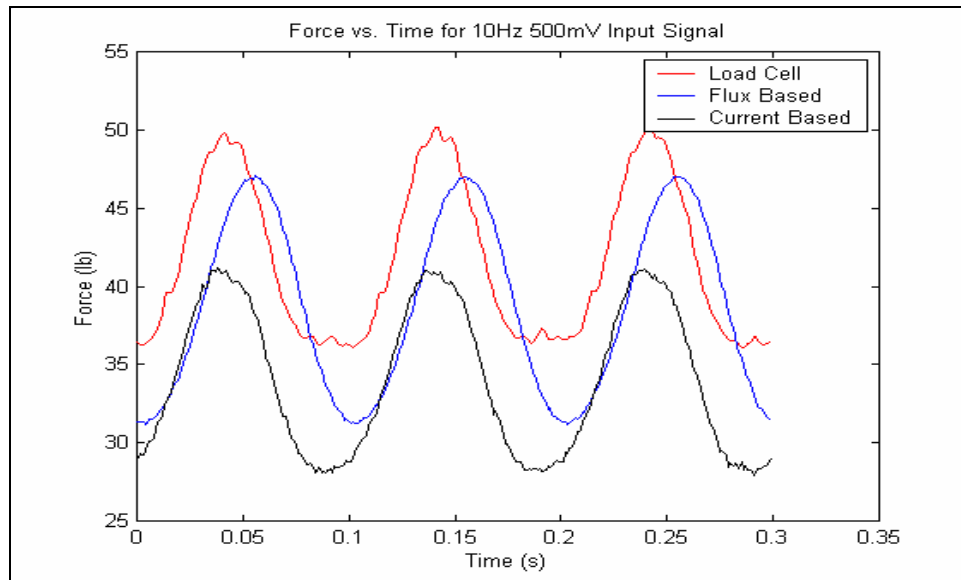


Figure 7.9: Dynamic Results for Input Frequency of 10Hz for Stiffer System

The flux based method still predicts the DC component of the load cell measurements more accurately, as before. However, the cause of the larger errors in the AC component measurements of the flux based resultants is unknown. Because the current and flux based methods are under predicting the load cell measurements, the system dynamics are probably not dominant at this low of an input frequency. This means that neglecting the dynamic component of the flux and current based reaction forces due to the inertia of the floating frame is still a valid assumption.

This is not true in the next dynamic loading case with an input frequency of 20Hz as shown in Figure 7.10. Frequency components of 40Hz and 60Hz can be seen in the

load cell measurement as well as a small 40Hz component in the current based resultant. These are due to harmonics because the input frequency is 20Hz having a stronger first harmonic of 40Hz and a weaker second harmonic of 60Hz.

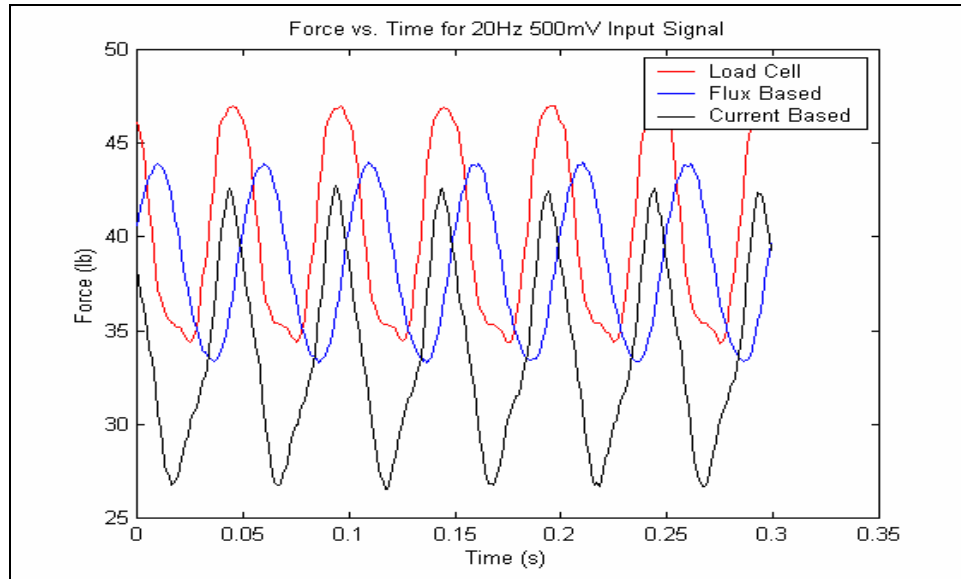


Figure 7.10: Dynamic Results for Input Frequency of 20Hz for Stiffer System

At this input frequency, it is evident that the amplitude of the flux based method is decreasing because the dynamic component due to the inertia of the floating frame is not included, while the amplitude of the current based method is increasing due to the hysteresis and eddy current effects. These effects appear at the same input frequency as they did in the original system, so increasing the stiffness has not affected these results. Dynamic components of the reaction forces due to the inertia of the floating frame should be corrected for at input frequencies of 20Hz and higher because of their effect on the flux based results.

Figure 7.11 presents the dynamic results for the stiffer system with an input frequency of 30Hz. Frequency components of 60Hz and 90Hz can be seen in the load cell measurement as well as a small 60Hz component in the current based resultant and a

smaller 60Hz component in the flux based resultant. These are due to harmonics rather than 60Hz noise because 60Hz and 90Hz are the first and second harmonics of the 30Hz input frequency, respectively.

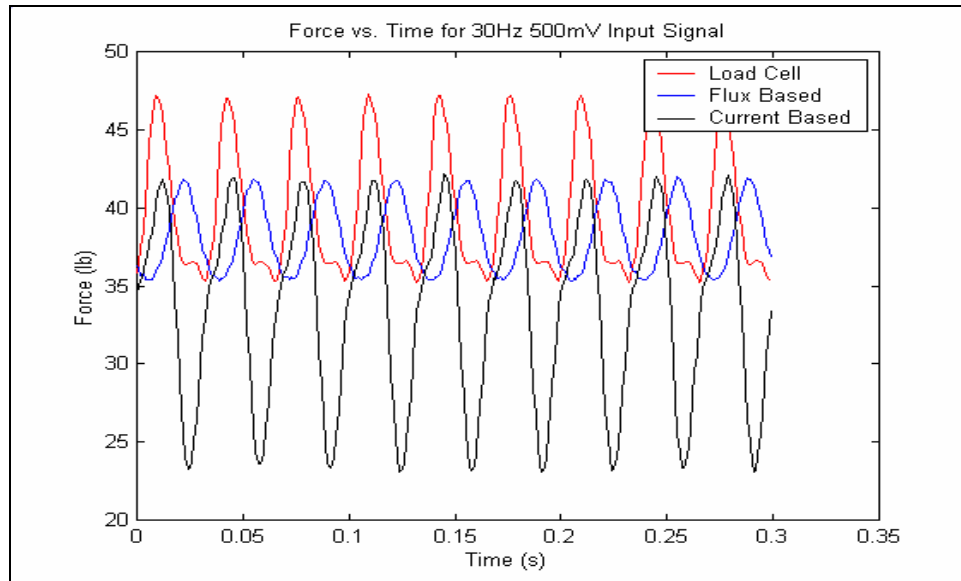


Figure 7.11: Dynamic Results for Input Frequency of 30Hz for Stiffer System

The load cell peak to peak amplitude is still about 12lb, while the flux based peak to peak amplitude is only about 7lb. Also, the phase difference between the load cell measurement and the flux based resultant is increasing with increasing input frequency. This means that in order to compare the load cell measurement to the flux based resultant, it will first be necessary to correct for the inertial component of the floating frame. The peak to peak amplitude of the current based method continues to increase as the input frequency increases due to hysteresis and eddy current effects.

The increase in amplitude of the current based results is even more dramatic with an input frequency of 50Hz as shown in Figure 7.12. It is evident from these results that the current based method is limited at measuring forces at higher frequencies where the hysteresis and eddy current effects are dominating. The flux based resultant is still scaled in phase and amplitude by the inertial component of the floating frame.

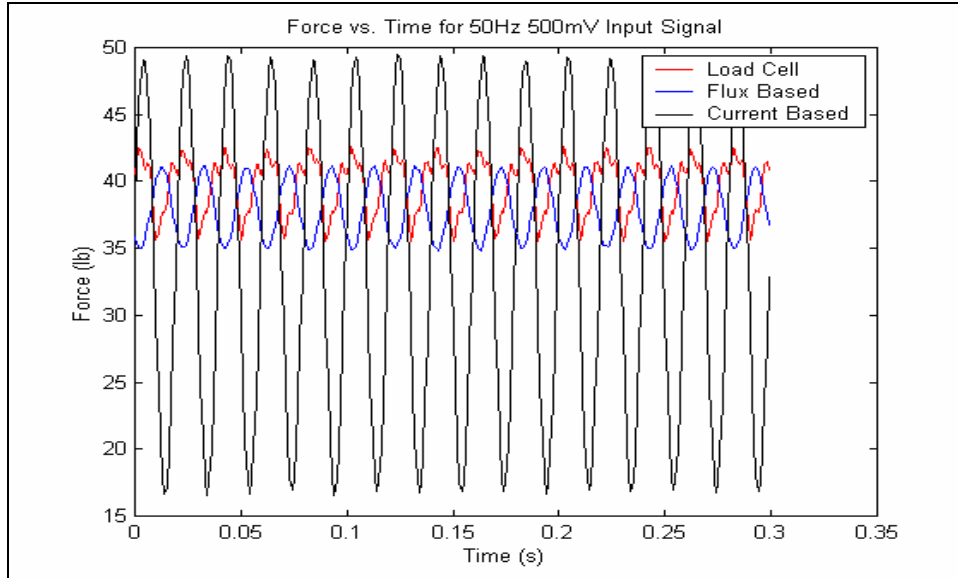


Figure 7.12: Dynamic Results for Input Frequency of 50Hz for Stiffer System

Harmonic components of 100Hz and 200Hz can be seen in the load cell measurement; however neither the flux based nor the current based methods show any harmonic components. The load cell measurement peak to peak force is only slightly smaller than the 7lb magnitude seen in the lower input frequencies. The initial decrease then increase, as seen in the results for the original system, is no longer seen in the results for the stiffer system. This could mean that increasing the stiffness has increased the resonance beyond the frequency range of interest.

To check this hypothesis, a swept sine wave from 5 to 50Hz was also input into the stiffer system. The “FORCE MEASURE” VI was again set up with a sampling rate of 500Hz acquiring 7500 samples per channel. The time responses for the load cell, flux based resultant, and current based resultant for the stiffer system are shown in Figure 7.13. In this plot, the frequency starts at 5Hz and increases 3Hz every second until it finally reaches 50Hz at 15 seconds. Thus, every second on the x-axis represents a 3Hz increase in frequency.

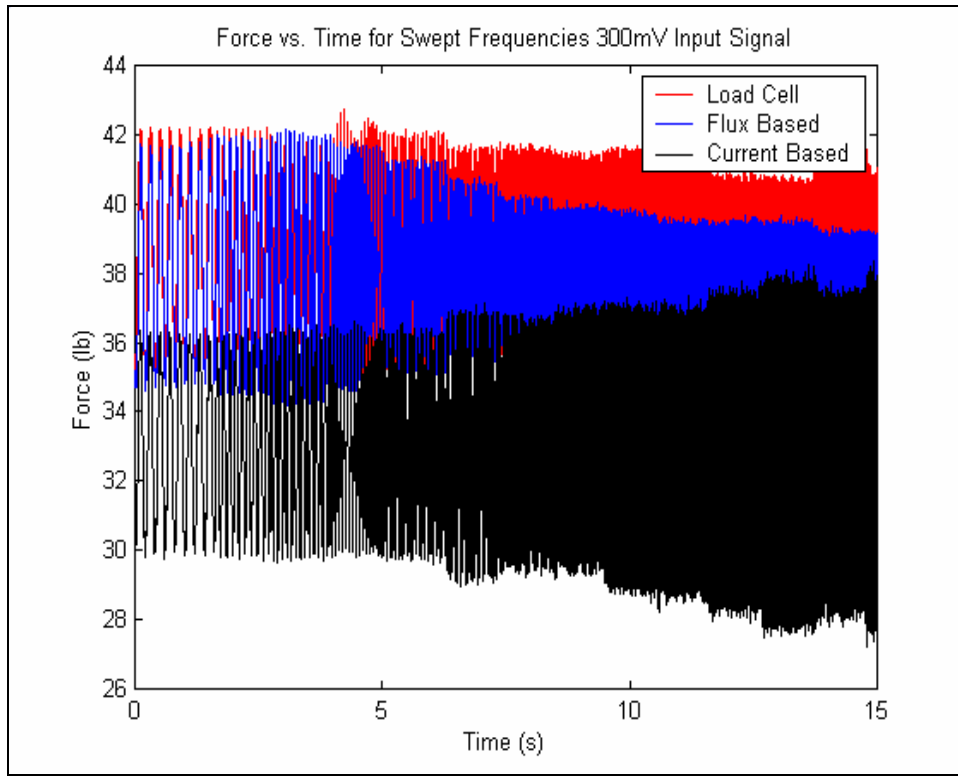


Figure 7.13: Time Response with Swept Sine Input For Stiffer System

After stiffening the thrust bearings, the magnitudes of all the measurements are higher at lower frequencies and lower at higher frequencies. Consequently, the response is more uniform over the entire frequency range. Figure 7.14 shows the load cell measurement plotted individually. Comparing the load cell results in Figure 7.14 for the stiffer system to those in Figure 7.7 for the original system, it is evident that increasing the stiffness of the thrust bearings has significantly reduced the response at higher frequencies. The decrease followed by the increase in response now occurs at about 14 seconds instead of the 11 seconds seen in the original system. This corresponds to a frequency of approximately 47Hz. This could be due to an increase in the resonant frequency of the system as a result of the increased stiffness of the thrust bearings. If the sine sweep were to continue increasing beyond 50Hz, the same increasing trend after resonance would be expected as seen the results for the original system.

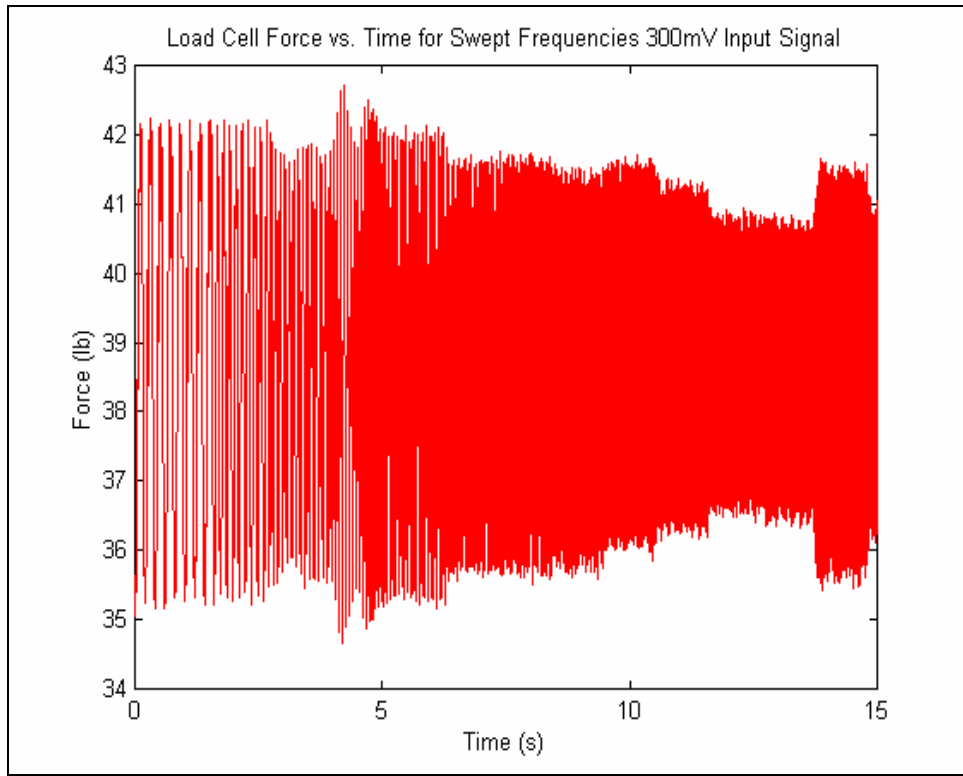


Figure 7.14: Time Response for Load Cell with Swept Sine Input For Stiffer System

Again, because the decreasing then increasing trend does not occur until about 14 seconds, it appears as though the resonant frequency has been increased from approximately 35Hz to about 47Hz simply by changing the gain parameters of the thrust bearings. The results shown in Figures 7.7 and 7.14 are consistent with an increase in the system resonant frequency; however, as stated previously, in order to completely determine whether or not the system is going through a resonance, a plot of phase versus frequency is needed. A phase shift of 180° would designate a system resonance. Again, time restrictions did not allow this to be investigated. These dynamic results show that it is possible that changing the gain parameters of the magnetic bearings can change the dynamics of the TMS demonstrator. This advantage to a magnetically levitated TMS would be useful in being able to control the system dynamics and avoid resonant responses when articles with significantly different masses are tested on the same test stand. No analytical model was performed on the dynamics of the TMS demonstrator because of time constraints and the confidence of the researchers in the ability to change the resonant frequencies of the system if problems arose.

Chapter 8

Summary of Results and Recommendations

8.1 Overview of Work Completed

A magnetically levitated rocket TMS demonstrator was designed, built and tested by Virginia Tech in conjunction with Joe Imlach of Imlach Consulting Engineering. This was done in response to a request by NASA to solve several problems with their existing rocket TMS designs. Existing TMSs at NASA take upwards of two weeks to calibrate, while the multipoint calibration technique used on the TMS demonstrator only takes about two hours. Also, misalignment problems with the strain gauges and load columns on existing TMSs cause cross axis forces to be measured; however, because the floating frame is completely levitated in a magnetic field and the targets have been oversized to allow the floating frame to move freely, neither misalignment nor cross axis forces are a problem for the demonstrator. The magnetically levitated TMS demonstrator also offers the unique capability of being able to measure a large range of test articles with various thrust outputs because of its ability to vary the range of accurate thrust measurement simply by energizing different numbers of thrust bearings. The magnetically levitated TMS demonstrator has been proven successful at answering all of the problems brought up by NASA while measuring forces within an accuracy of 99.5%.

Both static and dynamic forces were applied to the floating frame of the TMS demonstrator using a turnbuckle assembly for static testing and a magnetostrictive force actuator for dynamic testing. The input force was measured by a standard load cell, while the reaction forces at the bearings were measured using both flux based and current based force equations. To improve the accuracy of the force measurements, a calibration

technique known as the multipoint method was used to determine the physical air gaps for each of the axes of control. A fringing factor model, developed by Joe Imlach, that characterizes fringing as a function of air gap and bearing geometry, was also implemented into the flux and current based force equations to improve the accuracy of force measurements.

8.2 Summary of Results

The following is a list of the results for the static and dynamic testing as well as the thermal testing performed on the TMS demonstrator.

- The test rig was designed and built by Joe Imlach of Imlach Consulting, while Virginia Tech's role included the application of the multipoint calibration and software development, the implementation of a 128-channel data acquisition system, and the overall commissioning of the TMS demonstrator.
- The multipoint method calibration technique was used to determine the physical air gaps between the targets and actuators of all the bearing axes on the demonstrator allowing for accurate force calculations. The development of a communication interface between LabVIEW and the Revolve controllers would allow the calibration to be completely automated, taking only about two hours to complete. Also, this calibration technique does not require known loads to be applied to the system, making it ideal in a field situation.
- The static force accuracy is greater than 99.5% for the flux based method and greater than 94% for the current based method with all six thrust bearings energized. With only four thrust bearings energized, the static force accuracy is greater than 99.4% for the flux based method and greater than 92.5% for the current based method. So the accuracy of force measurement is only slightly affected by the number of thrust bearings that are energized. Also, if the accuracy of the load cell measurements is taken into account, it is possible that all of the flux based errors are within the maximum target error of 0.50%.

- There is no trend in the flux based errors; however, the current based errors increase linearly with load. Because of the deterministic nature of these errors, a correction factor could be applied to the current results that would significantly improve the accuracy of the current based force measurement. However, this would negate the goal of developing a calibration technique that can be used in a field situation and does not require known loads to be applied.
- The dynamic testing capability of the TMS demonstrator was proven qualitatively rather than quantitatively due to the absence of accelerometers to account for the dynamic component due to the inertia of the floating frame.
- The dynamic results suggest that increasing the stiffness of the thrust bearings increased the resonant frequency of the system from 35Hz to 47Hz. In order to completely determine whether or not the system is going through a resonance, a plot of phase versus frequency is needed; however, time restrictions did not allow this to be investigated. This ability to control the system dynamics and avoid resonant responses would be useful if articles with significantly different masses are tested on the same test stand.
- Thermal testing was also performed on the TMS demonstrator to determine the thermal sensitivity of the flux probes. The inability to isolate the thermal effects of the 37_ bearing made it impossible to apply individual correction factors to all the bearings. Thus, the flux based results in these tests are not corrected for the thermal sensitivity of the flux probes. It should be noted, however, that the flux based errors are still within the 0.50% maximum target error if the accuracy of the load cell measurements is taken into account.

8.3 Recommendations for Future Work

A list of recommendations for future possible improvements is given below.

- A separate calibration curve should be determined for each flux probe. This would be possible if thermal testing took place prior to system assembly. A separate thermal calibration curve for each flux sensor would account for the thermal sensitivity of the flux probes resulting in even higher accuracies in the flux based force calculations.
- The dynamic testing results could not be analyzed quantitatively because the floating frame was not equipped with accelerometers. Placing accelerometers at each of the targets to measure the acceleration of the floating frame at each axis, would allow the reaction forces at each bearing to be corrected for the inertial component of the floating frame. This would allow the errors between the load cell measurements and the flux and current based results to be calculated for dynamic loading.
- The determination of a transfer function between force and position could be used to completely determine the resonant frequencies of the original and stiffer systems. A phase shift of 180° would designate the system passing through a resonance. Phase plots for the transfer functions of both systems are needed to determine whether the original system has a resonance at 35Hz and the stiffer system has a resonance at 47Hz.
- The dynamic testing results found that there are limitations in accuracy of the current based method at higher frequencies due to hysteresis and eddy current effects. It would be desirable to know the dynamic range over which the current based method calculates the applied loads within a certain accuracy. This could be accomplished by starting at a low frequency and increasing the frequency in small steps until a maximum desired error in the current based method is

obtained. The frequency at which this maximum error occurred would determine the dynamic range for the current based method.

- The flux and current based fringing factors were determined to be functions of the air gap to pole width ratio. Recent work by Joe Imlach has also shown the fringing to be a function of the amount of current running through the actuator coils. For the work presented in this paper, the current dependency of the fringing factor was removed by averaging the MFEA results over the expected current range of the actuator coils. A more accurate fringing factor could be calculated by determining the fringing factor as a function of both the air gap to pole width ratio as well as the coil currents, which are readily available from the controller. This would further increase the accuracy of force measurements capable with both the flux and current based methods.

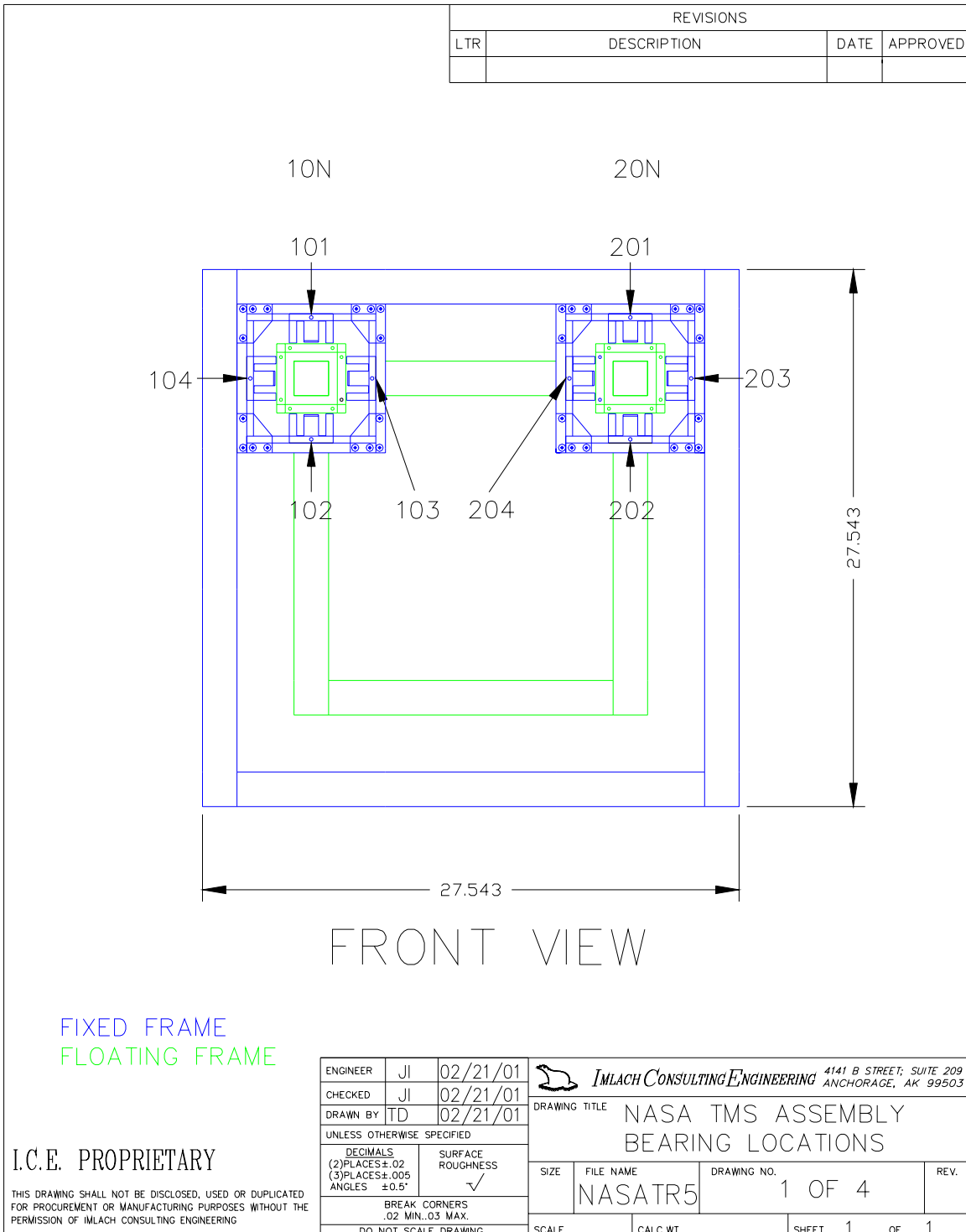
References

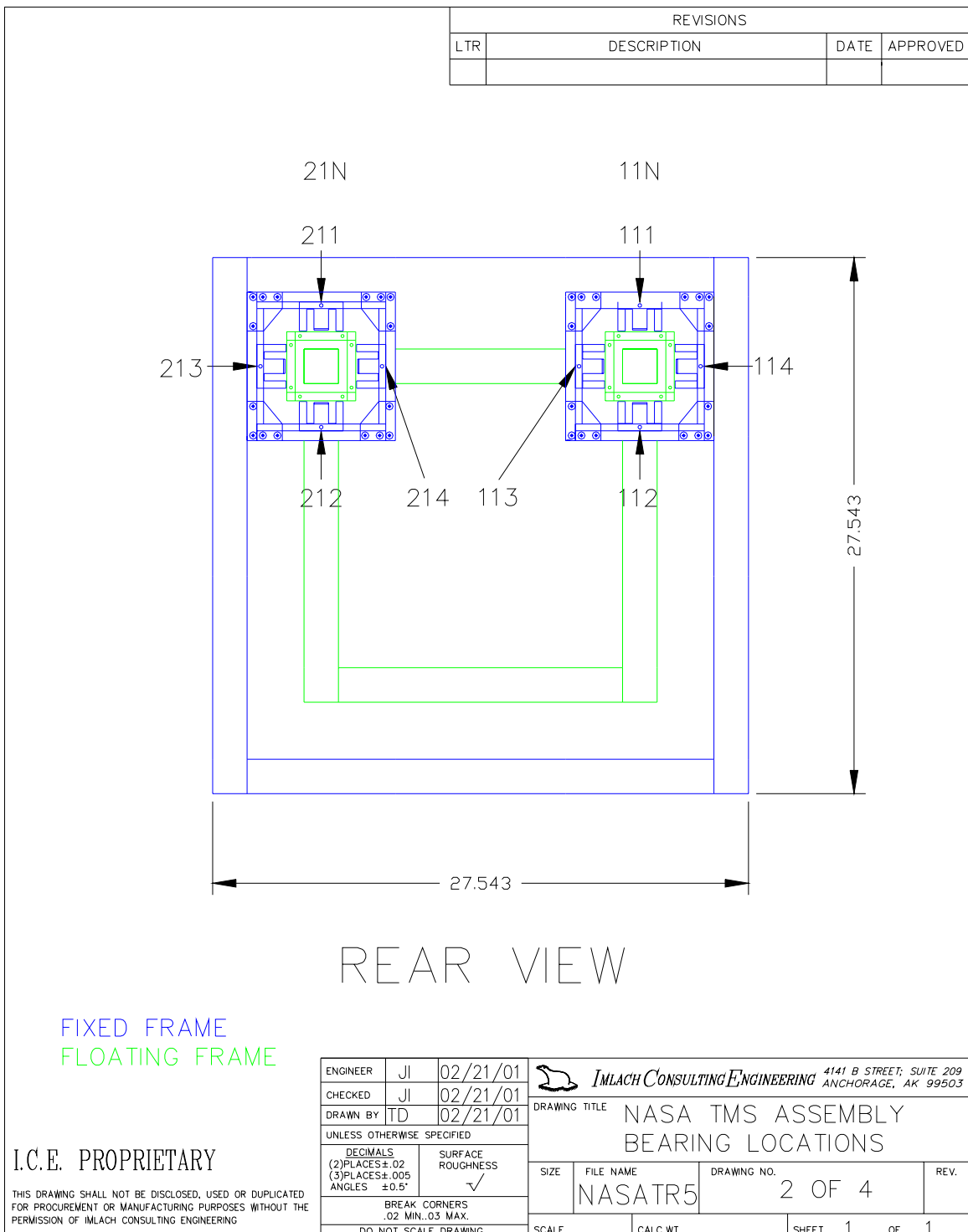
1. Aenis, M., Nordmann, R., 1999, "A Precise Force Measurement in Magnetic Bearings for Diagnosis Purposes," presented at the *5th International Symposium on Magnetic Suspension Technology*, Santa Barbara, CA, USA, December 1-3, 1999.
2. Aenis, M., Nordmann, R., 2000, "Active Magnetic Bearings for Fault Detection in a Centrifugal Pump," presented at the *7th International Symposium on Magnetic Bearings*, Zurich, Switzerland, August 23-25, 2000.
3. ANSI/ASME, "Measurement Uncertainty," *Supplement to ASME Performance Test Codes*, ANSI/ASME PTC 19.1-1985.
4. Baun, D. O., Fittro, R. L., Maslen, E. H., 1996, "Force Versus Current and Air Gap Calibration of a Double Acting Magnetic Thrust Bearing," presented at the *International Gas Turbine & Aeroengine Congress and Exhibition*, Birmingham, UK, June 2-5. ASME pamphlet paper no. 96-GT-121.
5. Baun, D. O., Flack, R. D., 1999, "A Plexiglas Research Pump with Calibrated Magnetic Bearings/Load Cells for Radial and Axial Hydraulic Force Measurement," *Journals of Fluids Engineering*, Vol. 121, March, pp 126-132.
6. Fittro, R. L., Baun, D. O., Maslen, E. H., Allaire, P. E., 1997, "Calibration of an 8-Pole Planar Radial Magnetic Actuator," presented at the *International Gas Turbine & Aeroengine Congress and Exhibition*, Orlando, FL, June 2-5.
7. Guinzburg, A. and Buse, F. W., 1994, "Axial and Radial Forces on a Pump Impeller Obtained with a Magnetic-Bearing Force Measurement Rig," *Proceedings of the Fourth International Symposium on Magnetic Bearings*, August, ETH Zurich, pp 537-545.
8. Guinzburg, A. and Buse, F. W., 1995, "Magnetic Bearings as an Impeller Force Measurement Technique," *Proceedings of the Twelfth International Pump Users Symposium*, March, pp 69-76.
9. Imlach, J., Blair, B. J., Allaire, P. E., 1990, "Measured and Predicted Force and Stiffness Characteristics of Industrial Magnetic Bearings," *ASME/STLE Tribology Conference*, Toronto, Canada, October 7-10.
10. Imlach, J., Kasarda, M. E. F., and Balaji, P. A., 2000, "Enhancements to AMB Force Measurement Procedures for Application To a Rocket Thrust Measurement System," presented at the *International Gas Turbine & Aeroengine Congress and Exhibition*, Munich, Germany, May 8-11. ASME pamphlet no. 2000-GT-0414.
11. Kasarda, M. E. F., 2000, "An Overview of Active Magnetic Bearing Technology and Applications," Virginia Polytechnic Institute and State University.
12. Kasarda, M., Imlach, J., Balaji, P. A., Marshall, J., 2000, "The Concurrent Use of Magnetic Bearings for Rotor Support and Force Sensing for the Nondestructive Evaluation of Manufacturing Processes," *Proceedings of the International Society for Optical Engineering (SPIE)*, Newport Beach, CA, March 6-9, pp 352-363.
13. Kasarda, M. E. F., 1999, "Magnetic Bearings for Improved Process Control," 1999 NSF Grantees Conference Proceedings, Long Beach, CA, January.
14. Knopf, E., Nordmann, R., 1998, "Active Magnetic Bearings for the Accurate Force Measurement in Rotating Machinery," MOVIC 1998, Zurich, 1998.

15. Marshall, J., Kasarda, M. E. F., 2000, "A Multipoint Measurement Technique for the Enhancement of Force Measurement with Active Magnetic Bearings (AMB)," Virginia Polytechnic Institute and State University.
16. Plonus, M. A., 1978, "Applied Electronics," McGraw-Hill, New York.
17. Wagner, N. G., Steff, K., 1998, "Dynamic Labyrinth Coefficients from a High-Pressure Full-Scale Test Rig Using Magnetic Bearings," DEMAG DELAVAL Turbomachinery, Duisburg, Germany.

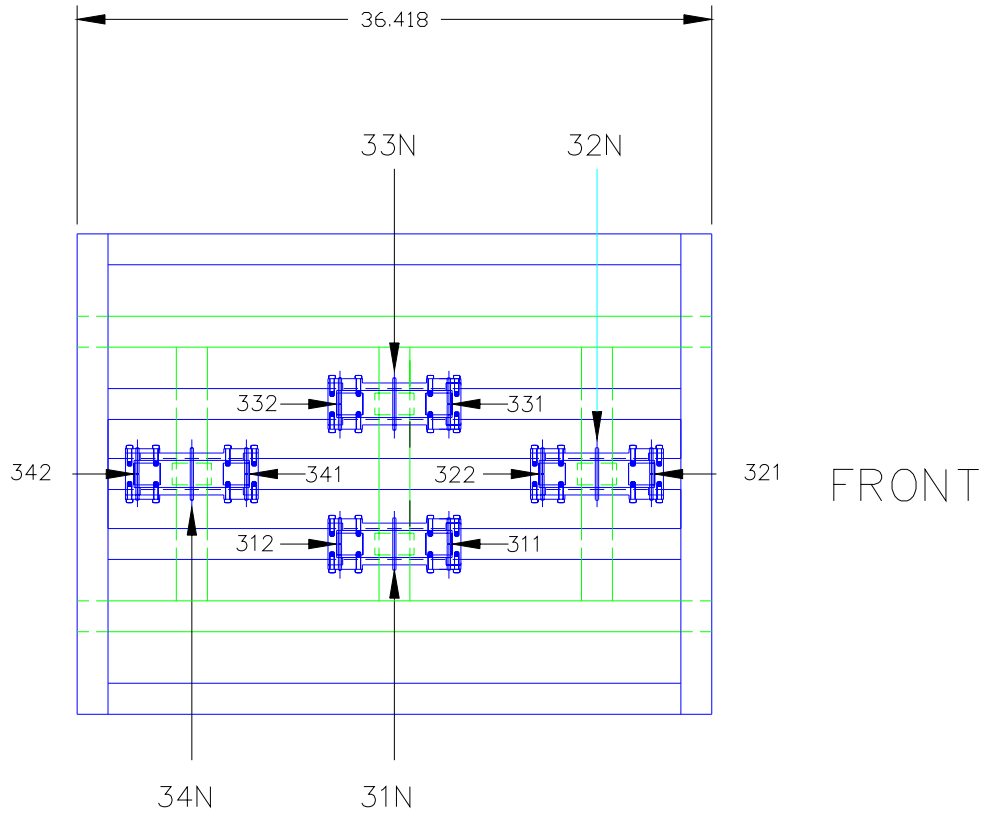
Appendix A

Scale Drawings of the TMS Demonstrator





| REVISIONS | | | |
|-----------|-------------|------|----------|
| LTR | DESCRIPTION | DATE | APPROVED |
| | | | |



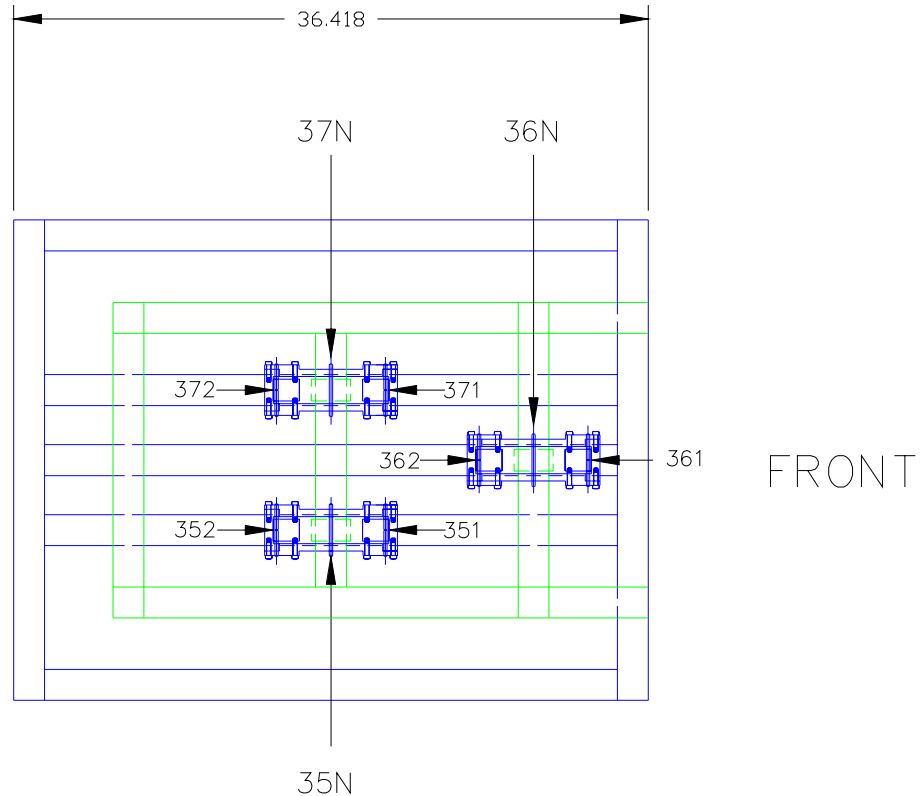
TOP VIEW OF TOP BEARINGS

FIXED FRAME FLOATING FRAME

J.C. E. PROPRIETARY

THIS DRAWING SHALL NOT BE DISCLOSED, USED OR DUPLICATED
FOR PROCUREMENT OR MANUFACTURING PURPOSES WITHOUT THE
PERMISSION OF IMLACH CONSULTING ENGINEERING

| | | | | |
|---|-----------|----------------------------|--|------|
| ENGINEER | JL | 02/21/01 |  IMLACH CONSULTING ENGINEERING 4141 B STREET, SUITE 209 ANCHORAGE, AK 99503 | |
| CHECKED | JL | 02/21/01 | | |
| DRAWN BY | TD | 02/21/01 | | |
| UNLESS OTHERWISE SPECIFIED | | | | |
| DECIMALS (2)PLACES±.02 (3)PLACES±.005 ANGLES ±.05° | | SURFACE ROUGHNESS ✓ | | |
| BREAK CORNERS .02 MIN..03 MAX. | | | | |
| DO NOT SCALE DRAWING | | | | |
| DRAWING TITLE NASA TMS ASSEMBLY BEARING LOCATIONS | | | | |
| SIZE | FILE NAME | | DRAWING NO. | REV. |
| | NASATR5 | | 3 OF 4 | |
| SCALE | CALC.WT. | | SHEET 1 | OF 1 |



TOP VIEW OF BOTTOM BEARINGS

FIXED FRAME
FLOATING FRAME

I.C.E. PROPRIETARY

THIS DRAWING SHALL NOT BE DISCLOSED, USED OR DUPLICATED
FOR PROCUREMENT OR MANUFACTURING PURPOSES WITHOUT THE
PERMISSION OF IMLACH CONSULTING ENGINEERING

| | | | | | | |
|--|----|-----------|---|--------|--|--|
| ENGINEER | JI | 02/21/01 | IMLACH CONSULTING ENGINEERING 4141 B STREET, SUITE 209 ANCHORAGE, AK 99503 | | | |
| CHECKED | JI | 02/21/01 | | | | |
| DRAWN BY | TD | 02/21/01 | | | | |
| UNLESS OTHERWISE SPECIFIED | | | | | | |
| DECIMALS (2) PLACES ± .02 (3) PLACES ± .005 ANGLES ± 0.5° | | | | | | |
| SURFACE ROUGHNESS ✓ | | | | | | |
| BREAK CORNERS .02 MIN., .03 MAX. | | | | | | |
| DO NOT SCALE DRAWING | | | | | | |
| SIZE | | FILE NAME | DRAWING NO. | REV. | | |
| NASATR5 | | | 4 OF 4 | | | |
| SCALE | | CALC.WT. | SHEET | 1 OF 1 | | |

Appendix B

Uncertainty Analysis

B.1 Introduction

The force calculations for both the current based and flux based methods have uncertainties associated with them, which can be due to variations in the pole dimensions due to manufacturing as well as variations in the gains for the sensors. The overall uncertainty of any derived value can be found using Equation B.1 (ANSI/ASME, 1985).

$$u_x = \sqrt{\sum_{n=1}^i \left(u_i \frac{\partial x}{\partial i} \right)^2} \quad \text{B.1}$$

In Equation B.1, u_x is the uncertainty of the variable x , i is the number of variables associated with the expression for x , u_i is the uncertainty of the variable I , and $\frac{\partial x}{\partial i}$ is the partial derivative of x with respect to the variable i .

The equation for the volume of a cylinder will be used to show how Equation B.1 is applied. The volume of a cylinder is calculated using the following equation:

$$V = \pi r^2 h \quad \text{B.2}$$

where r is the radius of the cylinder and h is the height of the cylinder. Given that the radius of the cylinder is $8.0\text{in}\pm0.05\text{in}$ and the height of the cylinder is $15.0\text{in}\pm0.05\text{in}$, the partial of V with respect to r is calculated using Equation B.3.

$$\frac{\partial V}{\partial r} = 2\pi rh \quad \text{B.3}$$

Equation B.3 evaluated with the given information results in a value of 753.982in². The partial of V with respect to h is calculated using Equation B.4.

$$\frac{\partial V}{\partial h} = \pi r^2 \quad \text{B.4}$$

Equation B.4 evaluated with the given information results in a value of 201.062in². The volume of the cylinder is 3015.929in³ using Equation B.2 and the given information. So, the uncertainty of the volume calculation can now be calculated using Equation B.5.

$$u_V = \sqrt{\left(u_r \frac{\partial V}{\partial r}\right)^2 + \left(u_h \frac{\partial V}{\partial h}\right)^2} \quad \text{B.5}$$

or

$$u_V = \sqrt{(0.05in * 753.982in^2)^2 + (0.05in * 201.062in^2)^2} \quad \text{B.5}$$

Equation B.5 simplifies to 39.016in³. So, the volume of the cylinder is 3015.929in³±39.016in.

This same type of uncertainty analysis was performed on both the current based and flux based force equations. The data for the vertical axis of Bearing 10_ with an axial load of about 20lb applied to the frame is used to give a general uncertainty analysis on the force equations. Due to the complexity of the force equations, Mathematica was used to calculate the uncertainties. The printouts from Mathematica can be found in Section B.4. The next two sections show the uncertainty analysis for each force equation.

B.2 Uncertainty Analysis for Current Based Force Equations

Three uncertainty analyses were performed prior to the uncertainty analysis for the current based force equation because there are three nested functions in the current based force equation. The current based force equation developed in Chapter 2 is shown below for reference.

$$F = \frac{\mu_o N^2 A_g}{2} \left(\frac{ff_1 I_1^2}{\left(\frac{L_i}{\mu_r} + 2(g_o - x) \right)^2} - \frac{ff_2 I_2^2}{\left(\frac{L_i}{\mu_r} + 2(g_o + x) \right)^2} \right) \quad (2.24)$$

where

$$\begin{aligned} ff_1 = & \frac{1}{2} \left[A_i e^{-\alpha_i \left(\frac{g_{o1}-x}{W_1} \right)} + K_i \left[A_i e^{-\alpha_i \left(\frac{g_{o1}-x}{W_2} \right)} + K_i \right] \right. \\ & \left. + \frac{1}{2} \left[A_i e^{-\alpha_i \left(\frac{g_{o2}-x}{W_3} \right)} + K_i \left[A_i e^{-\alpha_i \left(\frac{g_{o2}-x}{W_4} \right)} + K_i \right] \right] \right] \end{aligned} \quad (2.22)$$

$$\begin{aligned} ff_2 = & \frac{1}{2} \left[A_i e^{-\alpha_i \left(\frac{g_{o1}+x}{W_1} \right)} + K_i \left[A_i e^{-\alpha_i \left(\frac{g_{o1}+x}{W_2} \right)} + K_i \right] \right. \\ & \left. + \frac{1}{2} \left[A_i e^{-\alpha_i \left(\frac{g_{o2}+x}{W_3} \right)} + K_i \left[A_i e^{-\alpha_i \left(\frac{g_{o2}+x}{W_4} \right)} + K_i \right] \right] \right] \end{aligned} \quad (2.23)$$

First, the uncertainty of the air gap area, A_g , must be determined. Because the fringing factor is based on the bearing geometry, the equation for the air gap area assumes that the area of the gap over which the flux is distributed is equal to the pole face area. The equation used to calculate the air gap area is shown in Equation B.6.

$$A_g = 2LW_1 + LW_2 \quad B.6$$

Because the E-core actuators were manufactured using automated processes, the uncertainties of the pole face measurements are assumed to be $\pm 0.005\text{in}$. A summary of

the variables and uncertainties used to find the uncertainty in the air gap area is shown in Table B.1.

Table B.1: Variables and Uncertainties Used to Find Uncertainty of the Air Gap Area

| Variable | Value | Uncertainty |
|----------------|----------------------|--------------------------|
| L | 1.25in | 0.005in |
| W ₁ | 0.375in | 0.005in |
| W ₂ | 0.75in | 0.005in |
| A _g | 1.875in ² | 0.0158607in ² |

Next, the uncertainties in the fringing equations (Equations 2.22 and 2.23) must be determined. All position measurements are assumed to have an uncertainty of $\pm 0.0005\text{in}$ because of the gain used for the position sensors. The pole dimensions W₁, W₂, W₃, and W₄ are assumed to have an uncertainty of 0.005in because of the manufacturing processes used to assemble the E-cores. A summary of the variables and uncertainties used to find the uncertainties in the fringing factors is shown in Table B.2.

Table B.2: Variables and Uncertainties Used to Find Uncertainty of the Current Based Fringing Factors

| Variable | Value | Uncertainty |
|------------------|----------------|-------------|
| A _i | 1.00 | 0.0005 |
| α_i | 160 | 0.5 |
| g _{o1} | 0.0375in | 0.0005in |
| g _{o2} | 0.0875in | 0.0005in |
| x | -0.000035456in | 0.0005in |
| x _{ptp} | -0.00261in | 0.0005in |
| W ₁ | 0.375in | 0.005in |
| W ₂ | 1.25in | 0.005in |
| W ₃ | 0.75in | 0.005in |
| W ₄ | 1.25in | 0.005in |
| K _i | 1.104 | 0.0005 |
| ff ₁ | 1.22206 | 0.0011655 |
| ff ₂ | 1.22520 | 0.0013216 |

After the uncertainties in the air gap area and both fringing factors have been found, it is possible to find the uncertainty in the current based force equation. Table B.3 shows the variables and their corresponding uncertainties used to find the uncertainty in the current based force equation.

Table B.3: Variables and Uncertainties Used to Find Uncertainty of the Current Based Force Equation

| Variable | Value | Uncertainty |
|------------------|----------------------|--------------------------|
| A _g | 1.875in ² | 0.0158607in ² |
| ff ₁ | 1.22206 | 0.00116548 |
| I ₁ | 1.853947A | 0.00005A |
| g _o | 0.0625in | 0.0005in |
| x | -0.000035456in | 0.0005in |
| x _{ptp} | -0.00261in | 0.0005in |
| L _i | 4.5in | 0.05in |
| μ _i | 3000 | 500 |
| ff ₂ | 12252 | 0.00132155 |
| I ₂ | 0.358461A | 0.00005A |
| F | 23.1505lb | 0.56345lb |

So, the current based force equation calculates the force to be $23.1505\text{lb} \pm 0.56345\text{lb}$. In terms of percent error full load, the 0.56345lb uncertainty in the force measurement corresponds to about 0.37% error full load assuming four bearings are energized in the Y-direction.

B.3 Uncertainty Analysis for Flux Based Force Equations

The same analysis is performed on the flux based force equation as the current based force equation. The flux based force equation derived in Chapter 2 is shown below

$$F = \frac{A_g}{2\mu_o} (ff_1 B_1^2 - ff_2 B_2^2) \quad (2.9)$$

where

$$ff_1 = A_b e^{-\alpha_b \left(\frac{g_o - x}{W} \right)} + K_b \quad (2.10)$$

$$ff_2 = A_b e^{-\alpha_b \left(\frac{g_o + x}{W} \right)} + K_b \quad (2.11)$$

The air gap area for the flux based force equation is the same as that of the current based force equation, so this uncertainty analysis will not be repeated. The results for the

uncertainty analysis of the air gap area are summarized in Table B.1. Because the fringing factor equations are different, however, an uncertainty analysis of the flux based fringing factor equations must be performed. Table B.4 summarizes the variables and uncertainties used to calculate the uncertainties in the flux based fringing equations.

Table B.4: Variables and Uncertainties Used to Find Uncertainty of the Flux Based Fringing Factors

| Variable | Value | Uncertainty |
|-----------|----------------|-------------|
| A_b | 1.542 | 0.0005 |
| a_b | 40 | 0.5 |
| g_0 | 0.0625in | 0.0005in |
| x | -0.000035456in | 0.0005in |
| x_{ptp} | -0.0044325in | 0.0005in |
| W | 1.25in | 0.005in |
| K_b | 1.057 | 0.0005 |
| ff_1 | 1.23788 | 0.00715988 |
| ff_2 | 1.29776 | 0.00889984 |

After the uncertainty analyses have been performed on the air gap area and the flux based fringing equations, it is possible to calculate the uncertainty of the flux based force equation. The results for this analysis are shown in Table B.5.

Table B.5: Variables and Uncertainties Used to Find Uncertainty of the Current Based Force Equation

| Variable | Value | Uncertainty |
|----------|----------------------|--------------------------|
| A_g | 1.875in ² | 0.0158607in ² |
| ff_1 | 1.23788 | 0.00715988 |
| B_1 | 0.40756T | 0.00005T |
| ff_2 | 1.29776 | 0.00889984 |
| B_2 | 0.099041T | 0.00005T |
| F | 20.8704lb | 0.218741lb |

Therefore, the flux based equations calculate a force of $20.8704\text{lb} \pm 0.218741\text{lb}$. This corresponds to a percent full load of about 0.14% assuming four bearings are energized in the Y-direction. These results show that the flux based force equation is almost half as sensitive as the current based force equation to measurement uncertainty, another advantage of the flux based method to the current based method.

B.4 Mathematica Code Used in the Uncertainty Analysis

Code for Uncertainty of Air Gap Area:

```

ClearAll [Ag,L,W1,W2]
Ag [L_,W1_,W2_]:=2*L*W1+L*W2
Ag [1.25,0.375,0.75]
1.875
pdL=D [Ag [L,0.375,0.75],L]
1.5
pdW1=D [Ag [1.25,W1,0.75],W1]
2.5
pdW2=D [Ag [1.25,0.375,W2],W2]
1.25
uL=0.005;
uW1=0.005;
uW2=0.005;
\!\!(UAg = Sqrt[\!\!((uL*pdL)\!)^2 + \!\!((uW1*pdW1)\!)^2 +
\!\!((uW2*pdW2)\!)^2])
0.0158607

```

Code for Uncertainty of Current Based Top Fringing Equation (ff1):

```

ClearAll[ff1,Ai,\Alpha_i,go1,go2,x,xptp,w1,w2,w3,w4,ki]
\!\!(ff1[Ai_, \Alpha_i_, go1_, go2_, x_, xptp_, w1_, w2_, w3_, w4_, ki_]:= 
0.5*\!\!((\!\!((\!\!((\!\!((Ai*Exp[\!\!(-\!\![Alpha]\!)_i\!])* \!\!(go1 - \!\!((x +
xptp)\!) / \!\!w1])\!)) + ki)
\!\!)*\!\!((\!\!((\!\!((Ai*Exp[\!\!(-\!\![Alpha]\!)_i\!])* \!\!(go1 - \!\!((x +
xptp)\!) / \!\!w2])\!)
\!\! + \!\!((\!\!((\!\!((\!\!((Ai*Exp[\!\!(-\!\![Alpha]\!)_i\!])* \!\!(go2 - \!\!((x +
xptp)\!) / \!\!w3])\!)) + \!\!((ki)\!)*\!\!((\!\!((\!\!((Ai*Exp[\!\!(-\!\![Alpha]\!)_i\!])* \!\!(go2 - \!\!((x +
xptp)\!) / \!\!w4])\!)) + \!\!((ki)\!)))\!)))
ff1[1.00,160,0.0375,0.0875,-0.000035456,-
0.00261,0.375,1.25,0.75,1.25,1.104]
1.22206
D[ff1[Ai,160,0.0375,0.0875,-0.000035456,-
0.00261,0.375,1.25,0.75,1.25,1.104],
Ai]
0.5 (9.74634\times10\^-6 (1.104\ [InvisibleSpace] + 4.44702\times10\^-9 (
Ai) + 0.00586579
(1.104\ [InvisibleSpace] + 3.63989\times10\^-8 Ai) + 4.44702\times10\^-9 (
1.104\ [InvisibleSpace] + 9.74634\times10\^-6 Ai) + 3.63989\times10\^-8 (
1.104\ [InvisibleSpace] + 0.00586579 Ai))
pdAi=%/.Ai->1.00
0.00324332
D[ff1[1.00,\Alpha_i,0.0375,0.0875,-0.000035456,-
0.00261,0.375,1.25,0.75,1.25,
1.104],\Alpha_i]
0.5 (-0.0721164
E\^-0.0721164 \Alpha_i (
1.104\ [InvisibleSpace] + 1. E\^-0.120194 \Alpha_i) - 0.0321164
E\^-0.0321164 \Alpha_i (

```

```

    1.104\[InvisibleSpace]+1. E\^-0.107055 \[Alpha]i)-0.120194
    E\^-0.120194 \[Alpha]i (
    1.104\[InvisibleSpace]+1. E\^-0.0721164 \[Alpha]i)-0.107055
    E\^-0.107055 \[Alpha]i (
    1.104\[InvisibleSpace]+1. E\^-0.0321164 \[Alpha]i))
pd\[Alpha]i=%/.\[Alpha]i->160
-0.000104381
D[ff1[1.00,160,go1,0.0875,-0.000035456,-
0.00261,0.375,1.25,0.75,1.25,1.104],
go1]
0.5 (-128.
    E\^-128. (0.00264546\[InvisibleSpace]+go1) (
    1.104\[InvisibleSpace]+1.
        E\^-426.667 (0.00264546\[InvisibleSpace]+go1))-426.667
    E\^-426.667 (0.00264546\[InvisibleSpace]+go1) (
    1.104\[InvisibleSpace]+1.
        E\^-128. (0.00264546\[InvisibleSpace]+go1)))
pdgo1=%/.go1->0.0375
-0.414462
D[ff1[1.00,160,0.0375,go2,-0.000035456,-
0.00261,0.375,1.25,0.75,1.25,1.104],
go2]
0.5 (-128.
    E\^-128. (0.00264546\[InvisibleSpace]+go2) (
    1.104
        \[InvisibleSpace]+1.
            E\^-213.333 (0.00264546\[InvisibleSpace]+go2))-213.333
    E\^-213.333 (0.00264546\[InvisibleSpace]+go2) (
    1.104\[InvisibleSpace]+1.
        E\^-128. (0.00264546\[InvisibleSpace]+go2)))
pdgo2=%/.go2->0.0875
-0.000689161
D[ff1[1.00,160,0.0375,0.0875,x,-0.00261,0.375,1.25,0.75,1.25,1.104],x]
0.5 (128.
    E\^-128. (0.04011\[InvisibleSpace]-x) (
    1.104\[InvisibleSpace]+1.
        E\^-426.667 (0.04011\[InvisibleSpace]-x))+426.667
    E\^-426.667 (0.04011\[InvisibleSpace]-x) (
    1.104\[InvisibleSpace]+1.
        E\^-128. (0.04011\[InvisibleSpace]-x))+128.
    E\^-128. (0.09011\[InvisibleSpace]-x) (
    1.104\[InvisibleSpace]+1.
        E\^-213.333 (0.09011\[InvisibleSpace]-x))+213.333
    E\^-213.333 (0.09011\[InvisibleSpace]-x) (
    1.104\[InvisibleSpace]+1. E\^-128. (0.09011\[InvisibleSpace]-
x)))
pdx=%/.x-->-0.000035456
0.415151
D[ff1[1.00,160,0.0375,0.0875,-
0.000035456,xptp,0.375,1.25,0.75,1.25,1.104],
xptp]
0.5 (128.
    E\^-128. (0.0375355\[InvisibleSpace]-xptp) (
    1.104\[InvisibleSpace]+1.
        E\^-426.667 (0.0375355\[InvisibleSpace]-xptp))+426.667
    E\^-426.667 (0.0375355\[InvisibleSpace]-xptp) (
    1.104\[InvisibleSpace]+1.

```

```

E\^-128. (0.0375355\[InvisibleSpace]-xptp))+128.
E\^-128. (0.0875355\[InvisibleSpace]-xptp) (
1.104\[InvisibleSpace]+1.
E\^-213.333 (0.0875355\[InvisibleSpace]-xptp))+213.333
E\^-213.333 (0.0875355\[InvisibleSpace]-xptp) (
1.104\[InvisibleSpace]+1.
E\^-128. (0.0875355\[InvisibleSpace]-xptp)))
pdxptp=%/.xptp->-0.00261
0.415151
D[ff1[1.00,160,0.0375,0.0875,-0.000035456,-
0.00261,w1,1.25,0.75,1.25,1.104],
w1]
\!\(\(\(3.56448545418105711`\ E\^\(\(\(-
6.42327295999999936`\)/w1\)\)\)\/w1\^2\)
pdw1=%/.w1->0.375
9.22619\times10\^-7
D[ff1[1.00,160,0.0375,0.0875,-0.000035456,-
0.00261,0.375,w2,0.75,1.25,1.104],
w2]
\!\(\(\(3.54564679081996336`\ E\^\(\(\(-
6.42327295999999936`\)/w2\)\)\)\/w2\^2\)
pdw2=%/.w2->1.25
0.0133107
D[ff1[1.00,160,0.0375,0.0875,-0.000035456,-
0.00261,0.375,1.25,w3,1.25,1.104],
w3]
\!\(\(\(7.96171696100639803`\ E\^\(\(\(-
14.4232729600000002`\)/w3\)\)\)\/w3\^2\)
pdw3=%/.w3->0.75
6.29439\times10\^-8
D[ff1[1.00,160,0.0375,0.0875,-0.000035456,-
0.00261,0.375,1.25,0.75,w4,1.104],
w4]
\!\(\(\(7.96164670599032486`\ E\^\(\(\(-
14.4232729600000002`\)/w4\)\)\)\/w4\^2\)
pdw4=%/.w4->1.25
0.000049662
D[ff1[1.00,160,0.0375,0.0875,-0.000035456,-
0.00261,0.375,1.25,0.75,1.25,ki],
ki]
0.5 (0.00587558\[InvisibleSpace]+4 ki)
pdki=%/.ki->1.104
2.21094
uAi=0.0005;
u\[Alpha]i=0.5;
ugoi=0.0005;
ugo2=0.0005;
ux=0.0005;
uxptp=0.0005;
uw1=0.005;
uw2=0.005;
uw3=0.005;
uw4=0.005;
uki=0.0005;
\!\(Uff1curr =
Sqrt[\((uAi*pdAi)\)\^2 + \((u\[Alpha]i*pd\[Alpha]i)\)\^2 +

```

```

\((ugo1*pdgo1)\)\^2 + \((ugo2*pdgo2)\)\^2 +
\n\t\t\t\((ux*pdx)\)\^2 +
\((uxptp*pdxptp)\)\^2 + \((uw1*pdw1)\)\^2 + \((uw2*pdw2)\)\^2 +
\((uw3*pdw3)\)\^2 + \((uw4*pdw4)\)\^2 + \((uki*pdki)\)\^2] \\
0.00116548

```

Code for Uncertainty of Current Based Bottom Fringing Equation (ff₂):

```

ClearAll[ff2,Ai,\Alpha_i,go1,go2,x,xptp,w1,w2,w3,w4,ki]
\!\!\!(ff2[Ai_, \Alpha_i_, go1_, go2_, x_, xptp_, w1_, w2_, w3_, w4_, ki_]
:=
0.5*\(((\(
\(((\((Ai*Exp[\(-\Alpha_i\))*\((go1 + \((x +
xptp)\)\)\)/w1])) + ki)
\)*\(((\((Ai*Exp[\(-\Alpha_i\))*\((go1 + \((x +
xptp)\)\)\)\)/w2])) +
\((\((\((\((Ai*Exp[\(-\Alpha_i\))*\((go2 + \((x +
xptp)\)\)\)\)/w3])) + ki)\)*\(
\((Ai*Exp[\(-\Alpha_i\))*\((go2 + \((x +
xptp)\)\)\)\)/w4])) +
ki)\))))\)\) +
ff2[1.00,160,0.0375,0.0875,-0.000035456,-
0.00261,0.375,1.25,0.75,1.25,1.104]
1.2252
D[ff2[Ai,160,0.0375,0.0875,-0.000035456,-
0.00261,0.375,1.25,0.75,1.25,1.104],
Ai]
0.5 (0.000019185 (1.104\[InvisibleSpace]+1.3749\times10\^-8 Ai)+0.0115464
(1.104\[InvisibleSpace]+3.47927\times10\^-7 Ai)+1.3749\times10\^-8 (
1.104\[InvisibleSpace]+0.000019185 Ai)+3.47927\times10\^-7 (
1.104\[InvisibleSpace]+0.0115464 Ai))
pdAi=%/.Ai->1.00
0.00638441
D[ff2[1.00,\Alpha_i,0.0375,0.0875,-0.000035456,-
0.00261,0.375,1.25,0.75,1.25,
1.104],\Alpha_i]
0.5 (-0.0678836
E\^-0.0678836 \Alpha_i (
1.104\[InvisibleSpace]+1. E\^-0.113139 \Alpha_i)-0.0278836
E\^-0.0278836 \Alpha_i (
1.104\[InvisibleSpace]+1. E\^-0.0929455 \Alpha_i)-0.113139
E\^-0.113139 \Alpha_i (
1.104\[InvisibleSpace]+1. E\^-0.0678836 \Alpha_i)-0.0929455
E\^-0.0929455 \Alpha_i (
1.104\[InvisibleSpace]+1. E\^-0.0278836 \Alpha_i))
pd\[Alpha]i=%/.\[Alpha]i->160
-0.000178457
D[ff2[1.00,160,go1,0.0875,-0.000035456,-
0.00261,0.375,1.25,0.75,1.25,1.104],
go1]
0.5 (-128.
E\^-128. (-0.00264546+go1) (
1.104\[InvisibleSpace]+1. E\^-426.667 (-0.00264546+go1))-
426.667
E\^-426.667 (-0.00264546+go1) (

```

```

1.104\[InvisibleSpace]+1. E\^-128. (-0.00264546+go1)))
pdgo1=%/.go1->0.0375
-0.815905
D[ff2[1.00,160,0.0375,go2,-0.000035456,-
0.00261,0.375,1.25,0.75,1.25,1.104],-
go2]
0.5 (-128.
E\^-128. (-0.00264546+go2) (
1.104\[InvisibleSpace]+1. E\^-213.333 (-0.00264546+go2))-213.333
E\^-213.333 (-0.00264546+go2) (
1.104\[InvisibleSpace]+1. E\^-128. (-0.00264546+go2)))
pdgo2=%/.go2->0.0875
-0.00135715
D[ff2[1.00,160,0.0375,0.0875,x,-0.00261,0.375,1.25,0.75,1.25,1.104],x]
0.5 (-128.
E\^-128. (0.03489\[InvisibleSpace]+x) (
1.104\[InvisibleSpace]+1.
E\^-426.667 (0.03489\[InvisibleSpace]+x))-426.667
E\^-426.667 (0.03489\[InvisibleSpace]+x) (
1.104\[InvisibleSpace]+1.
E\^-128. (0.03489\[InvisibleSpace]+x))-128.
E\^-128. (0.08489\[InvisibleSpace]+x) (
1.104\[InvisibleSpace]+1.
E\^-213.333 (0.08489\[InvisibleSpace]+x))-213.333
E\^-213.333 (0.08489\[InvisibleSpace]+x) (
1.104\[InvisibleSpace]+1. E\^-128.
(0.08489\[InvisibleSpace]+x)))
pdx=%/.x->-0.000035456
-0.817263
D[ff2[1.00,160,0.0375,0.0875,-
0.000035456,xptp,0.375,1.25,0.75,1.25,1.104],-
xptp]
0.5 (-128.
E\^-128. (0.0374645\[InvisibleSpace]+xptp) (
1.104\[InvisibleSpace]+1.
E\^-426.667 (0.0374645\[InvisibleSpace]+xptp))-426.667
E\^-426.667 (0.0374645\[InvisibleSpace]+xptp) (
1.104\[InvisibleSpace]+1.
E\^-128. (0.0374645\[InvisibleSpace]+xptp))-128.
E\^-128. (0.0874645\[InvisibleSpace]+xptp) (
1.104\[InvisibleSpace]+1.
E\^-213.333 (0.0874645\[InvisibleSpace]+xptp))-213.333
E\^-213.333 (0.0874645\[InvisibleSpace]+xptp) (
1.104\[InvisibleSpace]+1.
E\^-128. (0.0874645\[InvisibleSpace]+xptp)))
pdxptp=%/.xptp->-0.00261
-0.817263
D[ff2[1.00,160,0.0375,0.0875,-0.000035456,-
0.00261,w1,1.25,0.75,1.25,1.104],-
w1]
!\(\(\(3.11054888491809533` \ E\`\`(\`(-
5.57672703999999974`\`)/w1`\`)\`/w1\`^2\`)
pdw1=%/.w1->0.375
7.69596\times10\`^-6
D[ff2[1.00,160,0.0375,0.0875,-0.000035456,-
0.00261,0.375,w2,0.75,1.25,1.104],

```

```

w2]
\!\((3.07835429622796574` \ E\^(\(-
5.5767270399999974`\)/w2\))\)/w2\^2\)
pdw2=%/.w2->1.25
0.0227481
D[ff2[1.00,160,0.0375,0.0875,-0.000035456,-
0.00261,0.375,1.25,w3,1.25,1.104],
 w3]
\!\((7.49448356086047251` \ E\^(\(-
13.5767270399999984`\)/w3\))\)/w3\^2\)
pdw3=%/.w3->0.75
1.83185\times10\^-7
D[ff2[1.00,160,0.0375,0.0875,-0.000035456,-
0.00261,0.375,1.25,0.75,w4,1.104],
 w4]
\!\((7.4943534194129322` \ E\^(\(-
13.5767270399999984`\)/w4\))\)/w4\^2\)
pdw4=%/.w4->1.25
0.0000920187
D[ff2[1.00,160,0.0375,0.0875,-0.000035456,-
0.00261,0.375,1.25,0.75,1.25,ki],
 ki]
0.5 (0.0115659\[InvisibleSpace]+4 ki)
pdki=%/.ki->1.104
2.21378
uAi=0.0005;
u\[Alpha]i=0.5;
ugo1=0.0005;
ugo2=0.0005;
ux=0.0005;
uxptp=0.0005;
uw1=0.005;
uw2=0.005;
uw3=0.005;
uw4=0.005;
uki=0.0005;
\!(Uff2curr =
Sqrt[\(((uAi*pdAi)\)\)\^2 + \(((u\[Alpha]i*pd\[Alpha]i)\)\)\^2 +
\(((ugo1*pdgo1)\)\)\^2 + \(((ugo2*pdgo2)\)\)\^2 +
\n\t\t\t\((ux*pdx)\)\)\^2 +
\(((uxptp*pdxptp)\)\)\^2 + \(((uw1*pdw1)\)\)\^2 + \(((uw2*pdw2)\)\)\^2 +
\(((uw3*pdw3)\)\)\^2 + \(((uw4*pdw4)\)\)\^2 + \(((uki*pdki)\)\)\^2]\)
0.00132155

```

Code for Uncertainty of Current Based Force Equation:

```

ClearAll[fcurr,Ag,ff1,I1,go,x,xptp,Li,mui,ff2,I2]
\!((fcurr[Ag_, ff1_, I1_, go_, x_, xptp_, Li_, mui_, ff2_, I2_] :=
\(((\((0.2248\*4 \ \Pi\)^10\^\(-7\)\)^Ag\^615\^2\)/2)\)*
\(((\((ff1\*I1\^2\)\)\/\((2\*((go - \((x + xptp)\)))\)) +
\((\((Li\)/mui)\)\)\)\^2
- \((ff2\*
I2\^2\)\)\/\((2\*((go + \((x + xptp)\)))\)) +
\((\((Li\)/mui)\)\)\)\^2
\))\))
fcurr[1.875,1.22206,1.853947,0.0625,-0.000035456,-
0.00261,4.5,3000,1.2252,

```

```

0.358461]
23.1505
D[fcurr[Ag,1.22206,1.853947,0.0625,-0.000035456,-
0.00261,4.5,3000,1.2252,
0.358461],Ag]
12.3469
pdAg=%/.Ag->1.875
12.3469
D[fcurr[1.875,ff1,1.853947,0.0625,-0.000035456,-
0.00261,4.5,3000,1.2252,
0.358461],ff1]
19.8222
pdf1=%/.ff1->1.22206
19.8222
D[fcurr[1.875,1.22206,I1,0.0625,-0.000035456,-0.00261,4.5,3000,1.2252,
0.358461],I1]
14.0955 I1
pdI1=%/.I1->1.853947
26.1322
D[fcurr[1.875,1.22206,1.853947,go,-0.000035456,-
0.00261,4.5,3000,1.2252,
0.358461],go]
\!\((0.100167694702357179`\
\((0.629724809183716782`\
\/\((\(\(0.0015`\[InvisibleSpace]\) +
2\ \((\((-0.0026454560000000025`\) + go)\))\)\)^3 -
16.8014649210933058`\
\/\((\(\(0.0015`\[InvisibleSpace]\) +
2\ \((\((0.0026454560000000025`\[InvisibleSpace]\) +
go)\))\)\^3)\)\)
pdgo=%/.go->0.0625
-699.8
D[fcurr[1.875,1.22206,1.853947,0.0625,x,-
0.00261,4.5,3000,1.2252,0.358461],Ag]

0
pdx=%/.x-->-0.000035456
0
D[fcurr[1.875,1.22206,1.853947,0.0625,-
0.000035456,xptp,4.5,3000,1.2252,
0.358461],xptp]
\!\((0.100167694702357179`\
\((16.8014649210933058`\
\/\((\(\(0.0015`\[InvisibleSpace]\) +
2\ \((\((0.0625354559999999981`\[InvisibleSpace]\) -
xptp)\))\)\^3 + 0.629724809183716782`\
\/\((\(\(0.0015`\[InvisibleSpace]\) +
2\ \((\((0.0624645440000000018`\[InvisibleSpace]\) +
xptp)\))\)\^3)\)\)
pdxptp=%/.xptp->-0.00261
770.644
D[fcurr[1.875,1.22206,1.853947,0.0625,-0.000035456,-
0.00261,Li,3000,1.2252,
0.358461],Li]

```

```

\!\
\!\\(0.100167694702357179`\
\((0.000104954134863952797`\
\\((\\((0.119709087999999997`\[InvisibleSpace]\) +
Li\\3000)\))\)^3 -
0.00280024415351555067`\
\\((\\((0.130290912000000003`\[InvisibleSpace]\) +
Li\\3000)\))\)^3)
\\\
pdLi=%/.Li->4.5
-0.116633
D[fcurr[1.875,1.22206,1.853947,0.0625,-0.000035456,-
0.00261,4.5,mui,1.2252,
0.358461],mui]
\!\\(*
RowBox[{"0.100167694702357179`", " ",
RowBox[{"(", ,
RowBox[{{
RowBox[{"-", ,
FractionBox["1.41688082066336278`",
RowBox[{"(",
SuperscriptBox[
RowBox[{"(",
RowBox[{\\"((0.11970908799999997`\[InvisibleSpace]\),
"+",
FractionBox[
StyleBox["4.5`",
StyleBoxAutoDelete->True,
PrintPrecision->2], "mui"]}], ")"}], "3"], " ",
\^(mui\^2\)]}]], "+",
FractionBox["37.8032960724599353`",
RowBox[{{
SuperscriptBox[
RowBox[{"(", ,
RowBox[{\\"((0.130290912000000003`\[InvisibleSpace]\),
"+",
FractionBox[
StyleBox["4.5`",
StyleBoxAutoDelete->True,
PrintPrecision->2], "mui"]}], ")"}], "3"], " ",
\^(mui\^2\)]}]], ")"}]]\)
pdmui=%/.mui->3000
0.00017495
D[fcurr[1.875,1.22206,1.853947,0.0625,-0.000035456,-
0.00261,4.5,3000,ff2,
0.358461],ff2]
-0.876075
pdf2=%/.ff2->1.2252
-0.876075
D[fcurr[1.875,1.22206,1.853947,0.0625,-0.000035456,-
0.00261,4.5,3000,1.2252,
I2],I2]
-16.7068 I2
pdI2=%/.I2->0.358461
-5.98875
uAg=0.0158607;
uff1=0.00116548;
uI1=0.00005;

```

```

ugo=0.0005;
ux=0.0005;
uxptp=0.0005;
uLi=0.05;
umui=500;
uff2=0.00132155;
uI2=0.00005;
\!\!(Ufcurr =
    Sqrt[\(((uAg*pdAg)\)\)^2 + \((uff1*pdff1)\)\)^2 + \((uI1*pdi1)\)\)^2 +
    \((ugo*pdgo)\)\)^2 + \n\t\t\t\((ux*pdx)\)\)^2 +
\((uxptp*pdxptp)\)\)^2 +
    \((uLi*pdLi)\)\)^2 + \((umui*pdmui)\)\)^2 + \((uff2*pdff2)\)\)^2 +
    \((uI2*pdi2)\)\)^2]
0.56345

```

Code for Uncertainty of Flux Based Top Fringing Equation (ff₁):

```

ClearAll[ff1, Ab, \[Alpha]b, go, x, xptp, w, kb]
\!\!(ff1[Ab_, \[Alpha]b_, go_, x_, xptp_, w_, kb_] :=
    \((Ab*Exp[\(-\[Alpha]b\)*\((go - \((x + xptp)\)\)\)/w])\)\) + kb\)
ff1[1.542, 40, 0.0625, -0.000035456, -0.0044325, 1.25, 1.057]
1.23788
D[ff1[Ab, 40, 0.0625, -0.000035456, -0.0044325, 1.25, 1.057], Ab]
0.117305
pdAb=%/.Ab->1.542
0.117305
D[ff1[1.542, \[Alpha]b, 0.0625, -0.000035456, -
0.0044325, 1.25, 1.057], \[Alpha]b]
\!\!(\((-0.0826116705215999935`)\)\)
E^\((-0.053574364799999961`\)\) \[Alpha]b\)\)
pd\[Alpha]b=%/.\[Alpha]b->40
-0.00969079
D[ff1[1.542, 40, go, -0.000035456, -0.0044325, 1.25, 1.057], go]
\!\!(\((-49.3440000000000011`\)\)
E^\((-32.0000000000000017`\)\)
\((\((0.0044679559999999915`\)[InvisibleSpace]\) + go)\)\)\)
pdgo=%/.go->0.0625
-5.78832
D[ff1[1.542, 40, 0.0625, x, -0.0044325, 1.25, 1.057], x]
\!\!(49.3440000000000011`\)
E^\((-32.0000000000000017`\)\)
\((\((0.066932500000000081`\)[InvisibleSpace]\) - x)\)\)\)
pdx=%/.x->-0.000035456
5.78832
D[ff1[1.542, 40, 0.0625, -0.000035456, xptp, 1.25, 1.057], xptp]
\!\!(49.3440000000000011`\)
E^\((-32.0000000000000017`\)\)
\((\((0.062535455999999981`\)[InvisibleSpace]\) - xptp)\)\)\)
pdxptp=%/.xptp->-0.0044325
5.78832
D[ff1[1.542, 40, 0.0625, -0.000035456, -0.0044325, w, 1.057], w]
\!\!(\((4.13058352607999967`\ E^\((-2.678718239999998`\)/w)\)\)\)/w^2\)
pdw=%/.w->1.25
0.310105
D[ff1[1.542, 40, 0.0625, -0.000035456, -0.0044325, 1.25, kb], kb]
1
pdkb=%/.kb->1.057

```

```

1
uAb=0.0005;
u\[Alpha]b=0.5;
ugo=0.0005;
ux=0.0005;
uxptp=0.0005;
uw=0.005;
ukb=0.0005;
\!\!(Uff1flux =
    Sqrt[\((uAb*pdAb)\)\^2 + \((u\[Alpha]b*pd\[Alpha]b)\)\^2 +
        \((ugo*pdgo)\)\^2 + \n\t\t\t\((ux*pdx)\)\^2 +
        \((uxptp*pdxptp)\)\^2 +
        \((uw*pdw)\)\^2 + \((ukb*pdkb)\)\^2]\)
0.00715988

```

Code for Uncertainty of Flux Based Bottom Fringing Equation (ff₂):

```

ClearAll[ff2, Ab, \[Alpha]b, go, x, xptp, w, kb]
\!\!(ff2[Ab_, \[Alpha]b_, go_, x_, xptp_, w_, kb_] :=
    \((Ab*Exp[\(-\[Alpha]b\)*\((go + \((x + xptp)\)\)\)/w])\)) + kb\)
ff2[1.542, 40, 0.0625, -0.000035456, -0.0044325, 1.25, 1.057]
1.29776
D[ff2[Ab, 40, 0.0625, -0.000035456, -0.0044325, 1.25, 1.057], Ab]
0.156136
pdAb=%/.Ab->1.542
0.156136
D[ff2[1.542, \[Alpha]b, 0.0625, -0.000035456, -
0.0044325, 1.25, 1.057], \[Alpha]b]
\!\!(\((-0.0715883294784000057`)\) \
E^\((-0.0464256352000000038`\)\) \[Alpha]b\))
pd\[Alpha]b=%/.\[Alpha]b->40
-0.0111775
D[ff2[1.542, 40, go, -0.000035456, -0.0044325, 1.25, 1.057], go]
\!\!(\((-49.3440000000000011`\)\) \
E^\((-32.0000000000000017`\)\) \
\((\((-0.0044679559999999915`\) + go)\)\)\)
pdgo=%/.go->0.0625
-7.70439
D[ff2[1.542, 40, 0.0625, x, -0.0044325, 1.25, 1.057], x]
\!\!(\((-49.3440000000000011`\)\) \
E^\((-32.0000000000000017`\)\) \
\((\((0.058067500000000096`\)[InvisibleSpace]\) + x)\)\)\)
pdx=%/.x->-0.000035456
-7.70439
D[ff2[1.542, 40, 0.0625, -0.000035456, xptp, 1.25, 1.057], xptp]
\!\!(\((-49.3440000000000011`\)\) \
E^\((-32.0000000000000017`\)\) \
\((\((0.062464544000000018`\)[InvisibleSpace]\) + xptp)\)\)\)
pdxptp=%/.xptp->-0.0044325
-7.70439
D[ff2[1.542, 40, 0.0625, -0.000035456, -0.0044325, w, 1.057], w]
\!\!(\((3.57941647391999984`\ E^\((-2.32128175999999974`\)/w)\)\)/w\^2\)
pdw=%/.w->1.25
0.357681
D[ff2[1.542, 40, 0.0625, -0.000035456, -0.0044325, 1.25, kb], kb]
1

```

```

pdkb=%/.kb->1.057
1
uAb=0.0005;
u\[Alpha]b=0.5;
ugo=0.0005;
ux=0.0005;
uxptp=0.0005;
uw=0.005;
ukb=0.0005;
\!\!(Uff2flux =
    Sqrt[\((uAb*pdAb)\)\^2 + \((u\[Alpha]b*pd\[Alpha]b)\)\^2 +
        \((ugo*pdgo)\)\^2 + \n\t\t\t\((ux*pdx)\)\^2 +
        \((uxptp*pdxptp)\)\^2 +
        \((uw*pdw)\)\^2 + \((ukb*pdkb)\)\^2]\)
0.00889984

```

Code for Uncertainty of Flux Based Force Equation:

```

ClearAll[fflux,Ag,ff1,B1,ff2,B2]
\!\!(fflux[Ag_, ff1_, B1_, ff2_, B2_] :=
  \((\((0.2248*0.0254\^2*Ag)\)\/\(2*4 \ \[Pi]*10\^(-7)\)))\)*
  \((ff1*B1\^2 - ff2*B2\^2)\))
fflux[1.875,1.23788,0.40756,1.29776,0.099041]
20.8704
D[fflux[Ag,1.23788,0.40756,1.29776,0.099041],Ag]
11.1309
pdAg=%/.Ag->1.875
11.1309
D[fflux[1.875,ff1,0.40756,1.29776,0.099041],ff1]
17.9725
pdff1=%/.ff1->1.23788
17.9725
D[fflux[1.875,1.23788,B1,1.29776,0.099041],B1]
267.876 B1
pdB1=%/.B1->0.40756
109.176
D[fflux[1.875,1.23788,0.40756,ff2,0.099041],ff2]
-1.06134
pdff2=%/.ff2->1.29776
-1.06134
D[fflux[1.875,1.23788,0.40756,1.29776,B2],B2]
-280.834 B2
pdB2=%/.B2->0.099041
-27.8141
uAg=0.0158607;
uff1=0.00715988;
uB1=0.00005;
uff2=0.00889984;
uB2=0.00005;
\!\!(Ufcurr =
    Sqrt[\((uAg*pdAg)\)\^2 + \((uff1*pdf1)\)\^2 + \((uB1*pdB1)\)\^2 +
        \((uff2*pdf2)\)\^2 + \((uB2*pdB2)\)\^2]\)
0.21874

```

Appendix C

FFT Analysis of Dynamic Data

C.1 FFT Analysis for Data from Original System

Fourier transforms were performed on the time response data from the sine sweep shown in Figure 7.6. Figures C.1 through C.4 show the frequency responses for the load cell, flux based, and current based measurements, respectively. The first plot of each plot of each frequency response is displayed from zero to 500Hz or the sampling frequency. The data is symmetric about 250Hz, the Nyquist frequency, which is typical of an extended Fourier transform presentation. The second plot of each frequency response is a zoomed portion of the first plot from zero to 100Hz. This allows more detail to be seen in the frequency range of interest. The spikes are seen from 5Hz to 50Hz in 3Hz steps because a discrete rather than continuous sine sweep was used as the input.

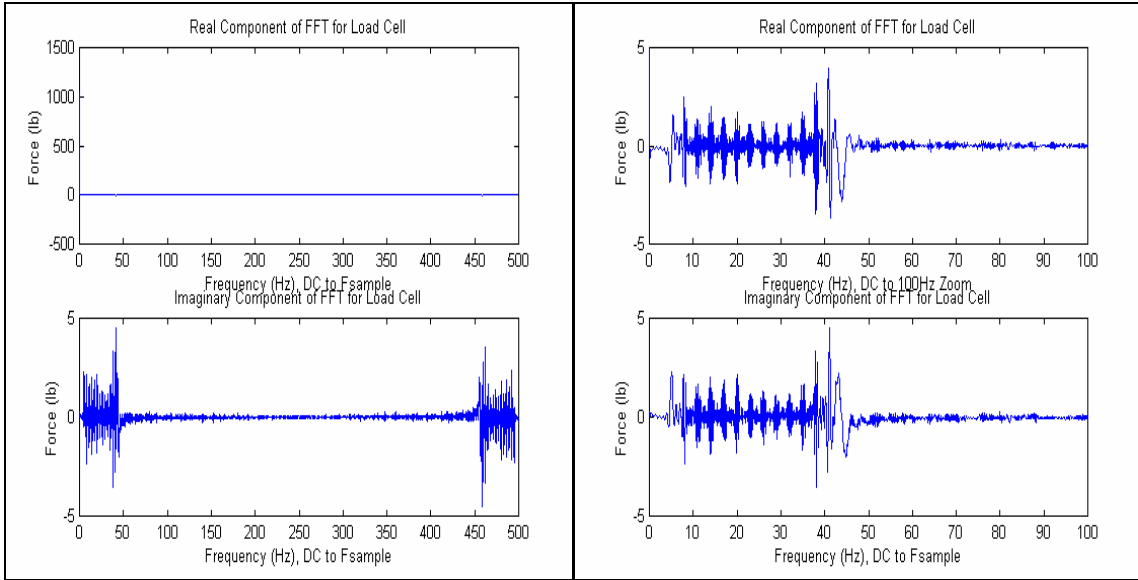


Figure C.1: Frequency Response of Load Cell Measurement with Swept Sine Input for Original System

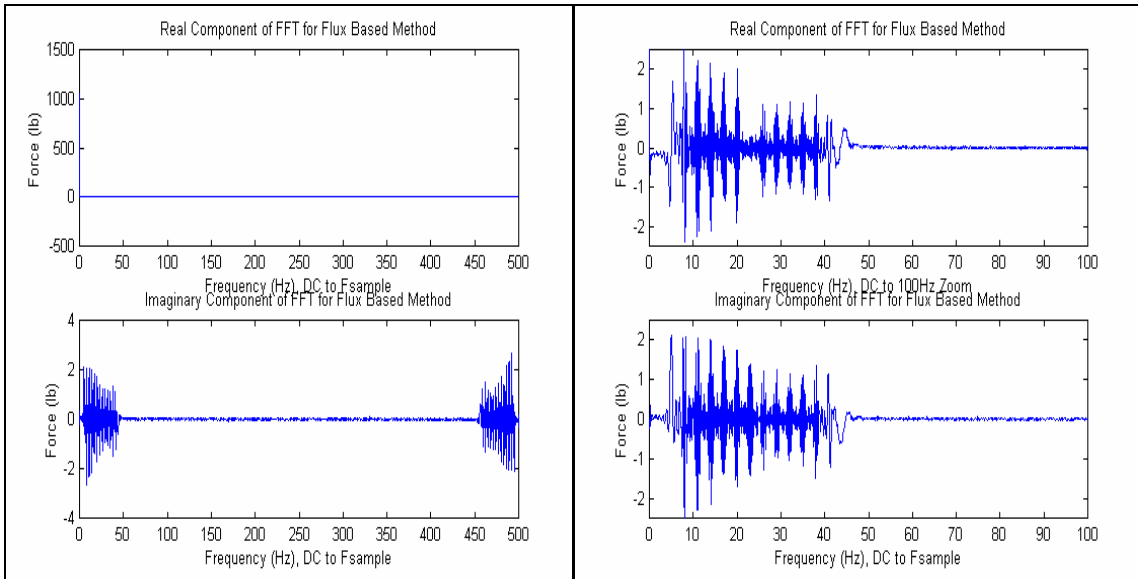


Figure C.2: Frequency Response of Flux Based Resultant Measurement with Swept Sine Input for Original System

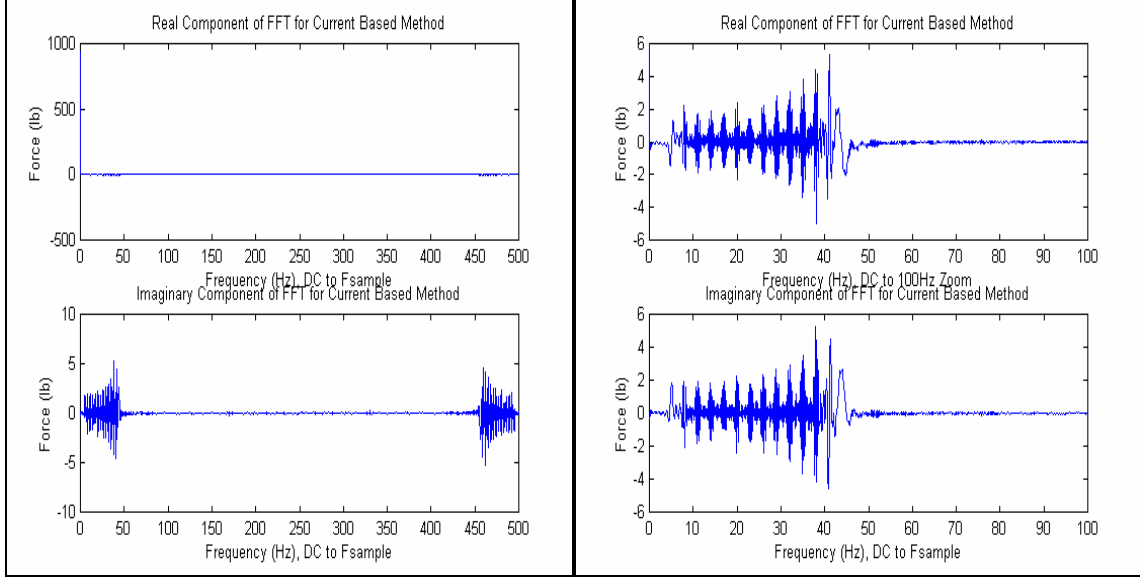


Figure C.3: Frequency Response of Current Based Resultant Measurement with Swept Sine Input for Original System

The frequency response plots show more clearly the trends seen in the time response plot of Figure 7.6. Figure C.1 shows the initial decrease in response from the load cell followed by an increase above about 35Hz. The frequency response plots from Figure C.2 show the decreasing trend in the flux based measurements with increasing frequency; while Figure C.3 shows the increasing trend in the current based measurements with increasing frequency. The next section illustrates the added versatility a magnetically levitated thrust measurement system by changing the system dynamics seen in these tests by simply varying the gain parameters of the thrust bearings.

C.2 FFT Analysis for Data from Stiffer System

The frequency response plots for the stiffer system are shown in Figures C.4 through C.6. The first plot for the frequency response is the Fourier transform of the time data in Figure 7.12 displayed from zero to 500Hz, the sampling frequency. The second plot is a zoom of the first plot from zero to 100Hz to show the frequency range of interest in more detail.

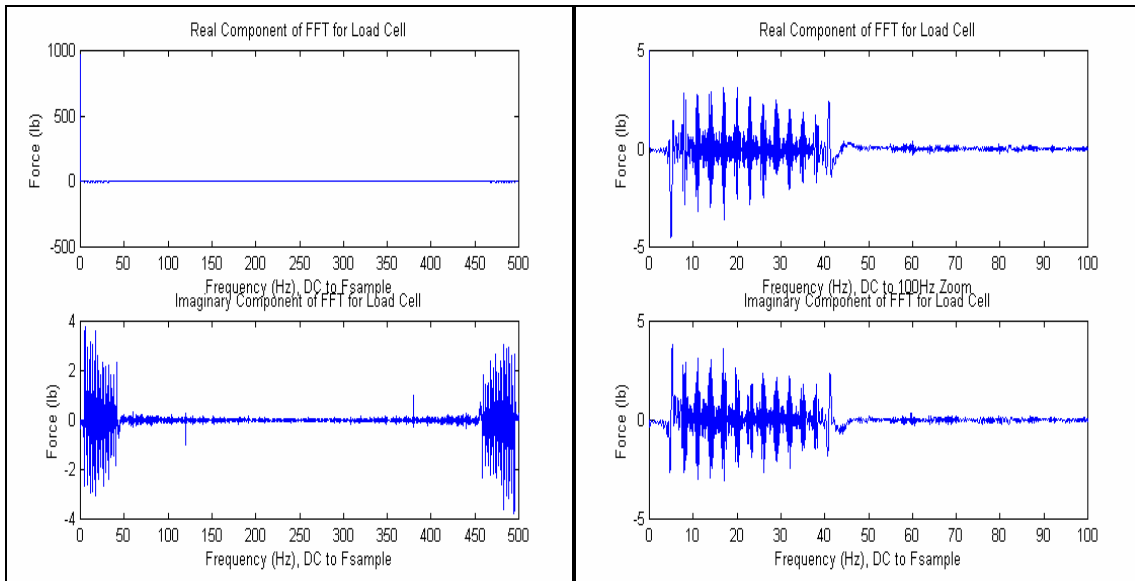


Figure C.4: Frequency Response of Load Cell Measurement with Swept Sine Input for Stiffer System

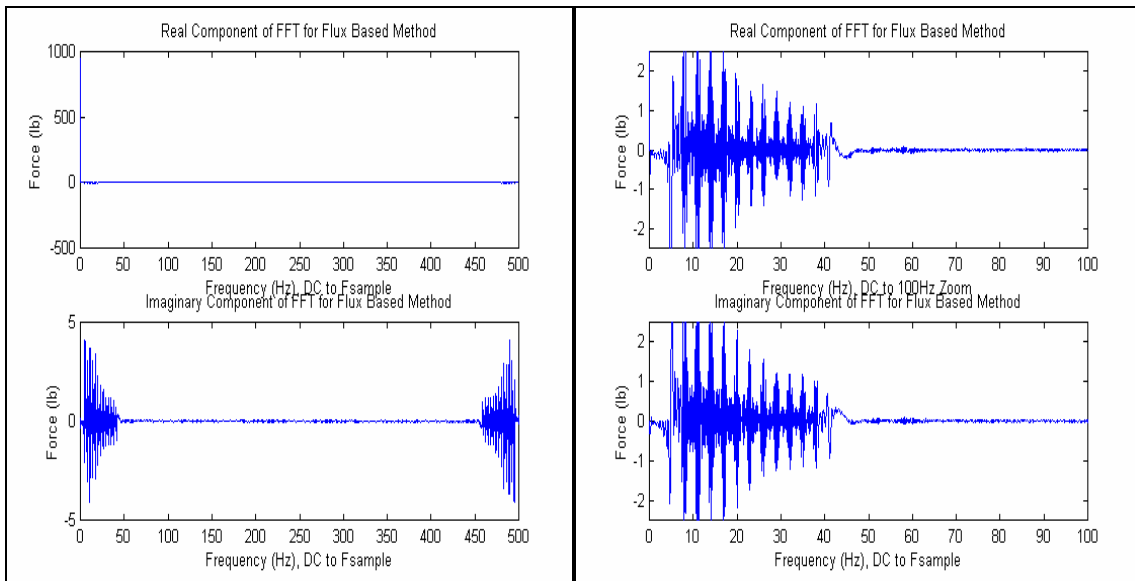


Figure C.5: Frequency Response of Flux Based Resultant Measurement with Swept Sine Input for Stiffer System

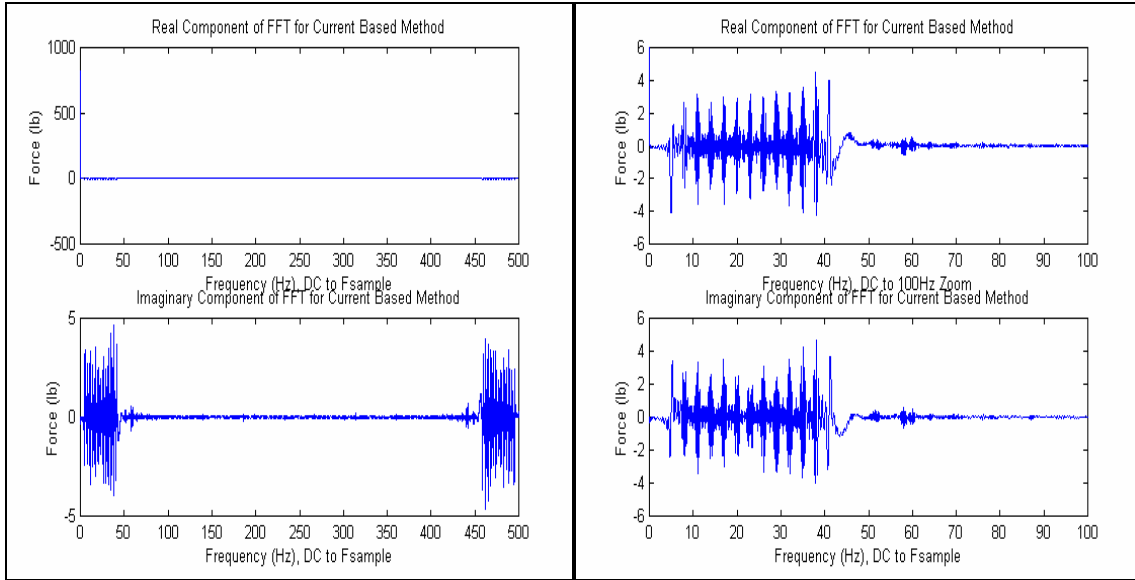


Figure C.6: Frequency Response of Current Based Resultant Measurement with Swept Sine Input for Stiffer System

Comparing these results to the results from the original system, the magnitudes of all the measurements are higher at lower frequencies and lower at higher frequencies. Consequently, the response is more uniform over the entire frequency range. Again, because the decreasing then increasing trend is no longer evident in the load cell data, it appears as though the resonant frequency has been increased from about 35Hz to beyond 50Hz simply by changing the gain parameters of the thrust bearings. These results show that changing the gain parameters of the magnetic bearings can change the dynamics of the TMS demonstrator.

Vita

Eric J. Blumber was born on April 30, 1978 in Newport News, Virginia. He graduated from Menchville High School in May 1996 and enrolled at Virginia Polytechnic Institute and State University. While obtaining his degree at Virginia Tech, he worked several internships including Gannett Flemming Planners and Engineers as well as the Energy Management Institute of Virginia Tech. In May 2000, he graduated Summa Cum Laude in Mechanical Engineering. While in his senior year at Virginia Tech, he was accepted into the 5-Year Bachelors/Masters Program to pursue a Masters Degree in Mechanical Engineering. As a graduate student, Eric worked with advisor Mary Kasarda as well as Joe Imlach of Imlach Consulting Engineering in Alaska on a magnetically levitated rocket thrust measurement system. Due to the timeline of the project, five years became six years to complete his Masters Degree. Eric graduated in June 2002 with his Masters Degree in Mechanical Engineering. He will be taking a job with Calnetix, a custom motor/generator manufacturer, in Torrance (Los Angeles), CA.